PERMEABILITY, CLAY MINERALOGY, AND MICROFABRIC OF SEDIMENTS FROM IODP EXPEDITION 348, SITE C0002, NANKAI TROUGH ACCRETIONARY PRISM, OFFSHORE SOUTHWEST JAPAN

A Thesis

presented to

the Faculty of the Graduate School

at the University of Missouri-Columbia

In Partial Fulfillment

of the Requirements for the Degree

Master of Science

---

by

CHEN SONG

Dr. Michael B. Underwood, Thesis Supervisor

MAY 2015

The undersigned, appointed by the dean of the Graduate School, have examined the thesis entitled

PERMEABILITY, CLAY MINERALOGY, AND MICROFABRIC OF SEDIMENTS FROM IODP EXPEDITION 348, SITE C0002, NANKAI TROUGH ACCRETIONARY PRISM, OFFSHORE SOUTHWEST JAPAN

presented by Chen Song,

a candidate for the degree of master of science,

and hereby certify that, in their opinion, it is worthy of acceptance.

Professor Michael Underwood

Professor Martin Appold

Professor John Bowders

ACKNOWLEDGEMENTS

This research used samples and data provided by the Integrated Ocean Drilling Program (IODP). We thank the MQJ crew, MWJ technicians, and shipboard scientists aboard *D/V Chikyu* for their assistance in acquisition of samples during Expeditions 348. The Consortium for Ocean Leadership Award T348A58 to Dr. Mike Underwood funded this research.

Also, I would like to thank my thesis advisor, Dr. Mike Underwood, for guiding me through this thesis process. His patience and valuable advice were essential to the completion of my graduate study in the field of Geological Sciences at the University of Missouri. I would also like to thank my thesis committee members, Dr. Martin Appold and Dr. John Bowders, who have provided valuable comments and discussion to improve the quality of this thesis. Moreover, I'd like to thank for all the support and help from all the faculty and colleagues from Department of Geological Sciences, the constant-flow apparatus and ESEM equipment provided by Department of Civil and Environmental Engineering and the Electron Microscopy Core Facility at the University of Missouri. I also want to thank New Mexico Bureau of Geology & Mineral Resource in New Mexico Institute of Mining and Technology for providing the XRD technique support. Additionally many thanks also go out to my friends and family for their continuous encouragement and support during my time at the University of Missouri.

TABLE OF CONTENTS

ACKNOWLEDGMENTS ii

LIST OF FIGURES vi

LIST OF TABLES x

ABSTRACT xi

Chapter 1 Introduction 1

1.1 Subduction zone and accretionary prism 1

1.2 Relevance of Nankai Trough 2

1.3 Seismogenic zone experiment 5

1.4 Relations between porosity, microfabric and permeability 7

1.5 Clay mineralogy and diagenesis 9

1.6 Objectives 10

Chapter 2 Geologic Background 11

2.1 Tectonic evolution of Japan 11

2.2 Shikoku Basin and Nankai accretionary prism 14

2.3 Kumano transect 18

2.4 Previous expeditions for NanTroSEIZE 21

2.5 Summary of Sites C0002 and C0009 22

Chapter 3 Methods 27

3.1 Recovery of cuttings and core samples 27

3.2 Sample preparation for constant flow test 28

3.2.1 Sample preparation 28

3.2.2 Constant-flow apparatus 30

3.2.3 Backpressure saturation 31
3.2.4 Constant-flow permeation 32
3.2.5 Constant-flow test data analysis 33
3.3 X-ray diffraction for bulk powder and clay-size fraction 34
3.3.1 Bulk mineralogy 34
3.3.2 X-ray diffractometer used for clay-size fraction 37
3.3.3 Sample preparation for clay mineralogy 38
3.3.4 Calculating relative clay mineral abundances 39
3.3.5 Calculating percentages of kaolinite and chlorite 40
3.3.6 Calculating expandability of illite/smectite mixed-layer clay 42
3.3.7 Calculating illite percentage in I/S mixed-layer and defining illite crystallinity 43
3.4 ESEM grain fabric analyses 44
3.4.1 Imaging of grain fabric 44
3.4.2 Characterization of microfabric anisotropy 47
3.4.3 Energy dispersive X-ray spectroscopy 48
Chapter 4 Results 49
4.1 Results of constant-flow permeability tests 49
4.1.1 Characterization of specimens 49
4.1.2 Results 53
4.2 Results of XRD analysis for cuttings and cores 56
4.2.1 Shipboard bulk powder 56
4.2.2 Shipboard core samples 58

4.2.3 Cutting samples from Hole C0002F 59

4.2.4 Cluster samples from Hole C0002P 63

4.3 Results of microfabric analyis 69

Chapter 5 Discussion 74

5.1 Comparison of permeability values from Nankai Trough and other subduction zones 74

5.1.1 Other sites from Nankai Trough 74

5.1.2 Global data set 78

5.1.3 Discussion 79

5.2 Comparison of clay mineralogy at different Nankai drilling sites 82

5.3 Interpretation of sediment dispersal system 85

5.4 Clay diagenesis 89

5.5 Implications for deeper drilling research 95

Chapter 6 Conclusions 97

6.1 Permeability and microfabric analysis 97

6.2 Clay mineralogy and diagenesis 98

6.3 Future work 99

References 100

Appendix 116

LIST OF FIGURES

Figure **Page**

1. Illustration of Nankai subduction zone and accretionary prism 2

2. Location map of DSDP/ODP sites in the northern Shikoku Bansin and Nankai Trough region 4

3. Regional bathymetry of Nankai Trough region showing most of the drilling sites from previous DSDP/ODP and IODP explorations 5

4. Overview of plate tectonics of the Japanese arc system 12

5. Volcanic activity along the SW Japan forearc during Sea of Japan opening 13

6. Seismic stratigraphy of the Shikoku Basin sediments 15

7. Different transects along-strike of Nankai accretionary prim 17

8. Structure features of Kumano transect 19

9. Schematic of the recent feature of the Kumano Basin 20

10. Seismic profile along the Nankai Trough axis 23

11. Stratigraphy of site C0002 25

12. Plot of depth versus bedding dip distribution at Hole C0002P 26

13. Illustration representing the horizontal and vertical section of core 28

14. X-ray computed tomography images and photos showing different features presented in the WR specimens 29

15. Schematic and picture of permeability testing system at University of Missouri 31

16. Example of typical responses of transient head difference during flow-through test..33

17. Example of X-ray diffractograms of bulk powder standard 36

18. Representative example of X-ray diffractograms of clay-size fraction 40

19. X-ray diffractogram of a typical kaolinite and chlorite standard mixture 41

20. Plot for calculating expandability of I/S mixed-clay layers.....42

21. Illustrations of steps used during image analysis of microfabric 46

22. Example of energy dispersive X-ray spectroscopy.....48

23. SEM images showing different grain sizes in specimen cut from 348-C0002P-3R-1. 50

24. Possible pyrite framboid inside the specimen cut from 348-C0002P-3R-1 51

25. SEM images of different grain sizes in specimen cut from 348-C0002P-4R-2 52

26. SEM images of grain sizes in specimen cut from 348-C0002P-6R-1 52

27. Plot of intrinsic permeability changing with depth.....55

28. Relative abundances of total clay, quartz, feldspar, and calcite for shipboard bulk powder samples from Holes C0002F, C0002N and C0002P 56

29. Relative abundance of total clay, quartz, feldspar, and calcite for shipboard core and cuttings from Holes C0002N and C0002P 58

30. Relative abundances of smectite, illite, kaolinite/chlorite, and quartz in clay-size fraction of cutting samples from Hole C0002F 59

31. Relative abundances of total clay minerals in bulk sediment 60

32. Plots for clay diagenesis indicators of Hole C0002F.....62

33. Relative abundances of smectite, illite, kaolinite/chlorite, and quartz in clay-size fraction of cluster samples from Hole C0002P 64

34. Relative abundances of total clay minerals in bulk sediment 65

35. Plots for clay diagenesis indicators of Hole C0002P.....67

36. ESEM images for all specimens tested for permeability, Hole C0002P 70

37. Orientation of grains measured on ESEM images, Hole C0002P 71

38. Cumulative frequency curves for grain orientations, Hole C0002P 72

39. Index of orientation plotted as a function of depth, Hole C0002P 73

40. Values of vertical intrinsic permeability versus depth for specimens from Nankai Trough 74

41. Relation between intrinsic permeability and post-test porosity for specimens from different subduction zones 79

42. Index map showing the regional geography, geology and bathymetry of the Nankai study area of southwest Japan 86

43. Schematic illustrations of sources and transport routes for sediments entering the Nankai subduction margin during different time 87

44. Estimated temperature profiles from 900 to 7,000 mbsf at Site C0002 94

A1. SEM images of grain sizes in specimens cut from 348-C0002P-3R-1.....116

A2. Calcium compound in specimen cut from 348-C0002P-3R-1.....116

A3. SEM images of grain sizes in specimens cut from 348-C0002P-4R-2.....117

A4. Possible pyrite inside the specimen cut from 348-C0002P-4R-2 117

A5. SEM images of grain sizes in specimens cut from 348-C0002P-6R-1.....118

A6. Barite inside the specimen cut from 348-C0002P-6R-1.....118

A7. Hydraulic gradient versus discharge velocity (348-C0002P-3R-1, 51 cm @0.28 MPa) 119

A8. Hydraulic gradient versus discharge velocity (348-C0002P-3R-1, 51 cm @0.55 MPa) 119

A9. Hydraulic gradient versus discharge velocity (348-C0002P-4R-2, 98 cm @0.28 MPa) 120

A10. Hydraulic gradient versus discharge velocity (348-C0002P-4R-2, 98 cm @0.55 MPa) 120

A11. Hydraulic gradient versus discharge velocity (348-C0002P-6R-1, 64 cm @0.28 MPa) 121

LIST OF TABLES

Table **Page**

1. Characteristic X-ray diffraction peaks for semiquantative area analysis of bulk powder 35

2. XRD normalization factors for bulk powder 35

3. XRD normalization factors for clay-size fraction.....39

4. The positions of useful reflections for estimating percent illite in illite/smectite.....44

5. Summary of specimen properties.....53

6. Sample properties and average test results 54

7. Results of XRD analysis for cuttings from Hole C0002F 61

8. Results of XRD analysis for clay diagenesis indicators of Hole C0002F 63

9. Results of XRD analysis for clusters from Hole C0002P 66

10. Results of XRD analysis for clay diagenesis indicators of Hole C0002P 68

11. Statistics for microfabric calculated from analyses of environmental SEM images, Hole C0002P 69

A1. Results of individual constant-flow tests results, Hole C0002P 122

ABSTRACT

One of the main objectives of the Integrated Ocean Drilling Program (IODP) Expedition 348 was to characterize the variations of lithology and structure in the deep interior of the Nankai Trough accretionary complex beneath the Kumano forearc basin, offshore SW Japan. One objective for this study is to document the hydrogeologic properties of different lithologies within the accretionary prism. Specifically, I focus on thin interbeds of fine-grained turbidites and evaluate their relation between sediment microstructure and permeability. In addition, I document the clay mineral assemblages and diagenetic reaction progress. Those results have implications for evaluating factors that control the updip aseismic-seismic transition in fault-slip behavior along the megathrust fault system.

I conducted constant-flow permeability tests on four whole-round (WR) specimens collected from 2174.98 to 2209.64 mbsf. The samples were trimmed parallel to the WR core axis and tested at isotropic effective stresses of 0.28 MPa (40 psi) and 0.55 MPa (80 psi). The specimens are mainly clayey siltstone, with thin interbeds of silty turbidites. Intrinsic permeability (k) values range from 3.80×10^{-18} to 2.66×10^{-17} m^2. Environmental scanning electron microscopy shows that the arrangement of grain fabric is random and does not vary significantly among the specimens tested.

A comparison of permeability data from Hole C0002P with data from other sites of Nankai Trough, as well as data from other subduction zones, indicates that samples from Nankai Trough conform to global trends. Permeability decreases with decreasing porosity and increasing depth. Data from Hole C0002P, however, are similar to data from mud and mudstone in shallow intervals of Sites C0002 and C0004, which indicates

permeability is higher than expected within the deep interior of accretionary prism. The higher permeability values at deeper depth could have been influenced by high density of microfractures, coarser grain size, and lab testing under relatively low confining pressures. Moreover, the very steep bedding dips within the cored interval of turbidites would also favor vertical fluid migration through the accretionary prism, good drainage of pore fluids, and retention of near-hydrostatic pore pressures. If similar conditions and rock properties extend all the way down to the megasplay fault, it could result in increases of effective normal stress and shear strength.

Additionally, 41 cuttings samples (1190.5 - 1990.5 mbsf) from Hole C0002F, and 23 samples adjacent to WR samples (2163 - 2216.8 mbsf) from Hole C0002P were analyzed by the X-ray diffraction (XRD). Results for the clay-size fraction show that smectite is the most abundant clay mineral within the accretionary prism. In Hole C0002F, the expandability of illite/smectite (I/S) mixed-layer clays has an average value of 70%, and the average illite percentage in I/S is 26%. In Hole C0002P, the average expandability of I/S is 69%, and the percentage of illite in I/S varies from 13% to 54%, with an average of 41%.

The XRD results are consistent with data from coeval (late Miocene) mudstones in the Nankai accretionary prism and the Shikoku Basin. Values of illite crystallinity (~0.4-0.7) show that detrital source rocks during the late Miocene had been subjected to advanced levels of diagenesis and incipient greenschist-facies metamorphism, consistent with rock units currently exposed in the Outer Zone of SW Japan. The smectite-to-illite reaction has initiated at the depths sampled in Hole C0002F, and reaction progress has advanced further at the depths cored in Hole C0002P. Linear projection of the diagenetic

gradient to greater depths indicates that the smectite-to-illite reaction probably goes to completion near the megasplay fault (~5200 mbsf). Exhaustion of clay dehydration would be expected to reduce the potential for build-up of fluid overpressures, thereby increasing values of effective normal stress within the seismogenic zone.

Chapter 1 Introduction

1.1 Subduction zone and accretionary prism

Subduction takes place at convergent plate boundaries where one tectonic plate (oceanic lithosphere) slides beneath another tectonic plate (either oceanic or continental lithosphere). Due to the strain caused by the plate convergence, different types of earthquakes occur in the subduction zones, such as megathrust (plate boundary thrust fault) earthquake (Park *et al.* 2002). In addition, during the subducting process, sediments scraped off from the downgoing oceanic crust can be brought to the convergent margins where the material is accreted to the overriding plate to cause crustal thickening and mountain-building, which is usually defined as accretionary prism. Figure 1 shows the Nankai subduction zone and accretionary prism as an example.

During the last 40 years, the geometries and structures of modern accretionary prisms have been well studied through ocean drilling (ODP, IODP) (Ogawa *et al.*, 2011) and marine geophysics (Karig *et al.*, 1975; Kagami *et al.*, 1986). In order to interpret the evolution of ancient accretionary complexes (Ogawa *et al.*, 2011), it is quite important to understand the spatial distribution and temporal progression of accretionary prism deformation, structural and hydrologic evolution of the décollement (a basal detachment fault) zone, fluid flow paths, etc. Moreover, accretionary prisms provide an important natural laboratory for studying initial orogenic processes and the composition and character of oceanic crust. Also, the internal deformation of accretionary prisms is critically related to the earthquake and tsunami damage in coastal areas (Ogawa *et al.*, 2011).

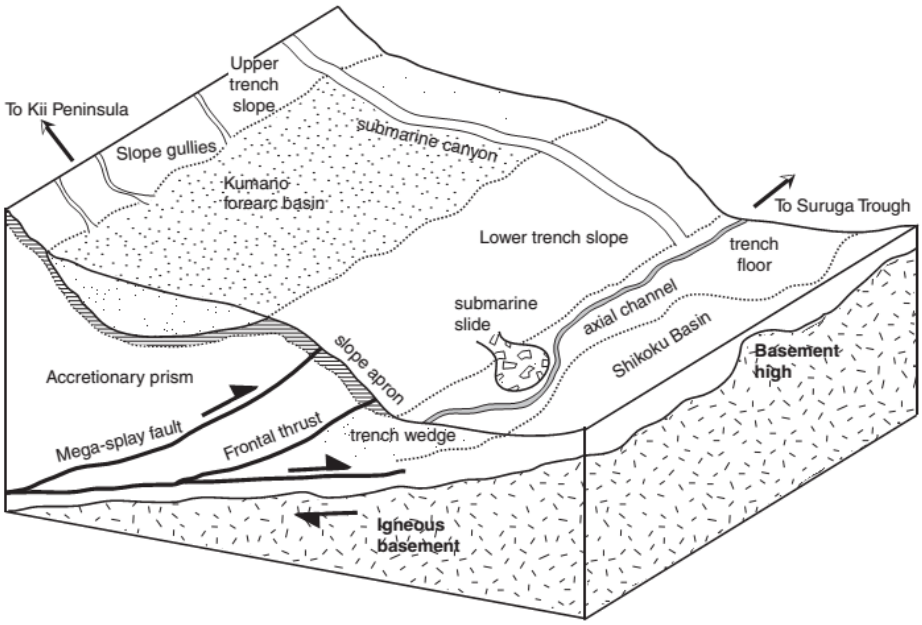

Figure 1. Illustration of Nankai subduction zone and accretionary prism (Underwood and Moore, 2012).

1.2 Relevance of Nankai Trough

Natural disasters such as earthquakes and tsunamis often happen in the subduction zones (e.g., Sumatra, 2004; Japan, 2011). Casualties can be especially high in the heavily populated coastal areas, so it is important to have a better understanding of the phenomena to minimize the consequences. Nankai Trough, located offshore southwest of Japan is one of the most active subduction zones in the world. Historically, great earthquakes record can be traced back for over one thousand years (Cummins *et al.*, 2001), and earthquakes with magnitude larger than 8.0 occur at frequencies from 100 to 200 years (Ando, 1975). The zone of coseismic rupture in future large earthquakes may be more predictable because the entire downdip width of the seismogenic zone ruptures in each event (Tobin and Kinoshita, 2006).

Many drilling projects have been conducted in this region (Figures 2 and 3). Deep Sea Drilling Project (DSDP) Leg 31 Sites 297 and 298 (Ingle *et al.*, 1975), Leg 58 Sites 442, 443 and 444 (deVries Klein *et al.*, 1980) and Leg 87 Sites 582 and 583 (Coulbourn, 1986) helped build understanding of subduction processes and regional sedimentation. The new program Ocean Drilling Program (ODP) continued with Leg 131 Site 808 to study the influence of pore fluids and the hydrogeology of the plate interface (Taira *et al.*, 1991). Legs 190 (Sites 1173-1178) and 196 (Sites 808 and 1173) focused on the relations among deformation, structure and hydrogeology with the addition of borehole observatories (Moore *et al.*, 2001; Mikada *et al.*, 2002). Integrated Ocean Drilling Program (IODP) started a series of expeditions on Nankai Trough Seismogenic Zone Experiment (NanTroSEIZE), which includes Expeditions 314, 315, 316 (Screaton *et al.*, 2009), 319 (Expedition 319 Scientists, 2010), 322 (Underwood *et al.*, 2010), 326, 332, 333 (Expedition 333 Scientists, 2011), 338 (Expedition 338 Scientists, 2014), and 348 (Expedition 348 Scientists, 2015). NanTroSEIZE is the first project to attempt drilling into the seismogenic portion of a megathrust within a subduction zone (Tobin and Kinoshita, 2006).

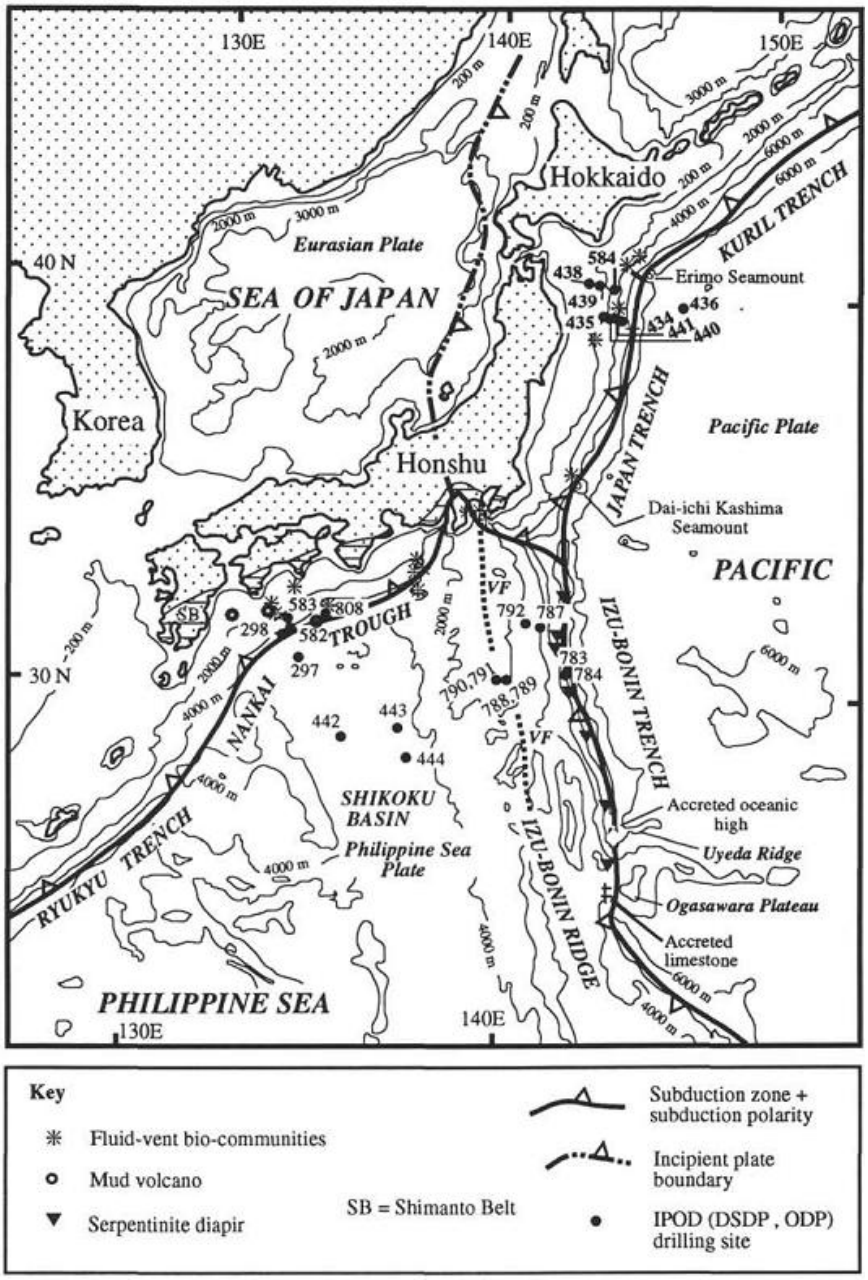

Figure 2. Location map of DSDP/ODP sites in the northern Shikoku Basin and Nankai Trough region (Pickering *et al.*, 1993).

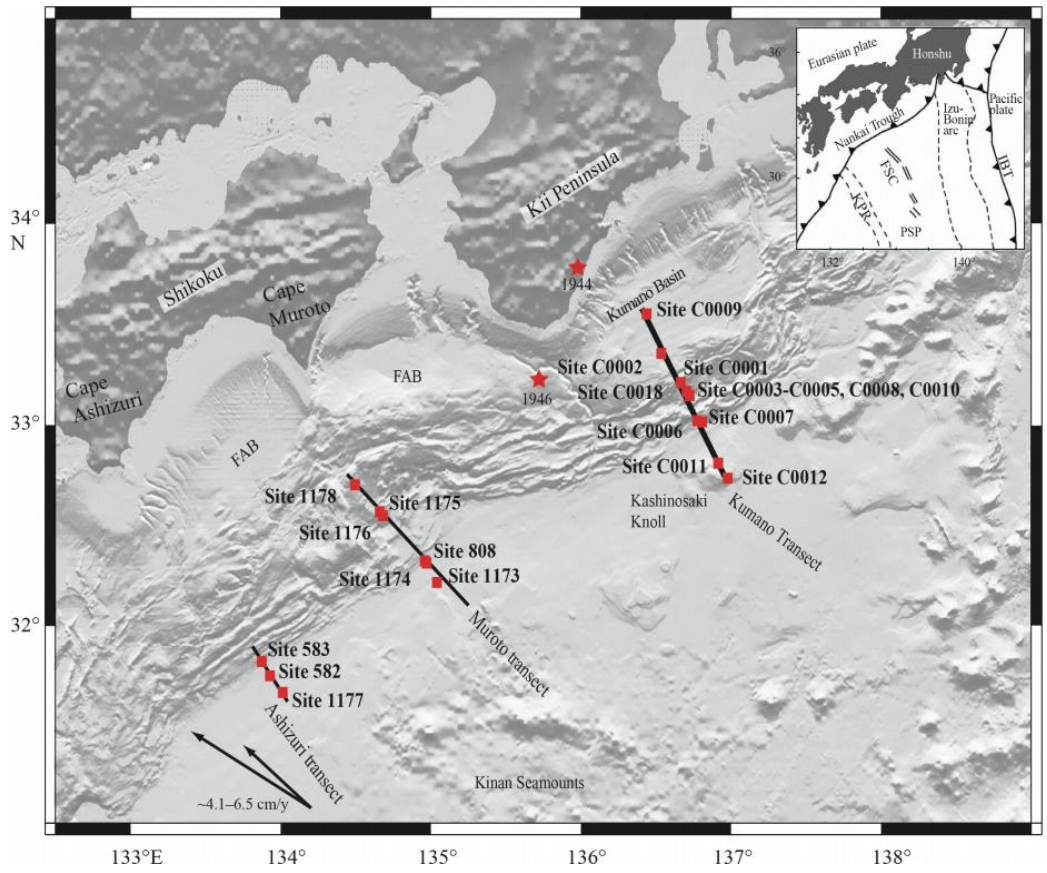

Figure3. Regional bathymetry of Nankai Trough region showing most of the drilling sites from previous DSDP/ODP and IODP explorations. FAB = forearc basin. Inset = tectonic map showing plate tectonic setting of the region. IBT = Izu-Bonin Trench, KPR = Kyushu-Palau Ridge, FSC = fossil spreading center, PSP = Philippine Sea plate. Stars = epicenter locations of last two large subduction earthquakes (1944 and 1946) (Karig *et al.*, 1975; Taira *et al.*, 1991; Moore *et al.*, 2001; Screaton *et al.*, 2009; Underwood *et al.*, 2010; Expedition 333 Scientists, 2011).

1.3 Seismogenic zone experiment

The seismogenic zone of a subduction zone is where earthquakes and co-seismic slip happen. During the International Lithosphere Program (ILP) workshop in 1995 (Uyeda *et al.*, 1995), the Seismogenic Zone Experiment (SEIZE) was conceptualized to study great thrust earthquakes at convergent margins. In 1997, a subsequent workshop focused on the SEIZE research objectives and site selections. One of the important

questions to be answered is what controls the updip and downdip limits of the seismogenic zone on subduction thrusts (Moore and Moore, 1998). The 1997 workshop considered such criteria as high quality earthquake data, imaging of the seismogenic zone by multichannel seismic reflection, favorable drilling conditions, extent of existing drilling data, behavior of the subduction zone (e.g., sediment accretion versus erosion, convergence rate, thermal regime), and prospects for installation of borehole observatories.

Nankai Trough was one of the preferred field locations (the others are Japan Trench and Central America) because subducting sediments can be traced into the seismogenic zone on seismic reflection images and the up-dip limit of the seismogenic zone is within the technological capabilities of the drill ship *Chikyu*. Also, the megathrust is comparatively well inverted for slip (tsunamigenic, seismic, geodetic) with good past large earthquakes history and geodetic coverage of the contemporary deformation of the upper plate (Moore and Moore, 1998). The updip and downdip limits of this seismogenic zone are closely related to the temperature of the plate interface based on a previous 2D thermal model (Yoshioka and Murakami, 2007). In 2007, Nankai Trough Seismogenic Zone Experiment (NanTroSEIZE) began with the first of multiple expeditions conducted over several years.

There are several reasons to conduct seismogenic zone drilling projects in the region offshore the Kii Peninsula on Honshu Island. First, past coseismic rupture extended shallow enough for drilling in only this region based on the slip inversion studies (Ichinose *et al.*, 2003; Baba and Cummins, 2005), and an updip zone of large slip has also been identified and targeted. The megasplay fault should be a primary drilling

target since it suggests that coseismic slip (during events like the 1944 Tonankai earthquake) may also have occurred on the megasplay fault besides the plate boundary décollement (Ichinose *et al.*, 2003; Baba *et al.*, 2006). Second, there is significant interseismic strain accumulation in this region through onshore high-resolution geodetic studies with short duration (Miyazaki and Heki, 2001; Obana *et al.*, 2001). Third, this region has the unique characteristic of the Nankai margin in terms of heat flow and sediment on the incoming plate. Finally, since the operational limits of riser drilling by the *Chikyu* are maximum of 2500 m water depth and 7000 m subseafloor penetration, this target region is within these limits and for example, the seismogenic zone is about 6000 m beneath the seafloor in the seaward portions of the Kumano Basin (Nakanishi *et al.*, 2002).

1.4 Relations between porosity, microfabric and permeability

Physical properties of the submarine samples in subduction zones have been studied widely for a long time (e.g., Coulbourn, 1986; Neuzil, 1994; Dewhurst et al., 1999; Yang and Aplin, 2007; Rowe *et al.*, 2011; Saffer *et al.*, 2011; Yue *et al*, 2012; Screaton *et al.*, 2013; Daigle and Dugan, 2014).Permeability is one of the important properties on studying the mechanics of subduction zones because of its influence on fluid flow and pore pressures (Gamage *et al.*, 2010; Saffer and Bekins, 2002). Pore fluid plays a critical role in fault systems and subduction zones because pore fluid pressure has a significant effect on shear strength (Hubbert and Rubey, 1959). At subduction zones, because of the tectonic loading and mineral dehydration, fluid pressure can rise above hydrostatic values to reduce effective stress (Saffer and Tobin, 2011; Underwood, 2007).

One of the major factors that affect permeability is porosity, which is the fraction of the total volume of material that consists of pore space (Schwartz and Zhang, 2003). The relation between permeability and porosity for sediments in subduction zones has been thoroughly examined (Gamage *et al.*, 2011). Many factors affect the relation between porosity and permeability, such as grain size, diagenetic processes, plastic deformation of the solid skeleton, and mineral dissolution (Dewhurst et al., 1999; Bryant *et al.*, 1981; Noiriel *et al.*, 2004). Moreover, porosity and permeability generally decrease with increasing effective normal stress and mechanical compaction due to changing particle orientation and pore size distribution (Aplin *et al.*, 2006).

The microstructure is another basic property that has significant influence on sediment's physical and mechanical properties and behavior under static and dynamic stresses (Bennett *et al.*, 1991). Bennett *et al.* (1991) pointed out that there are two aspects to the term clay microstructure. Fabric refers to the orientation and arrangement or spatial distribution of the solid particles and the particle-to-particle geometry. The mechanical alteration of the sediment fabric is not only by aggregation taking place in the water column but also by bioturbation after deposition. Physicochemistry is related to the sediment's interparticle forces, which result from both the physical interactions caused by gravitational forces and the electrical nature of the particle and the surrounding fluids. Both the fabric and physicochemistry are important to the understanding of the nature, properties, and large-scale developmental history of sedimentary deposits, but in this thesis, clay fabric is the main focus.

Previous studies have shown that the grain orientation affects the movement of the fluids via permeability anisotropy (Anandarajah and Kuganenthira, 1995; Clennel *et*

al., 1999; Saffer and Tobin, 2011). Compaction can rearrange the distribution of platy grains to a preferred alignment. Fluids usually follow along the direction of strongly preferred grain alignment, so permeability can be more anisotropic under this condition (Sintubin, 1994; Clennel *et al*., 1999; Dewhurst *et al*., 1999; Kim *et al*., 1999).

1.5 Clay mineralogy and diagenesis

Smectite, which is a hydrated mineral, is often a main component of sediments that enter a subduction zone (Vrolijk, 1990). Where smectite is abundant, the existence of significant intragranular water can lead to overestimates of intergranular porosity (Gamage *et al*., 2011). In the interlayer site of smectite, is the hydration state varies as a function of temperature, pressure, interlayer cation species, and salinity (Colten-Bradley, 1987). The volumetric significance of interlayer water increases with burial (Brown and Ransom, 1996). Smectite starts to transform to illite with increasing temperature and effective stress, where illite is precipitated as a more stable diagenetic mineral (Worden and Burley, 2003).Mixed-layer illite/smectite (I/S) can be used as a geothermometer and indicator of thermal maturity based on the concepts of shale diagenesis that were first described from studies of the Gulf Coast (e.g., Powers, 1957, 1967; Burst, 1959, 1969; Perry and Hower, 1970). During the smectite illitization process, fresh water can get into the pore system to increase pore pressure unless drainage can keep pace with fluid production (Lanson *et al*., 2009). Thus, clay diagenesis may play an important role in controlling the position of the up-dip limit of the seismogenic zone (e.g., Moore and Saffer, 2001).

1.6 Objectives

IODP Expedition 348 began on September 13th, 2013 and ended on January 29th, 2014. One of the main objectives of this expedition was to characterize the variations of lithology and structure within the interior of the Nankai Trough accretionary complex beneath the Kumano forearc basin (IODP Expedition 348, 2013). As for this thesis project, the objectives are: (1) to document hydrogeologic properties of different lithologies within the accretionary prism, with a focus on thin interbeds of fine-grained turbidites; (2) to evaluate the relation between sediment microstructure and permeability; (3) to document diagenetic reaction progress as a factor controlling the updip aseismic-seismic transition of the megathrust fault system.

Chapter 2 Geologic Background

2.1 Tectonic evolution of Japan

Kimura *et al.* (2014) summarized the paleogeography of southwest Japan. The Outer Zone of southwest Japan formed during the Cretaceous to the Miocene, through a subduction-accretion process. The subduction initiation of the Izu-Bonin-Mariana arc began ~50 Ma, which was constrained by the age of the forearc igneous basement (Bloomer *et al.*, 1995). Accretion continued to the middle Oligocene (~30 Ma), where it began to spread and propagate both north and south (Kimura *et al.*, 2005). During the Oligocene-Miocene, marginal basins of the Philippine Sea Plate were simultaneously opened, which resulted in the separation of the Japanese islands from the Asian continental margin (Karig, 1971; Tamaki, 1985). Since then, SW Japan has continued growing as a result of the subduction of the Pacific Plate and Philippine Sea Plate from the east and south, respectively. The Shikoku Basin started to form during the late Oligocene by rifting and back-arc spreading behind the Izu-Bonin arc system (Okino *et al.*, 1994; Kobayashi *et al.*, 1995; Sdrolias *et al.*, 2004). Late-stage reorientation of the spreading center and off-axis seamount volcanism continued into the middle and late Miocene (Underwood and Moore, 2012).

Mahony *et al.* (2011) proposed that prior to 15 Ma, Pacific Plate subduction dominated Kyushu tectonics. From 15 to 6 Ma, the evolving relative plate motions shifted the triple junction between the Pacific Plate, Philippine Sea Plate, and southwest Japan toward the northeast (Mahony *et al.*, 2011). This led to the subduction of the Philippine Sea Plate beneath Kyushu. By 6-5 Ma, changes in the Philippine Sea Plate

motion led to more rapid, nearly trench-normal, subduction of Philippine Sea crust beneath Kyushu. They also suggested that collision of the Izu Arc with central Japan (Honshu) initiated at ~8-6 Ma rather than the more widely accepted date of ~15 Ma (Figure 4).

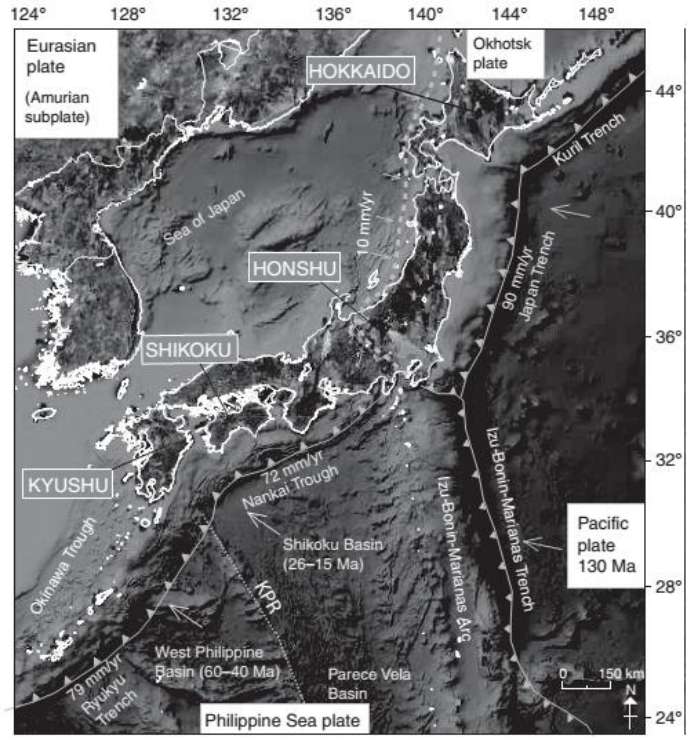

Figure 4. Overview of plate tectonics of the Japanese arc system, indicating the interaction between the three main plates—the Eurasian plate (Amurian subplate), the Philippine Sea plate, and the Pacific plate. White outlined areas indicate land. Convergence rates at each respective plate boundary are labeled in mm/yr. The gray lines with solid triangles mark subduction zones. The gray dashed line cutting across Honshu and up the western side of Honshu and Hokkaido marks a zone of convergent tectonics, which is not a subduction zone. The main subduction zones are marked—the Ryukyu Trench, Nankai Trough, Izu-Bonin-Mariana Trench, Japan Trench, and Kuril Trench. The Okinawa Trough is a recent backarc basin (since 6 Ma). The Sea of Japan, West Philippine Basin, Shikoku Basin, and Parece Vela Basin are mature basins. The Kyushu-Palau ridge (KPR) is a remnant arc currently being subducted beneath Kyushu (Mahony *et al.*, 2011).

Kimura *et al.* (2005) documented the late Cenozoic magmatism in the SW Japan arc. The magmatism included four stages: I- Initial rifting of the Sea of Japan back-arc

Basin (25-17 Ma), II- opening of the Sea of Japan back-arc Basin (17-12 Ma), III- late Teritiary volcanic arc (12-4 Ma), and IV- late Pliocene-Holocene volcanic arc (4 Ma-present). Low alkali tholeiite (LAT) volcanism characterized stage I, and during stage II, the subduction of a young, hot Shikoku Basin caused widespread high-magnesium andesite (HMA) magmatism. In stage III, igneous activity in the forearc of SW Japan ceased after 12 Ma, and rear-arc alkalic volcanism dominated until Quaternary time. During stage IV, subduction of the Shikoku Basin spreading ridge produced MORB-like (mid-oceanic-ridge basalt) tholeiitic basalt and off-ridge alkali basalt magmas at the Pacific coast. Figure 5 presents volcanic activity along the SW Japan forearc during the opening of the Sea of Japan, which could be possible sources of smectite or volcanic ash during the late Miocene.

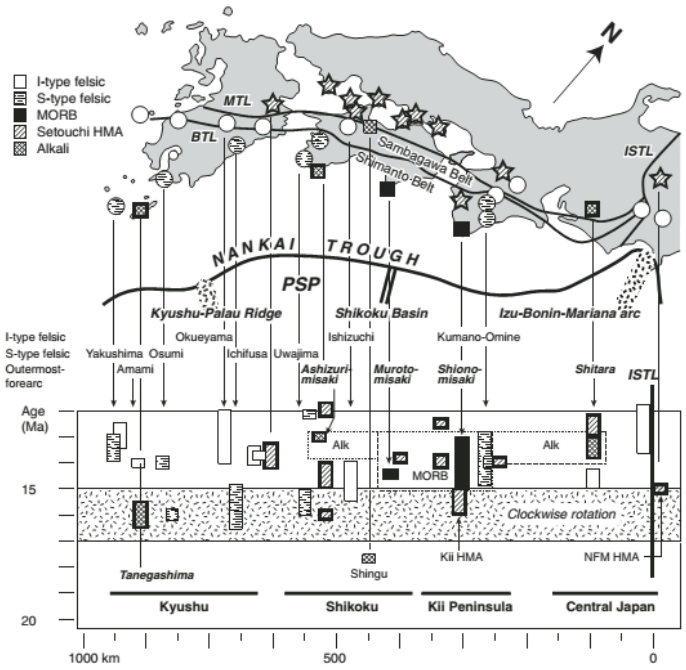

Figure 5. Volcanic activity along the SW Japan forearc during Sea of Japan opening. Alk = alkali basalt, HMA = high-magnesium andesite, NFM HMA = Northern Fossa Magna high magnesium andesite. PSP = Philippine Sea plate, MORB = mid oceanic-ridge basalt, MTL = median Tectonic Line, BTL = Butsuzo Tactonic Line, ISTL = Itoigawa Shizuoka Tactonic Line (Kimura *et al.*, 2005).

2.2 Shikoku Basin and Nankai accretionary prism

Ike *et al.* (2008) detailed the history of the Shikoku Basin. In the northern part of the Philippine Sea Plate, the basement structure of the Shikoku Basin was formed by the complex back-arc spreading history in the Izu-Bonin island arc during 27-15 Ma (Kobayashi and Nakada, 1978; Nakamura *et al.*, 1984; Okino *et al.*, 1994; Kimura *et al.*, 2014). Magnetic anomalies at the eastern and western sections of the basin trend dominantly NNW-SSE, reflecting the early seafloor spreading history (Okino *et al.*, 1994; Kobayashi *et al.*, 1995) that started ~27 Ma, when the Kyushu-Palau arc was split by back-arc spreading. Spreading proceeded at about 2.3-4.7 cm/yr until ~20-23 Ma. Seafloor spreading direction changed to NE-SW during 15-20 Ma, and this was the last true spreading phase in the Shikoku Basin (Okino *et al.*, 1994, 1999), but late-stage rifting may have continued until 7-10 Ma with associated volcanism that formed the Kinan Seamount Chain (Chamot-Rooke *et al.*, 1987; Ishii *et al.*, 2000). The ages of accretionary prism rocks collected from Sites 1178, 1175 and 1176 also suggested the current phase of subduction and accretion of the Shikoku Basin section probably started between late Miocene and Pliocene (Moore *et al.*, 2001c; Underwood and Steurer, 2003).

Ike *et al.* (2008) also defined four major seismic stratigraphic sequences of the Shikoku Basin that are correlated with lithologic units at ODP Leg 131 and 190. The base of the stratigraphic sequence is a thin volcaniclastic unit that overlies oceanic crust (Moore *et al.*, 2001c). Above this unit, it is the lower Shikoku Basin sequence which is the oldest mapped sediment. This sequence is correlated with the middle Miocene to lower Pliocene hemipelagic mudstone sampled at the ODP drill sites (Moore *et al.*, 2001a). The upper Shikoku Basin sequence overlies the lower Shikoku Basin sequence,

and is correlated with the Quaternary to Pliocene hemipelagic mudstone and an abundant ash and tuff unit (Figure 6).

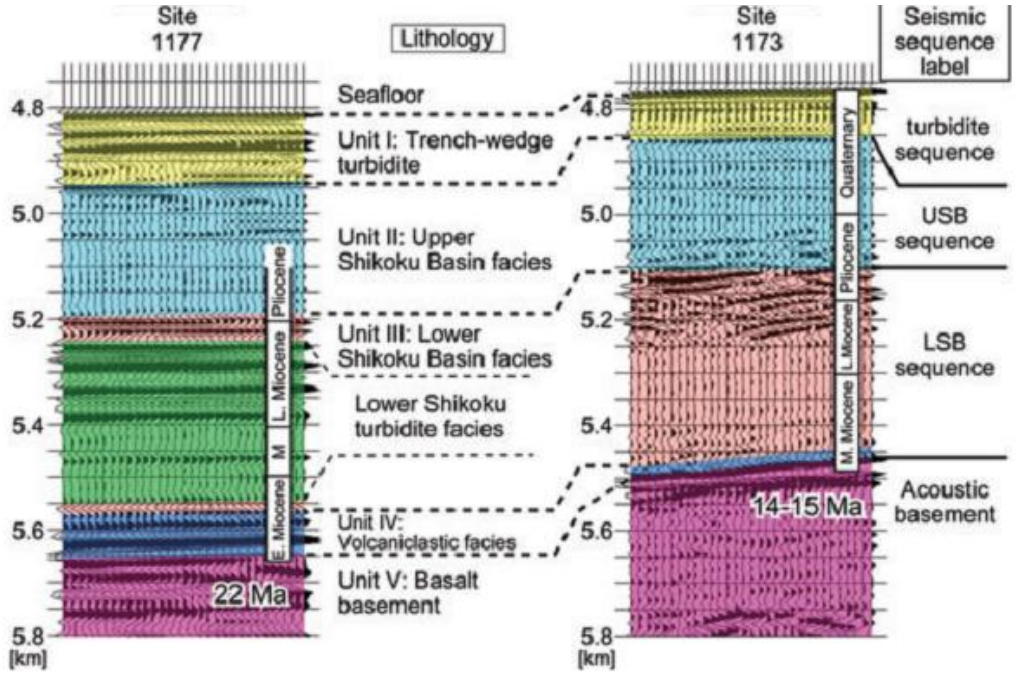

Figure 6. Seismic stratigraphy of the Shikoku Basin sediments (scale in km) correlated with stratigraphy at ODP Sites 1173 and 1177 (Ike *et al.*, 2008).

Nankai Trough is a convergent boundary caused by the subduction of the Phillippine Sea Plate beneath the Eurasian plate at an approximate rate of 4 cm/yr (Seno *et al.*, 1993; Miyazaki and Heki, 2001). The convergence direction is slightly oblique to the trench, and the Shikoku Basin plus trench wedge sediments are actively accreting at the deformation front. The Nankai accretionary prism on the landward side of the Nankai Trough mainly consists of offscraped and underplated materials from the trough fill turbidites and the Shikoku Basin hemipelagic sediments. This accretionary complex is one of the more intensively studied prisms in the world (Anma *et al.*, 2011). The rate of outbuilding of the accretionary prism is about 0.3 cm/year (Karig and Angevine, 1985).

The imbricated thrust slices of mélanges and trench turbidites of the Cretaceous-Tertiary Shimanto Belt on Shikoku, Honshu and Kyushu Islands show that accretion occurred in the Cretaceous (Ohmori *et al.*, 1997; Taira *et al.*, 1988; Taira and Tashihiro, 1987). Three transects, Ashizuri, Muroto and Kumano, in Nankai accretionary prism have been drilled by DSDP, ODP and IODP, and the prism architecture varies remarkably along-strike (Moore *et al.*, 2009; Saffer, 2010) (Figure 7). This variation of the prism can possible result from along-strike variations in the Shikoku Basin sedimentary sequence, where the Miocene-Pliocene turbidite sequence presented along the Ashizuri transect but not along the Muroto transect (Moore *et al.*, 2001).

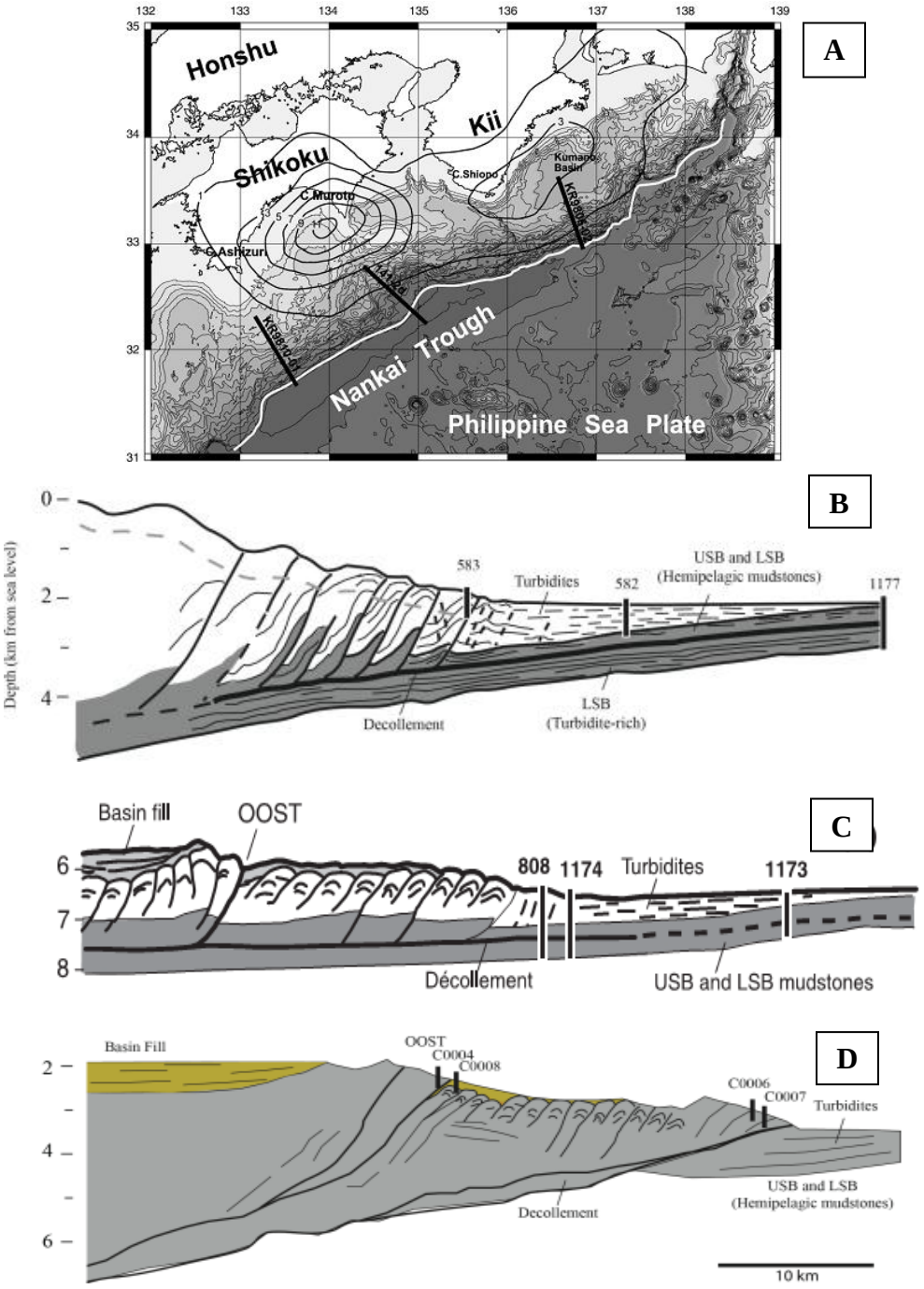

Figure 7. (A) Locations of seismic profile in (B), (C) and (D). (B) Ashizuri transect, (C) Muroto transect, and (D) Kumano transect. LSB = Lower Shikoku Basin, USB = Upper Shikoku Basin, OOST = out-of-sequence thrust (Kimura *et al.*, 2007; Saffer, 2010; Simpson, 2010; Moore *et al.*, 2001).

2.3 Kumano transect

The Kumano transect is in the region where rupture happened during the 1944 and 1946 earthquakes (Baba and Cummins, 2005). This part of the seismogenic zone is also the main target of NanTroSEIZE drilling project (Tobin and Kinoshita, 2006). Kopf *et al*. (2011) described the structure features of the Kumano transect (Figure 8). In the trench zone, younger trench deposits, the so-called trench wedge facies, overlie the oceanic crust and Shikoku Basin sediments. Farther landward, a well-developed protothrust zone has developed; however, it is overlain by a slice of trench strata previously accreted into the prism and emplaced over the trench strata by an out-of-sequence thrust (OOST). The frontal thrust zone (FTZ) appears highly complex with a very steep slope (~10 °) and a large embayment interpreted as slump scar possibly reflecting indentation by a recently subducted seamount (Screaton *et al.*, 2009b). Landward of the prism front is the imbricate thrust zone (ITZ) a series of thrust packages reflecting past in-sequence thrusting and accretion. The ITZ is overlain by slope sediments deposited in slope basins within the ridge-basin topography typical of fold-and-thrust belts developed in many accretionary prisms (e.g., Morley, 2009). Beneath the upper slope and Kumano Basin, a regional splay fault system, first recognized by Park et al. (2002) and later termed "megasplay" by Tobin and Kinoshita (2006), discontinuously cuts across the older part of the accretionary prism and intersects its shallow landward edge (Moore *et al.*, 2007; Moore *et al.*, 2009). The shallow part of the megasplay fault zone (MSFZ) is a complex thrust system with backward breaking branches that truncate the imbricate thrust faults within the accretionary prism and override younger slope basin sediments (Moore *et al.*, 2007; Strasser *et al.*, 2009). Landward of the MSFZ, along the

forearc high, the Kumano forearc basin is bounded on the southeast by a topographic valley. Décollement zone is the structural and mechanical boundary between the accreted and subducted sediments (Moore, 1989; Le Pichon and Henry, 1992). Further landward, this plate boundary fault system hosts the seismogenic zone (Rowe *et al.*, 2012).

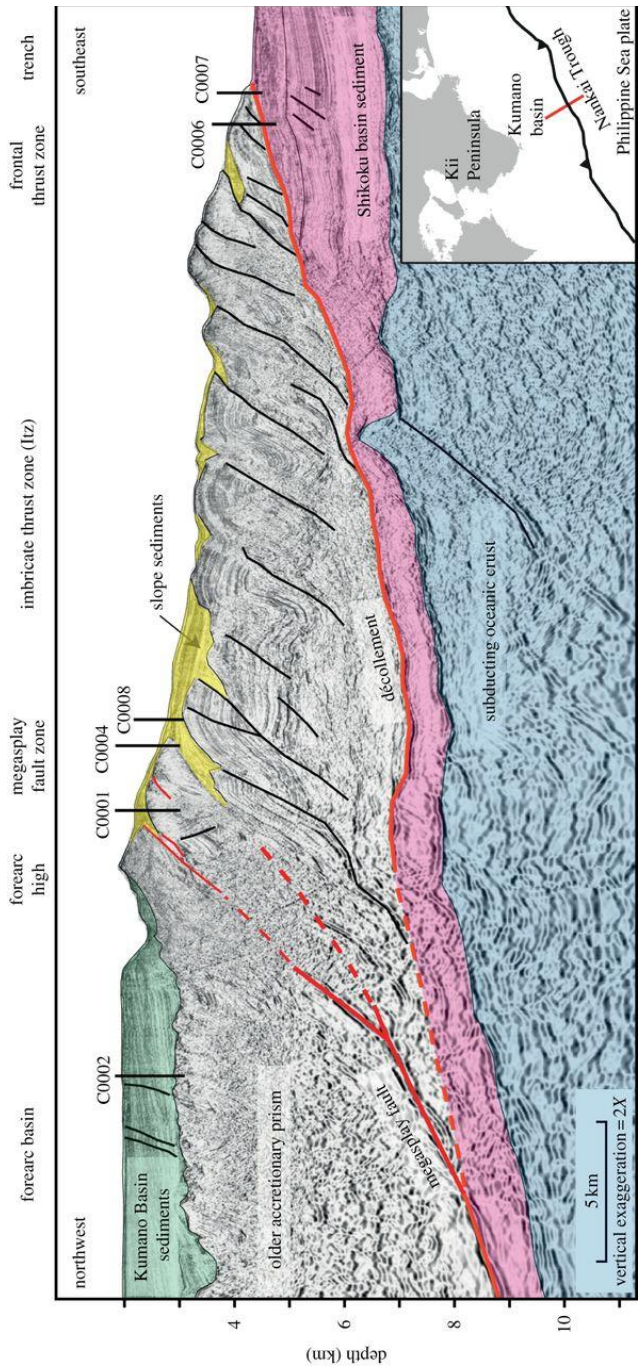

Figure 8. Structure features of Kumano transect (Futagami *et al.*, 2013).

The Kumano Basin is located on the eastern Nankai accretionary prism and is the largest forearc basin in the Nankai Trough. The Kumano Basin is 1-2 km in thickness and extends about 100 km in E-W and 70 km in N-S. On the north side of the basin, it is Shima Spur and continental slope off Kii Peninsula. Dai-ni Atsumi Knoll is on the east and outer arc high on the south. Based on the seismic data analyses, the basin can be divided into the north and the south zones, where there are three anticlines with 5-10 km intervals in the north zone, while in the south zone (except for the two anticlines in the east end), a large extended sedimentary basin is dammed up by uplift of the outer arc high (Figure 9) (Morita *et al.*, 2004).

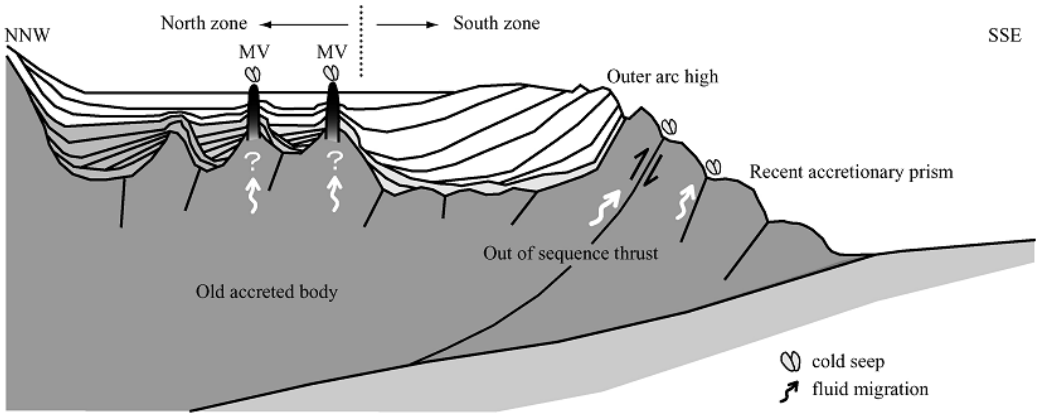

Figure 9. Schematic of the recent feature of the Kumano Basin (Morita *et al.*, 2004).

Underwood and Moore (2012) explained the evolution of structure and sedimentary environments of the Kumano transect. The out-of-sequence fault system, or megasplay, cuts across the older part of the accretionary prism and branches off the top of the plate interface between the basal accretionary prism and subducting igneous basement at ~10 km from the seafloor. Slip on the megasplay began at ~1.95 Myr by out-of-

sequence thrusting near the prism toe and was reactivated as a major splay fault at ~1.55 Myr (Strasser *et al.*, 2009). As for the Kumano Basin, it rests above upper Miocene to lower Pliocene aged accretionary prism, and most of the basin-fill accumulated within the last 1.6 Myr. During the Pleistocene, the influx of turbidite sand to the forearc basin was probably accelerated by incision of submarine canyons and slope gullies across the upper continental margin together with rapid uplift and erosion of sediment sources on the nascent Japanese Islands (Underwood and Moore, 2012).

2.4 Previous expeditions for NanTroSEIZE

NanTroSEIZE Stage 1 included IODP Expeditions 314, 315, and 316. There were eight sites for riserless drilling to target the frontal thrust region, the midslope megasplay fault region and the Kumano forearc basin. The purpose of Expedition 314 was to measure the in-situ physical properties and image the borehole through logging while drilling (LWD) (Tobin *et al.*, 2009). Expedition 315 cored and measured downhole temperature at sites in the megasplay region and the forearc basin (Ashi *et al.*, 2009). Expedition 316 focused on the frontal thrust and megasplay fault in their shallow, aseismic portions (Screaton *et al.*, 2009).

There were four Expeditions (319, 322, 332, and 333) during NanTroSEIZE Stage 2. This stage was devoted to (Expedition 319 Scientists, 2010; Underwood *et al.*, 2010; Expedition 332 Scientists, 2011; Expedition 333 Scientists, 2012): (1) characterizing the subduction inputs from the Philippine Sea plate; (2) preparing for later observatory installations for long-term monitoring of deformation at the updip limit of the seismogenic zone.

NanTroSEIZE Stage 3 includes Expeditions 326, 338 and 348 and mainly focused on Site C0002. During Expedition 326, a 20-inch casing string was installed in Hole C0002F to 860 mbsf (Expedition 326 Scientists, 2011). The hole was deepened to ~2010 mbsf (rather than targeted 3600 mbsf due to the mechanical and weather related events) in Expedition 338. There was no additional casing installed, but a complete set of logs and cuttings were still collected. Expedition 348 sampled and logged a deeper interval within the inner accretionary wedge, from 856 to 3058.5 mbsf (new scientific drilling record) in Holes C0002N (sidetracked from Hole C0002F) and C0002P (sidetracked from Hole C0002N), including a never-before sampled zone in the lowermost ~1 km of drilling (Expedition 348, 2015). It also collected a full suite of LWD logs, as well as cuttings at ~5 m intervals and cores at a 55.5 m interval from 2163 to 2218.5 mbsf. See Figure 2 for all drilling sites from three stages in NanTroSEIZE region.

2.5 Summary of sites C0002 and C0009

Site C0002 is the centerpiece of the NanTroSEIZE project (Figure 10). Clusters of very low frequency earthquakes have repeated in this zone (Ito and Obara, 2006; Sugioka *et al.,* 2012), and the first tectonic tremor was recorded in an accretionary prism setting (Obana and Kodaira, 2009). One goal of NanTroSEIZE is to reach the location that has slipped coseismically in the 1944 Tonankai earthquake. That portion of the megasplay is capable of seismogenic locking and slip in this plate interface fault system (Ichinose *et al.*, 2003).

IODP Site C0009 was drilled during Expedition 319 approximately 20 km northwest of Site C0002 (Figure 10). One of the objectives of this site was to collect core

and cuttings within the forearc basin and underlying units to characterize the lithology, depositional history, physical properties and deformation of the Kumano Basin and upper accrretionary prism (Expedition 319 Scientists, 2010b). In the upper section of Site C0009, seismic reflectors can be traced to Site C0002, which suggests widely divergent sediment deposition rates between the two sites during basin history (Expedition 319 Scientists, 2010b).

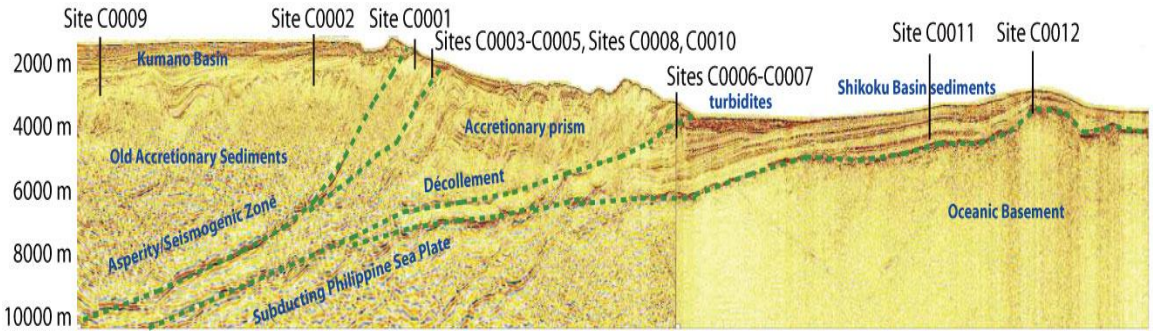

Figure 10. Seismic profile along the Nankai Trough axis, showing major geologic features along the transect encompassing all NanTroSEIZE drill sites (Expedition 322 Scientists, 2010).

Four lithologic units were described at both Site C0002 (shallow part) and Site C0009 (Figure 11). Unit IV (~5.6 to 7.9 Ma) is mudstone with thin-bedded, fine-grained turbidites, interpreted as accretionary prism material. This unit is significantly deformed and has limited evidence of carbonate deposition. Unit III (~0.9 to 3.8 Ma) is about 5 times thicker at Site C0009 than at Site C0002. There are two subunits (IIIA and IIIB) at Site C0009: silt, ash beds and abundant wood and lignite are present. It is interpreted as a condensed mudstone section deposited in the early forearc basin at Site C0002 (Ashi *et al.*, 2009). Subunit IIIB at Site C0009 is interpreted as early forearc basin or slope deposits and considered to be laterally equivalent to Unit III at Site C0002. At both locations, sediments grade upward from mudstone (Unit III) to interbedded mudstone and

sandstone (Unit II, <0.9 to ~0.9 Ma), but it is greatly expanded at Site C0009. These strata record infilling of the Kumano Basin and sediment deposition progressively migrating to the northwest as uplift occurred on the megasplay fault (Expedition 319 Scientists, 2010b).

Three lithologic units (III, IV, V) were defined at Hole C0002F during Expedition 338 (Expedition 338 Scientists, 2014) with greenish grey silty claystone as the dominant lithology. Four lithologic units were identified at Site C0002 during Expedition 348 based on geological and geochemical characteristics of core and cuttings samples (Figure 7). Lithologic Unit II (475-512.5 mbsf in Hole C0002M) is interpreted to be the upper Kumano forearc basin sediments and is dominated by the hemipelagic mud (Expedition 315 Scientists, 2009). Silty claystone is the main lithology, with subordinate fine-grained sandstone and sandy siltstone. Lithologic Unit III (875.5-975.5 mbsf in Hole C0002N) in Hole C0002N is interpreted to be the lower part of Kumano forearc basin sediment. It is dominated by silty claystone with trace amounts of very fine loose sand, containing common glauconite grains. Lithologic Unit IV (975.5-1665.5 mbsf in Hole C0002N) in Hole C0002N is divided into five subunits based on sand content and is interpreted as the upper accretionary prism sediment. Silty claystone is the dominated lithology, with sandstone (appearing as disaggregated loose sand in cuttings) as a minor lithology. Lithologic Unit V (1665.5-2325.5 mbsf in Hole C0002N, and 1965.5-3058.5 mbsf in Hole C0002P) in Holes C0002N and C0002P is interpreted to be accreted trench or Shikoku Basin hemipelagic deposits, similar to the hemipelagic facies at Sites C0011 and C0012 (Expedition 322 Scientists, 2010). The major lithology is also silty claystone. From 875.5 to 3058.5 mbsf, cuttings and core samples contain fossil assemblages ranging

in age from the late Pliocene to late Miocene. Bedding is steep to vertical (~70-80°) in the cored interval of this unit (Figure 12).

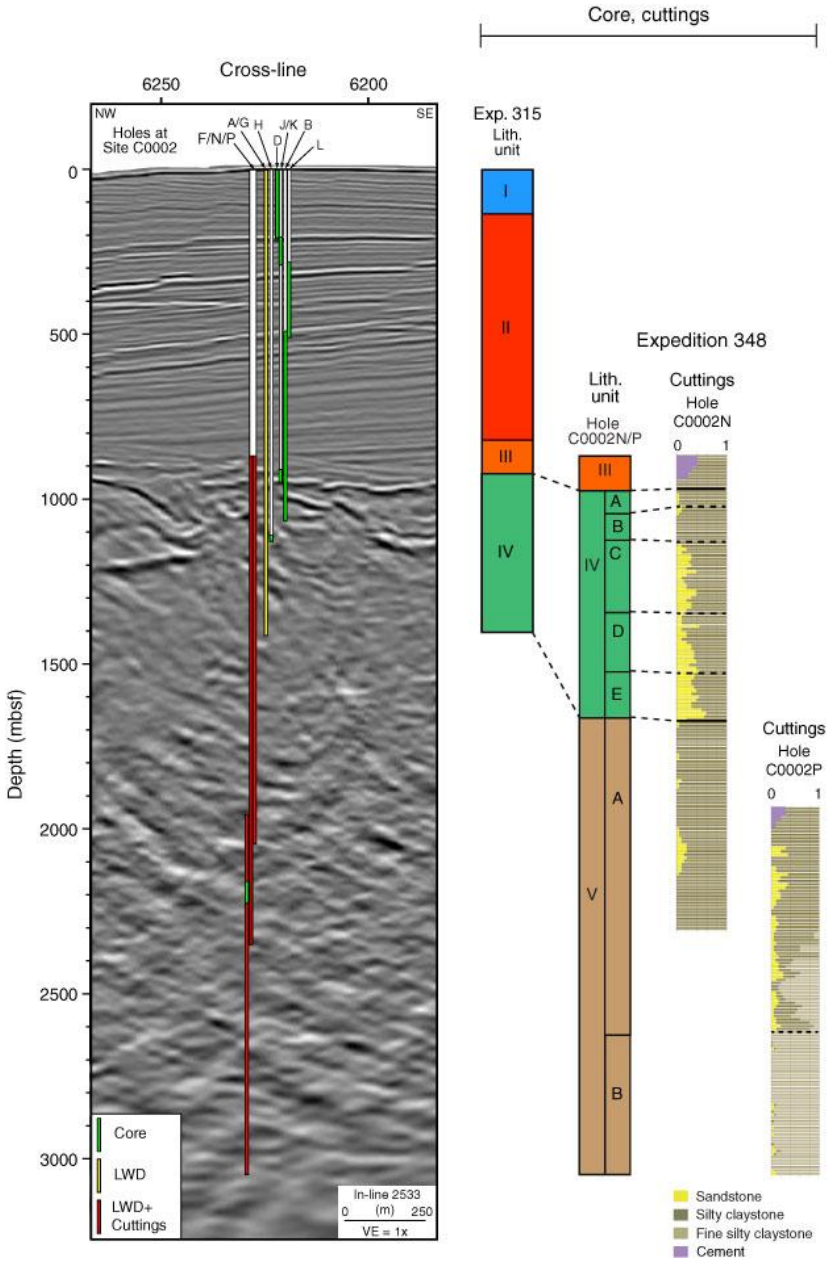

Figure 11. Stratigraphy of site C0002. Lithologic unit boundaries are from Expeditions 315, 338, and 348 (Expedition 348 Scientists, 2015b).

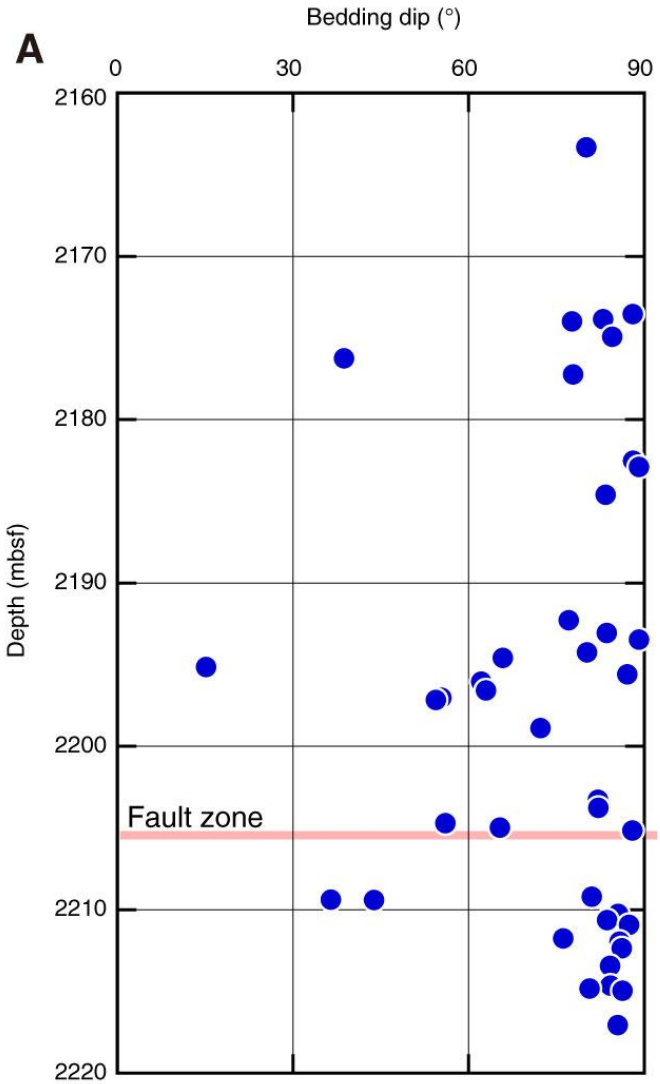

Figure 12. Plot of depth versus bedding dip distribution at Hole C0002P (Expedition 348 Scientists and Scientific Participants, 2014).

Chapter 3 Methods

3.1 Recovery of cuttings and core samples

A total of 293 cuttings samples were collected from the shale shakers between 870.5 and 2330 mbsf in Hole C0002N and 231 cutting samples between 2107.5 and 3058.5 mbsf in Hole C0002P at a 5-m depth interval. After washing and sieving, cuttings samples were classified using a sequential material number followed by an abbreviation describing the type of material and size fraction. For example, "348-C0002N-123-SMW, 1–4 mm" (for the 1–4 mm size fraction aliquot of the one hundred twenty-third cuttings sample recovered from Hole C0002N during Expedition 348; SMW = solid taken from drilling mud) (Expedition 348 Scientists, 2015a).

Six whole-round (WR) samples were collected over a 55.5 m coring interval from 2163 to 2218.5 mbsf at Hole C0002P. The overall core recovery was 56.7% (minimum 4.2% and maximum 86.0%). Each core was cut into different sections and labeled successively from top to bottom. Each interval from different sections was measured in centimeters from top of the section. A sample identification number of "348-C0002P-3R-01, 51 cm" would indicate the following:

348	C0002	P	3	R	01	51
(Expedition)	(Site)	(Hole)	(Core)	(Technique)	(Section)	(Interval)

3.2 Sample preparation for constant flow test

3.2.1 Sample preparation

Four whole-round specimens from depths of 2174.98 to 2209.64 mbsf were obtained for constant-flow permeability tests with a focus on thin interbeds of silty claystone and fine-grained turbidites. The samples are from lithostratigraphic Unit V (accreted trench or Shikoku Basin hemipelagic deposits). The WR samples were capped and taped in their plastic core liners on board the *D/V Chikyu*, sealed with wet sponges in aluminum vacuum bags to prevent moisture loss, and stored at ~4 ℃ until immediately prior to trimming. Specimens were easy to extract from the core liners without cutting the liners open. Cylinders for tests in the vertical (along-core) direction were trimmed using a razor blade and knife (Figure 13).

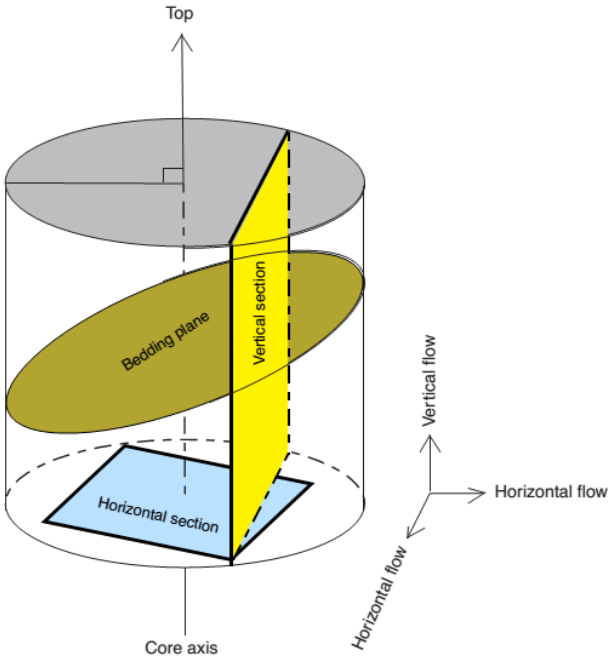

Figure 13. Illustration representing the horizontal and vertical section of core.

The length after trimming was 3.6 to 7.8 cm and averaged 5.46 cm, as measured by caliper to a resolution of 0.02 mm. The diameter was 3.8 to 4.5 cm and averaged 4.0 cm. WR cylinders were not long enough to trim to comparable dimensions in the horizontal (cross-core) direction. The WR specimens are heterogeneous and some intervals contain thin (~1.3 cm) oblique silty layers and black bands. Steeply dipping bedding is also present in the specimens, which can be seen through the patterns after the specimens broke (Figure 14).

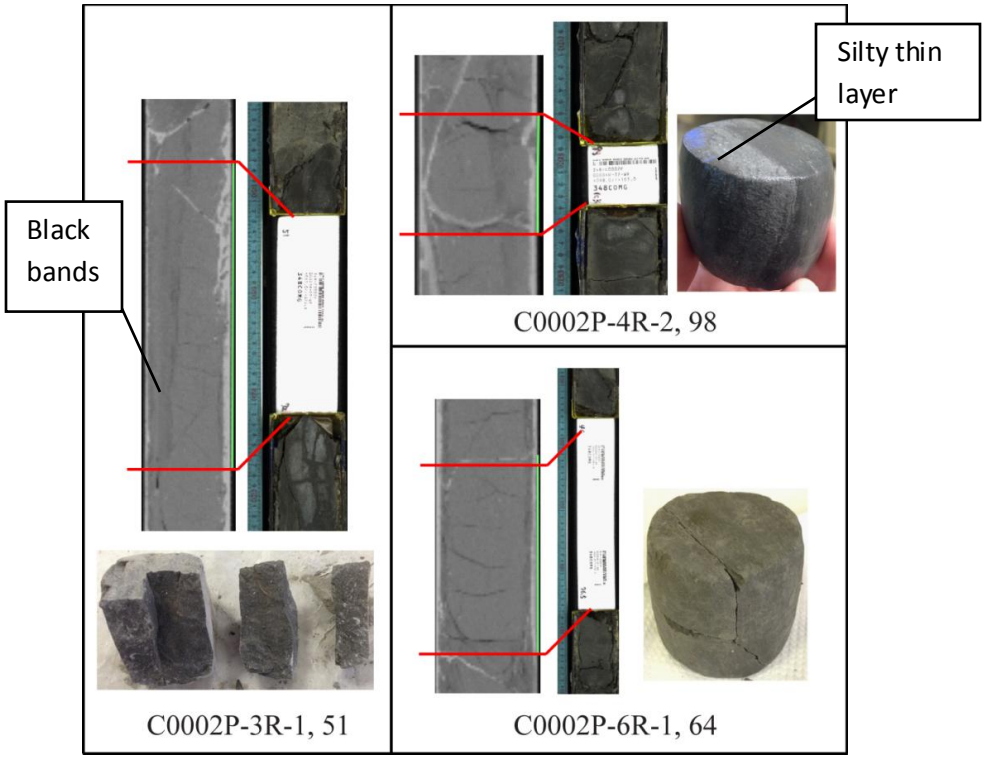

Figure 14. X-ray computed tomography (XRCT) images and photos showing different features presented in the WR specimens.

For most samples, I calculated values of initial (pre-test) and post-test porosity from measurements of gravimetric water content. This was done by oven-drying the trimmings at 105 ℃ in accordance with shipboard protocols (Expedition 348 Scientists,

2015a) and by assuming 100% pore water saturation. However, the samples dried out quickly during the trimming so the pre-test porosities may be inaccurate. Values of grain density and comparable shipboard porosity were imported from shipboard measurements of the closest adjacent specimen. A correction for pore-water salt content was applied using:

$$W_c = (M_t - M_d) / (M_d - rM_t), \quad (1)$$

where

W_c = corrected dry weight,

M_t = total mass of saturated specimen,

M_d = mass of dried specimen, and

r = salinity (per mil).

For salt corrections on pre-test trimmings, we assumed an average interstitial salinity value of 35‰; for post-test trimmings, we assumed a value of 25‰ to approximate the simulated seawater that was used to saturate specimens.

3.2.2 Constant-flow apparatus

Yue *et al.* (2012) provided a thorough description of the instrumentation and testing procedures for permeability at the University of Missouri-Columbia (USA). To summarize, the system consists of an acrylic confining cell, a constant-flow syringe pump, one differential pressure transducer to measure hydraulic head difference between the specimen top cap and bottom cap, and an air/water interface panel for regulating the

confining fluid pressure and backpressure (Figure 15). Signals from the differential pressure transducer permit calculations of hydraulic head difference (Δh) at a precision of ± 1 cm H_2O over a range of ± 1000 cm H_2O. A digital interface also records values of effective isotropic confining stress (σ') and elapsed time. A syringe pump (KDS Scientific, Model 260) simultaneously injects and extracts pore fluid from opposite ends of the specimen. The flow pump holds one syringe (Hamilton GasTight Series 1000) to infuse pore fluid into one end, while another syringe withdraws an equal volume of fluid from the other end at the same rate.

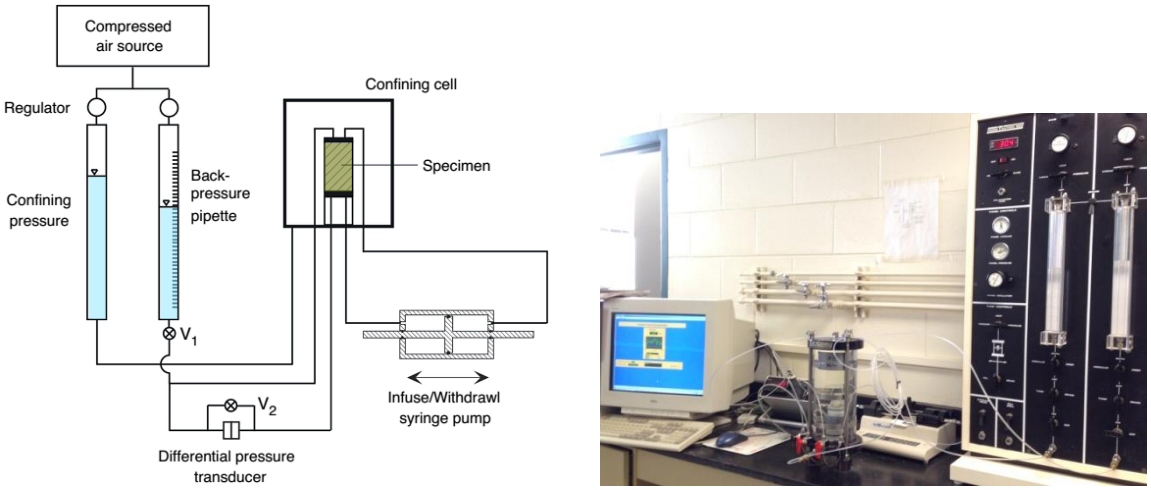

Figure 15. Schematic and picture of permeability testing system at University of Missouri.

3.2.3 Backpressure saturation

Prior to my tests, all permeant lines and porous stones are saturated with simulated seawater (25 g NaCl to 1 L tap water). After placing a specimen on the pedestal, the top cap is attached, and a latex membrane is added to encase the cylinder using a vacuum membrane expander. The confining chamber is then sealed and the cell

filled with tap water. Saturation is achieved by ramping pore-fluid backpressure to 0.48 MPa (70 psi) using the panel board (air/water interface) while also ramping the confining pressure to maintain an effective isotropic confining stress of 0.034 MPa (5 psi). The elevated backpressure is maintained for at least 24 h. We confirm saturation by increasing the confining pressure to 0.55 MPa (80 psi) and measuring the corresponding pore pressure (u) response, which yields Skempton's B-value ($B = \Delta u/\Delta\sigma$). Specimens are "saturated" if $B \geq 0.95$ or if a B-value < 0.95 remains constant for more than 48 h. After saturation, the cell pressure is increased to consolidate the specimen at an isotropic effective stress of 0.28 MPa (40 psi) first. Pore water drains during consolidation from both the top and bottom of the specimen by opening valves on the confining cell. The volume of expelled pore water is measured using the backpressure pipette and monitored for equilibrium to calculate the corresponding volume change of the specimen. After the permeability tests are finished at this effective stress, the same specimen is consolidated at an effective stress of 0.55 MPa (80 psi) to run a new series of tests.

3.2.4 Constant-flow permeation

In this research project, two samples trimmed vertically (parallel to the core axis) were tested under two different isotropic effective stresses, 0.28 MPa (40 psi) and 0.55 MPa (80 psi). One sample trimmed vertically was tested only under 0.28 MPa because the sample fell apart during loading to 0.55MPa. With each effective stress, four flow-through tests were conducted with two different flow rates and two different flow directions. Steady state head difference (Δh_s) was monitored by the differential pressure transducer during each test (Figure 16).

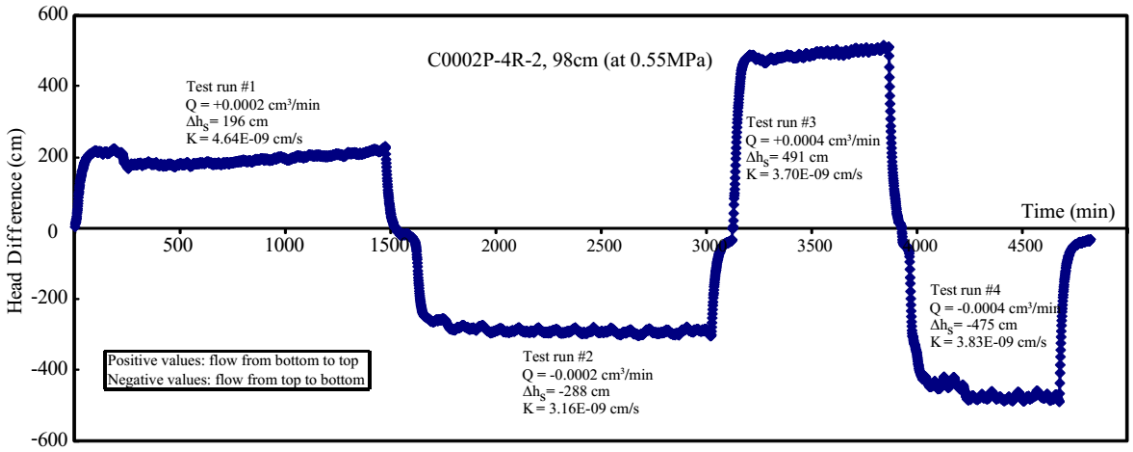

Figure 16. Example of typical responses of transient head difference (Δh_s) during flow-through test. Q = volumetric flow rate, K = hydraulic conductivity.

3.2.5 Constant-flow test data analysis

Hydraulic conductivity (K) is defined as the ease with which fluid will flow through a porous medium by Darcy's Law. I calculated the value of hydraulic conductivity (K, in units of m/s) for each specimen using Darcy's Law:

$$Q = K\, i_s\, A = K\, (\Delta h_s / \Delta L)\, A \qquad (2)$$

where

Q = applied volumetric flow rate (L^3/T),

i_s = steady-state hydraulic gradient,

Δh_s = steady-state head difference (L),

ΔL = length over which head difference occurs (initial height of the specimen, L),

A = cross-sectional flow area (initial specimen area, L^2).

The corresponding value of discharge velocity is computed using: $v = Q/A$. Intrinsic permeability (k) is also defined as the ability of a porous material to allow fluids

to pass through it, but it is a function of only matrix, not fluid properties. Permeability is affected by the size and degree of interconnection of pore space (Schwartz and Zhang, 2003). Conversion of hydraulic conductivity to values of intrinsic permeability (in units of m^2) takes the permeant properties into account:

$$k = (K\ \mu) / (\rho\ g), \quad (3)$$

where

μ = viscosity of permeant at room temperature (0.001 Pa·s at 25˚C),

ρ = density of permeant (1027 kg/m^3),

g = gravitational acceleration (9.81 m/s^2).

3.3 X-ray diffraction for bulk powder and clay-size fraction

3.3.1 Bulk mineralogy

The principal goal of shipboard X-ray diffraction was to estimate the relative weight percentages of total clay minerals, quartz, feldspar, and calcite in bulk samples. Expedition 348 Scientists (2015b) described the procedures used for shipboard XRD analyses. For cuttings, XRD analysis was conducted on 10 g subsamples of the 1-4 mm and > 4 mm size fractions every 10 m. For cores, material for XRD was obtained from a 10 cc sample that was also used for XRF and carbonate analyses. All samples were vacuum dried, crushed with a ball mill, and mounted as randomly oriented bulk powders. Routine shipboard XRD analyses of bulk powders were performed using a PANalytical CubiX PRO (PW3800) diffractometer with the settings as follows: Generator = 45 kV; Current = 40 mA; Tube anode = Cu; Wavelength = 1.54060 Å (Kα1) and 1.54443 Å (Kα2); Step spacing = 0.005°2θ; Scan step time = 0.648 s; Divergent slit = automatic; Irradiated length = 10 mm; Scanning range = 2°-60°2θ; Spinning = yes.

In order to maintain consistency with previous NanTroSEIZE results, MacDiff 4.2.5 was used for data processing (www.ccp14.ac.uk/ccp/ccp14/ ftp-mirror/krumm/Software/macintosh/macdiff/MacDiff.html). Each peak's upper and lower limits were adjusted by following the guidelines shown in Table 1.

Table 1. Characteristic X-ray diffraction peaks for semiquantitative analysis of bulk powder (Expedition 348 Scientists, 2015a).

Mineral	Reflection	d-value (Å)	Peak position (°2θ; area)
Composite clay	Multiple	4.478	19.4–20.4
Quartz	101	3.342	26.3–27.0
Plagioclase	2	3.192	27.4–28.2
Calcite	104	3.035	29.1–29.7

Calculations of relative mineral abundance utilized a matrix of normalization factors derived from integrated peak areas and Singular Value Decomposition (SVD). As described by Fisher and Underwood (1995), calibration of SVD factors depends on the analysis of known weight-percent mixtures of mineral standards that are appropriate matches for natural sediments. SVD normalization factors were recalculated during Expedition 338 (Table 2). The mixtures were rerun at the beginning of Expedition 348.

Table 2. Normalization factors for calculation of relative mineral abundance using bulk powder X-ray diffraction analysis as revised during Expedition 338 (Expedition 348 Scientists, 2015a).

In standard mixture	Normalization factors			
	Total clay	Quartz	Plagioclase	Calcite
Influencing mineral:				
Total clay	0.11006193E–01	–0.20231483E–03	–0.29246596E–03	–0.11871842E–02
Quartz	–0.14089397E–04	0.58841606E–03	–0.24897352E–04	–0.23400669E–04
Plagioclase	0.49289758E–03	–0.71762974E–04	0.11238736E–02	–0.41371561E–04
Calcite	0.56265158E–04	–0.41641979E–05	–0.50802228E–05	0.13876300E–02

Bulk powder mixtures for the Nankai Trough are the same as those reported by Underwood *et al.* (2003): quartz (Saint Peter sandstone), feldspar (Ca-rich albite), calcite (Cyprus chalk), smectite (Ca-montmorillonite), illite (Clay Mineral Society IMt-2, 2M1 polytype), and chlorite (Clay Mineral Society CCa-2) (Figure 17).

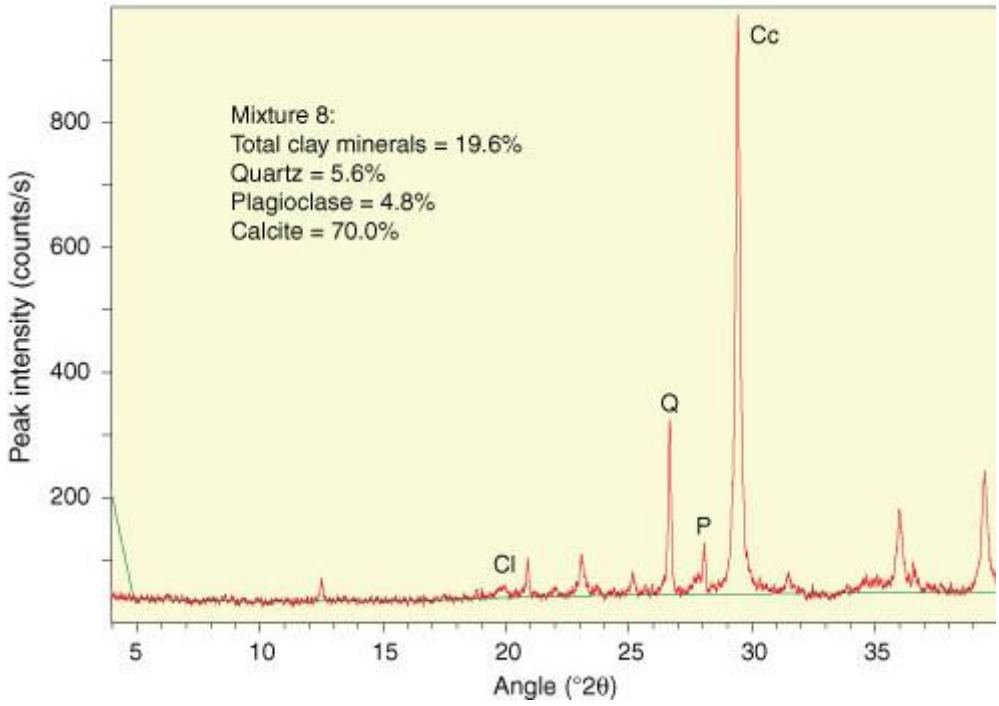

Figure 17. Example of X-ray diffractograms for one bulk standard minerals mixture showing the positions of diagnostic peaks used to calculate relative mineral abundance (green line represents baseline subtraction) (Expedition 348 Scientists, 2015a).

Average errors (SVD-derived estimates versus true weight percent) of the standard mineral mixtures are: total clay minerals = 3.3%; quartz = 2.1%; plagioclase = 1.4%, and calcite = 1.9%. One of the fundamental problems with any bulk powder XRD method is the difference in peak response between poorly crystalline minerals at low diffraction angles (e.g., clay minerals) and highly crystalline minerals at higher diffraction angles (e.g., quartz and plagioclase). Clay mineral content is best characterized by measuring the peak area, whereas peak intensity may more accurately

quantify quartz, feldspar, and calcite. Analyzing oriented aggregates enhances basal reflections of the clay minerals, but this is time consuming and requires isolation of the clay-size fraction to be effective. For clay mineral assemblages in bulk powders, the two options are to individually measure one peak for each mineral and add the estimates together (thereby propagating the error) or to measure a single composite peak at 19.4 °-20.4° 2θ. Other sources of error are contamination of mineral standards by impurities such as quartz (e.g., the illite standard contains ~20% quartz) and differences in crystallinity between standards and natural clay minerals. For trace quantities of a mineral and peaks with low intensity, use of negative SVD normalization factors may result in negative values of absolute weight percent. In such cases, I inserted the numerical value of 0.1% as a proxy for "trace". Calculated mineral abundances should be regarded as relative percentages within a four-component system of clay minerals + quartz + feldspar + calcite. How close those estimates are to their absolute percentages within the total solids depends on the abundance of amorphous solids (e.g., biogenic opal and volcanic glass), as well as the total of all other minerals that occur in minor or trace quantities. For most natural samples, the difference between calculated and absolute abundance percentage is probably between 5% and 10%. To compound the error, the XRD data from cuttings show effects of contamination by drilling fluids. The severity of these artifacts is especially obvious in the calculated values of percent calcite (Expedition 348 Scientists, 2015a).

3.3.2 X-ray diffractometer used for clay-size fraction

A X-ray diffractometer was used at New Mexico Bureau of Geology & Mineral Resource in New Mexico Institute of Mining and Technology to scan slides from 3 °to

26.5°2θ at the following parameters: Anode material = Cu; Scan step time = 1.6 s; Step size = 0.01°2θ; Voltage = 45 kV; Current = 40 mA; Irradiated length = 0.5 mm; Receiving slit size = 0.1 mm (receiving); Measurement temperature = 25 °C; Spinning = yes. MacDiff software (version 4.2.5) was used to process the digital data (Petschick, 2001) to establish a baseline of intensity, smooth counts, and correct peak positions (using the quartz (100) peak at 20.85°2θ; d-value = 4.24 Å), and calculate integrated peak areas (total counts).

3.3.3 Sample preparation for clay mineralogy

There are several steps of sample preparation for XRD analyses of clay-size fractions. First, approximately 5 cubic centimeters of sediment are gently crushed and placed in a 600 ml glass beaker with 3% H_2O_2 for at least 24 hours to let the reaction of organic matter digestion complete. Second, 250 ml of dispersant solution (4 g sodium hexametaphosphate per 1 L deionized H_2O) are added to the beaker to disperse the clay particles. After disaggregating the samples with the ultrasonic bath, a Marathon 21K centrifuge is used to wash the sample (six 60 ml tubes per sample at 8200 rpm for 25 min). Each sample is washed twice. After disaggregation with an ultrasonic cell disrupter, the <2 μm fraction is isolated using a centrifuge at 1000 rpm for 2 minutes and 24 seconds then the 2-μm fraction is transferred to glass slide using the filter-peel method (Moore and Reynolds, 1989) with a 0.45 μm membrane. Ethylene glycol vapor is used to saturate the clay aggregates for at least 24 hours prior to XRD analysis, using a closed vapor chamber heated to 60°C in an oven.

3.3.4 Calculating relative clay mineral abundances

The accuracy of estimating the relative abundance of a mineral in the clay-size fraction is quite challenging (Moore, 1968). One common method is to multiply the Biscaye (1965) weighting factors by the peak areas of basal reflections and normalize to 100% (McManus, 1991). However, the accuracy is affected by the absolute abundance by weight of each mineral in the mixture (Underwood *et al.*, 2003). XRD results are also affected by sample disaggregation technique, chemical treatments, particle size separation, crystallinity and chemical composition of minerals, peak-fitting algorithms and the degree of preferred orientation of clay mounts (Moore and Reynolds, 1989; Ottner *et al.*, 2000). In order to improve the accuracy, SVD was used on standard mineral mixtures (Underwood *et al.*, 2003) to compute a matrix of normalization factors for clay-size fraction (Table 3).

Table 3. Normalization factors for calculation of relative mineral abundance of clay-size fraction using X-ray diffraction.

In standard mixture	Normalization factors			
	Smectite	Illite	Chlorite	Quartz
Influencing mineral:				
Smectite	7.4475294E-04	-3.1953641E-05	-7.5067212E-05	-1.5661915E-04
Illite	6.3114654E-05	3.7866938E-03	8.4222964E-05	1.1769286E-04
Chorite	-3.5636057E-04	-6.7378140E-05	2.5121504E-03	5.2290707E-05
Quartz	9.3573136E-03	3.6491468E-03	3.2755411E-03	1.4825645E-02

I calculated relative weight abundance by measuring the integrated peak areas for basal reflections of smectite, illite, kaolinite, chlorite, and quartz. The targeted peaks are (Figure 18): smectite (001) at ~5.3° 2θ (d-value = 16.5 Å); illite (001) at ~8.9° 2θ (d-value = 9.9 Å); the composite chlorite (002) + kaolinite (001) at ~12.5° 2θ (d-value = 7.06 Å); and quartz (100) at 20.85° 2θ (d-value = 4.26 Å). However, the chlorite (001)

peak occurs on the shoulder of the glycol-solvated smectite (001) peak at ~14 Å, so the limits for peak area was adjusted to subtract the counts generated by chlorite (Underwood and Guo, 2013). Average errors for the standard mineral mixtures used to calibrate this method are approximately 3.5% for smectite, 1% for illite, 1.9% for chlorite and 1.6% for quartz.

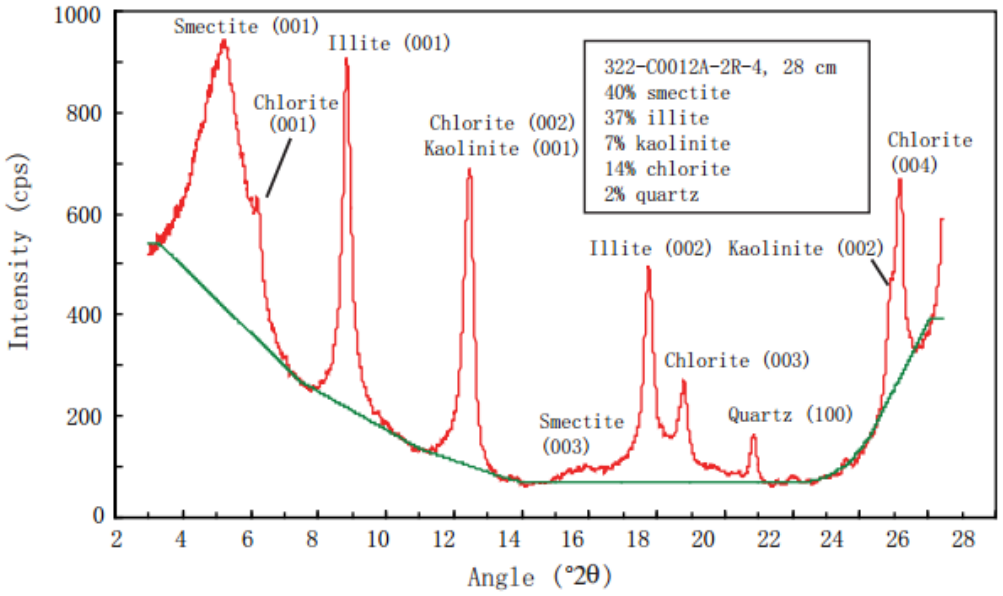

Figure 18. Representative example of X-ray diffractograms showing peaks for smectite, illite, chlorite, kaolinite and quartz (Underwood and Guo, 2013).

3.3.5 Calculating percentages of kaolinite and chlorite

Because of the nearly total overlap peaks between chlorite (002) and kaolinite (001) at ~7.06 Å, the relative abundance as undifferentiated chlorite and kaolinite was calculated first. The proportion of each mineral was solved by using the double peak at ~25° 2θ. Guo and Underwood (2011b) described the method as follows.

By using MacDiff software (version 4.2.5), offset of peak positions caused by misalignment were corrected to either kaolinite (002) at ~24.8° 2θ (d-value = 3.58 Å) or chlorite (004) at ~25.1° 2θ (d-value = 3.54 Å). The corrected peak profiles were used to

locate the centers of peaks and when both crests are resolved, angular separation between the two overlapping peaks averages 0.27° 2θ. Through the results of all the diffractograms generated for the standard mixtures, Guo and Underwood (2011b) found that one side of the dominant peak is not distorted by interference from the minor peak, and using the undistorted side makes it easy to compute the dominant peak's total area by multiplying its half-peak area by 2× (Figure 19). One important assumption is peak symmetry, which does not necessarily hold true for natural mixtures of clay minerals (Moore and Reynolds, 1997). But the ratio of the dominant peak area (PA) to the total area (TA) of the composite peak should correlate with each mineral's abundance. For mixtures in which both peak crests are distinct each mineral's undistorted half-peak area was measured and doubled to compute both of the respective PA values.

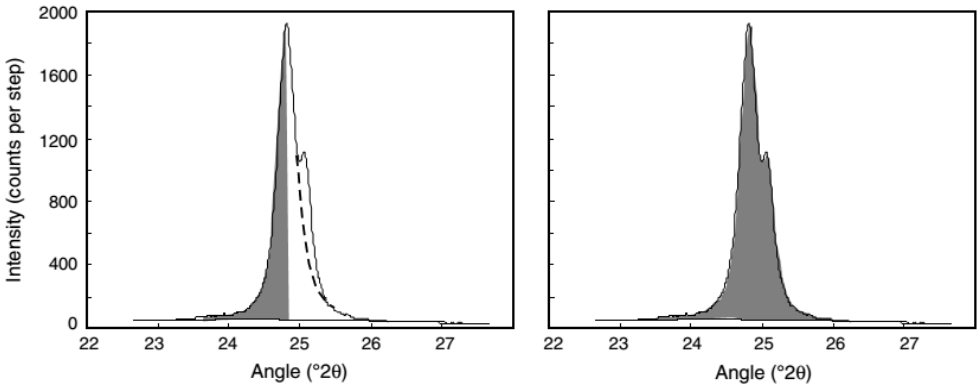

Figure 19. X-ray diffractogram of a typical kaolinite and chlorite standard mixture. The regions highlighted in gray show how to measure the half peak area and the total peak area. The dashed line helps outline the dominant peak (Guo and Underwood, 2011b).

Guo and Underwood (2011b) constructed two equations. For kaolinite-dominant specimens:

$$\text{Kaolinite wt\%} = 100 \times (\text{PA/TA})^{1.613} \qquad (4)$$

For chlorite-dominant specimens:

$$\text{Chlorite wt\%} = 100 \times (\text{PA/TA})^{1.433} \qquad (5)$$

In this study, I used equation (5) to calculate the abundance of chlorite, then subtracted the chlorite wt% from the total abundance of kaolinite/chlorite to get the abundance of kaolinite.

3.3.6 Calculating expandability of illite/smectite mixed-layer clay

As an indicator of clay diagenesis, the saddle/peak method (Rettke 1981) was used to calculate the percent expandability of smectite and illite/smectite (I/S) mixed-layer clay (Figure 20). This method is sensitive to the proportions of discrete illite versus I/S mixed-layer clay.

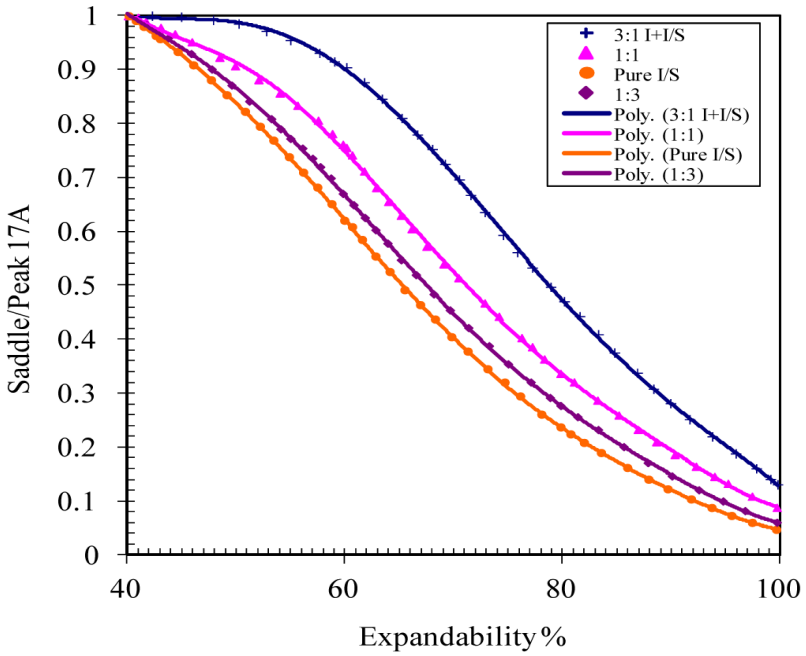

Figure 20. Plot of "saddle"/peak intensity ratio as a function of I/S expandability for pure I/S and for various mixtures of I/S with discrete illite (modified after Rettke 1981)

Four equations are developed from Figure 20 (I = illite; I/S = illite/smectite; x = expandability; y = "saddle"/peak intensity ratio), and equation (7) is used in this study:

For I: I/S = 3:1,

$$x = -3972.8y^6 + 12381y^5 - 15187y^4 + 9251.1y^3 - 2877.1y^2 + 364.18y + 84.286, \quad (6)$$

For I: I/S = 1:1,

$$x = 653.09y^6 - 2309.2y^5 + 3079.7y^4 - 2029.1y^3 + 743.2y^2 - 211.19y + 113.85, \quad (7)$$

For I: I/S = 1:3,

$$x = 251.6y^6 - 893.61y^5 + 1228.2y^4 - 899.58y^3 + 415.86y^2 - 170.73y + 108.51, \quad (8)$$

For pure I/S,

$$x = 357.57y^6 - 1264.4y^5 + 1776.5y^4 - 1325.1y^3 + 591.95y^2 - 204.27y + 107.93, \quad (9)$$

3.3.7 Calculating illite percentage in I/S mixed layer and defining illite crystallinity

Underwood and Guo (2013) used a complementary way to calculate the proportion of illite in the I/S mixed-layer phase is based on the position of the (002/003) peak 16 to 17° 2θ (Moore and Reynolds, 1989) after correcting the diffractogram peaks for misalignment of the detector and sample holder (Table 4). I determined the ° 2θ value of illite/smectite mixed-layer for each sample then interpolated it in Table 4 to calculate illite percentage.

Table 4. The positions of useful reflections for estimating percent illite in illite/smectite (modified after Moore and Reynolds, 1989).

	002/003	
% Illite	**d(Å)**	**° 2θ**
10	5.61	15.80
20	5.58	15.88
30	5.53	16.03
40	5.50	16.11
50	5.44	16.29
60	5.34	16.60
70	5.28	16.79
80	5.20	17.05
90	5.10	17.39

Illite crystallinity index is experimentally determined by measuring the full width at half maximum for the X-ray diffraction reflection of illite (001) peak (Kübler, 2000),

3.4 ESEM grain fabric analyses

3.4.1 Imaging of grain fabric

Yue *et al.* (2012) provided a thorough description of the procedures to image and characterize microfabric. To summarize, a razor blade is used to cut oriented specimens while trimming cylinders for the flow-through tests wet, uncoated, and unfixed surfaces are imaged using an FEI Quanta 600 FEG scanning electron microscope (SEM), which operates in environmental mode (ESEM) at 20 kV with the specimen chamber pressure set at 400 Pa. Water vapor (~98% humidity) from a built-in reservoir keeps specimens from losing moisture with the cooling stage set to 2 ℃. I used a gaseous backscattered electron detector, spot = 3.0, and a working distance of ~10 mm. This combination generates an imaging resolution of ~4 nm, and dimensions of the field of view are with 1000× magnification. All the image files were saved with color grey mode in tiff format.

The gray mode TIFF images from ESEM are processed using "ImageJ" software (rsbweb.nih.gov/ij/index.html), which isolates the apparent dimensions of objects in a two-dimensional image. Processing steps are described as flowing:

(1) Contrast enhancement, by linear stretching of the grey level histogram in order to use 256 grey level values (Figure 21A);

(2) Median filter, by moving each pixel value to the median values of 9 closest pixels (to reduce noise);

(3) Mean filter, by replacing each pixel with the neighborhood mean. The size of the neighborhood is specified by entering its radius in the dialog box (to preserve subtle details);

(4) Median hybrid filter, by moving each pixel to the median values of the middle horizontal 3 pixels, center vertical 3 pixels and center pixel of those 9 closest pixels (to reduce noise while preserving linear features);

(5) Threshold, by adjusting and picking up one point of grey level histogram (to select objects);

(6) Make binary, to transform the grey image to white and black image (Figure 21B);

(7) Overlap the image onto the original image and set its alpha value (transparency) to 60% in Adobe Photoshop 6 software, then separate objects that touch, by manual adjustment with eraser tool (Figure 21C);

(8) Median filter with ImageJ, to remove objects less than 9 pixels in size (because measurements on small objects are mostly biased);

(9) Fill the holes on the objects (Figure 21D);

(10) Measure automatically, to obtain the long-axis and short-axis dimensions and long-axis orientation of an object. The software can automatically determine the long or short axis (apparent dimensions) of the objects in the 2-D image. The results are saved in a text file automatically after the measurement.

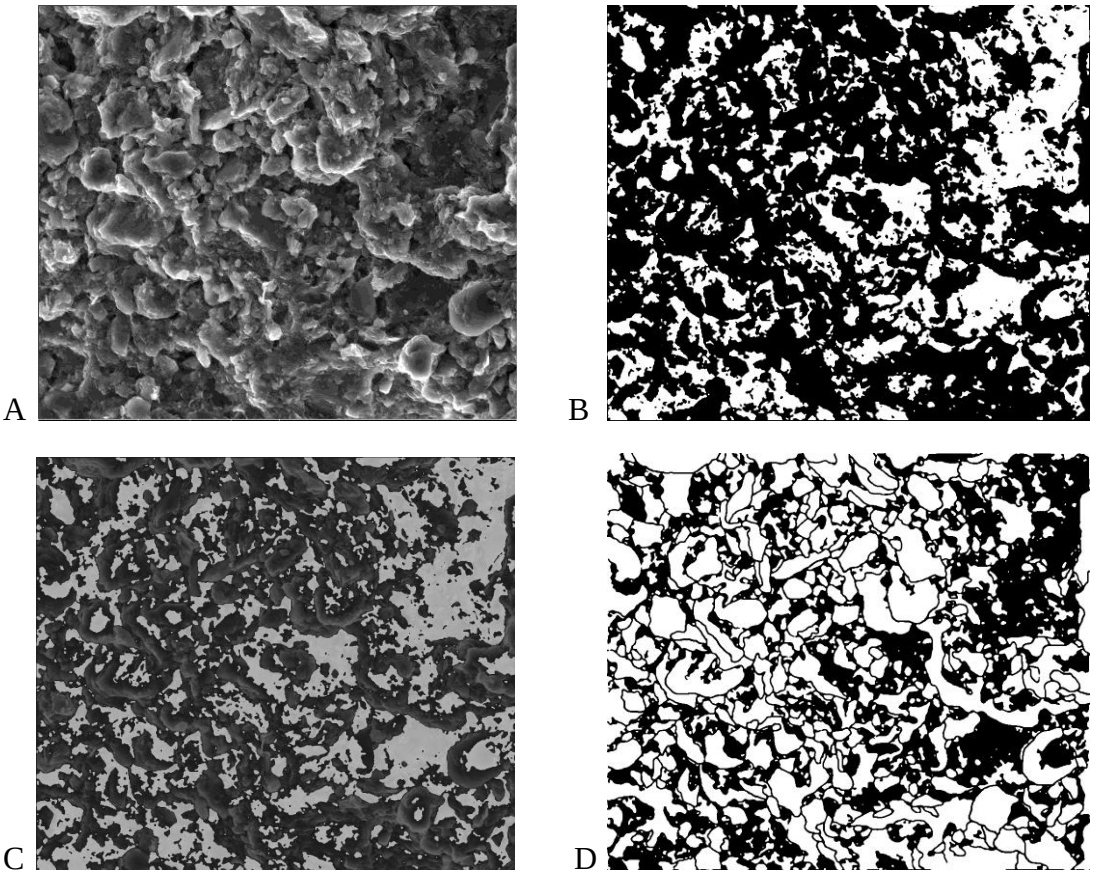

Figure 21. Illustrations of steps used during image analysis of microfabric (348-C0002P-4R-2, 98 cm). (A) ESEM image, (B) Binary image obtained with ImageJ software, (C) Binary image (transparency = 60%) overlying the original ESEM image, (D) Binary image after particle separation using the eraser tool in Photoshop 6 software.

3.4.2 Characterization of microfabric anisotropy

I counted between 600 and 800 grains per image (depending on particle size) to calculate statistics for preferred grain orientation. Each particle orientation (azimuth of the apparent long axis) is assigned to an angle between 0 °and 180 °. For the vertical cut surface, the core axis is oriented at 90°. Rose diagrams were constructed using "Rozeta" software (www.softpedia.com/get/Science-CAD/Rozeta.shtml), which automatically assigns azimuths to bins at 10 °intervals. Cumulative frequency curves are then used to obtain graphical solutions of standard deviation (*d*) according to Folk and Ward (1957) statistics:

$$d = [(\varphi_{84} - \varphi_{16})/4] + [(\varphi_{95} - \varphi_{5})/6.6], \quad (10)$$

where φ_{84}, φ_{16}, φ_{95}, and φ_{5} represent the azimuth (in degrees) at the 84^{th}, 16^{th}, 95^{th}, and 5^{th} percentiles. This graphical technique can avoid the complex calculations required by moment statistics (Chiou *et al.*, 1991). In this context, the largest possible value of *d* is 72.3° (i.e., a case in which φ_{16} and $\varphi_{5} = 0°$ and φ_{84} and $\varphi_{95} = 180$ °). To compare each standard deviation to this maximum *d* value we calculate the "index of microfabric orientation":

$$i = 1 - (d/72.3) \quad (11)$$

If the value of *i* is close to 1, it means the particles tend to align in a preferred direction. With random arrangements of particles, the cumulative curve is relatively flat (slope <0.75) near the median, the value of *d* is >35 °, and the value of *i* is <0.5. As particles attain better parallel alignment, azimuths cluster more tightly, the slope of the

cumulative curve steepens (slope >1.00) near the median, the value of *d* is <25 °, and *i* is >0.65 (Yue *et al.*, 2012).

3.4.3 Energy dispersive X-ray spectroscopy

Energy dispersive X-ray spectroscopy (EDS) is an analytical technique used to identify what particular elements are in a specimen and what their relative proportions are. This technique relies on an interaction of some source of X-ray excitation and a sample. Its characterization capabilities are due in large part to the fundamental principle that each element has a unique atomic structure allowing a unique set of peaks on its X-ray emission spectrum (Goldstein *et al.*, 2003). One example is shown in Figure 22, and sample is from C0002P-4R-02, 98 cm, which shows typical silicate minerals at point 1. Points 2 and 3 in image A consist of similar mineral compositions as point 1, so only one spectrum is shown here.

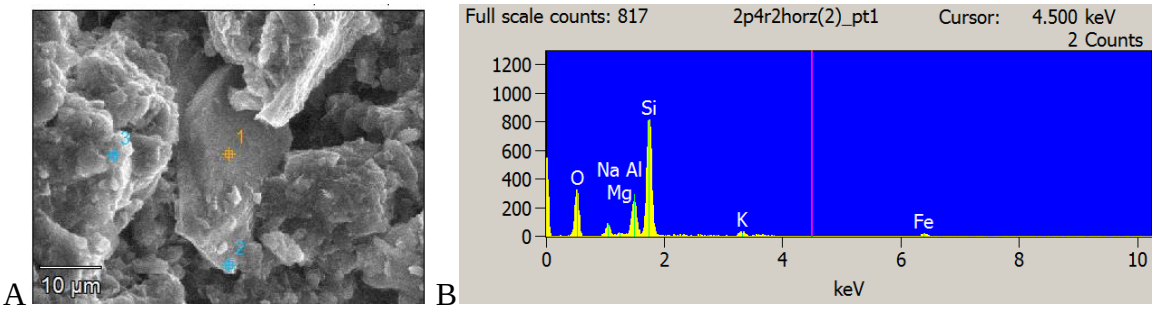

Figure 22. A: SEM image for sample cut from C0002P-4R-02, 98 cm for EDS analysis. B: EDS spectrum on point 1 from image A.

Chapter 4 Results

4.1 Results of constant-flow permeability tests

4.1.1 Characterization of specimens

The main lithology for the WR core samples was characterized by shipboard scientist as silty claystone to clayey siltstone. One sample (C0002P-4R-2, 98 cm) in this study contains one thin layer of silt turbidite. SEM and EDS analyses were used to help characterize the grain sizes and other features found in the specimens (e.g., pyrite). Some additional images are included in the Appendix (Figures A1 to A6).

Figure 23 shows different grain sizes observed in a specimen that was cut with random orientation from 348-C0002P-3R-1, 51 cm. Part of the specimen consists of coarse grains (~50-100 μm), and fine grains (~20-40 μm) are observed for the other part. Photo of the specimen also shows different colors for different layers, and the layer with greenish color is coarser (Figure 23A). Based on the grain size, the coarser layer is more likely clayey siltstone.

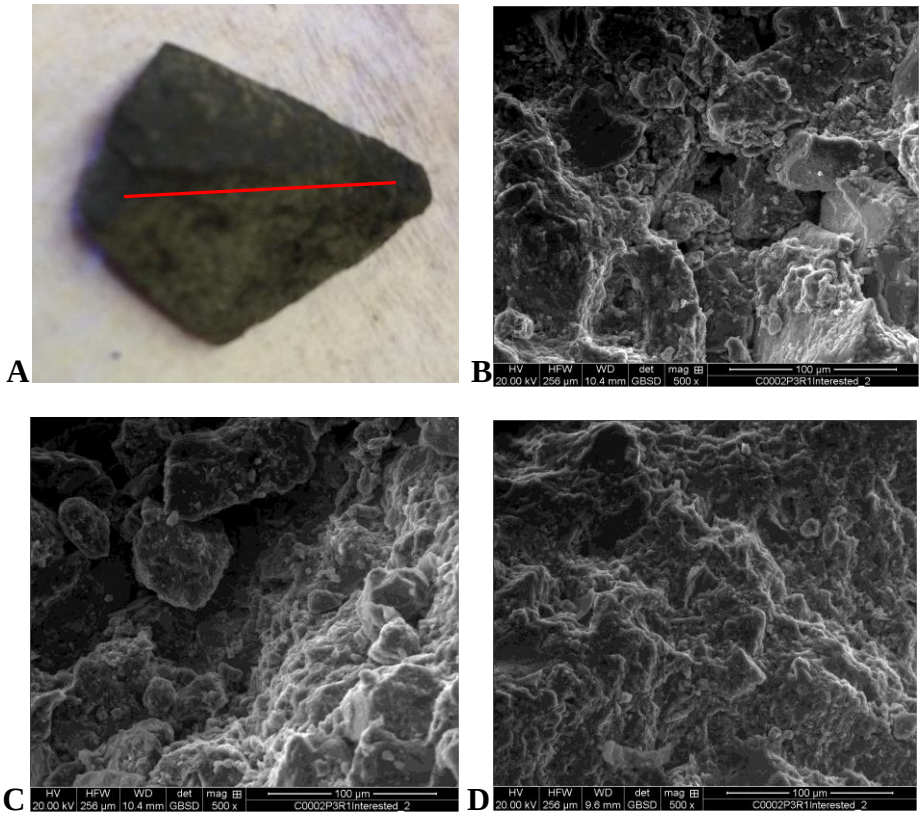

Figure 23. SEM images showing different grain sizes in specimen cut from 348-C0002P-3R-1, 51 cm. A: photo of the specimen imaged by SEM. Red line separates different layers. B: image of coarse grains. C: image of the contrast between coarse grains (upper left) and fine grains (bottom left). D: image of fine grains.

Figure 24 shows pyrite (FeS) framboids identified from a specimen that was cut from 348-C0002P-3R-1, 51 cm. The particles are ~ 1 µm and basically spheroidal aggregate. Pyrite is a common minerals in deep-sea sediments. Schallreuter (1984) reported that pyrite framboids were the most common form of the mineral in the sediments investigated on DSDP Leg 75, and pyrite framboids have been reported since the first DSDP leg (Beall and Fischer, 1969). This form of pyrite is especially common in sapropels (Love and Amstutz, 1966). Moreover, the high contents of S and Fe match the black band identified from the CT scan of the WR sample. Small amount of pyrite is also found in specimen cut from 348-C0002P-4R-2, 98 cm.

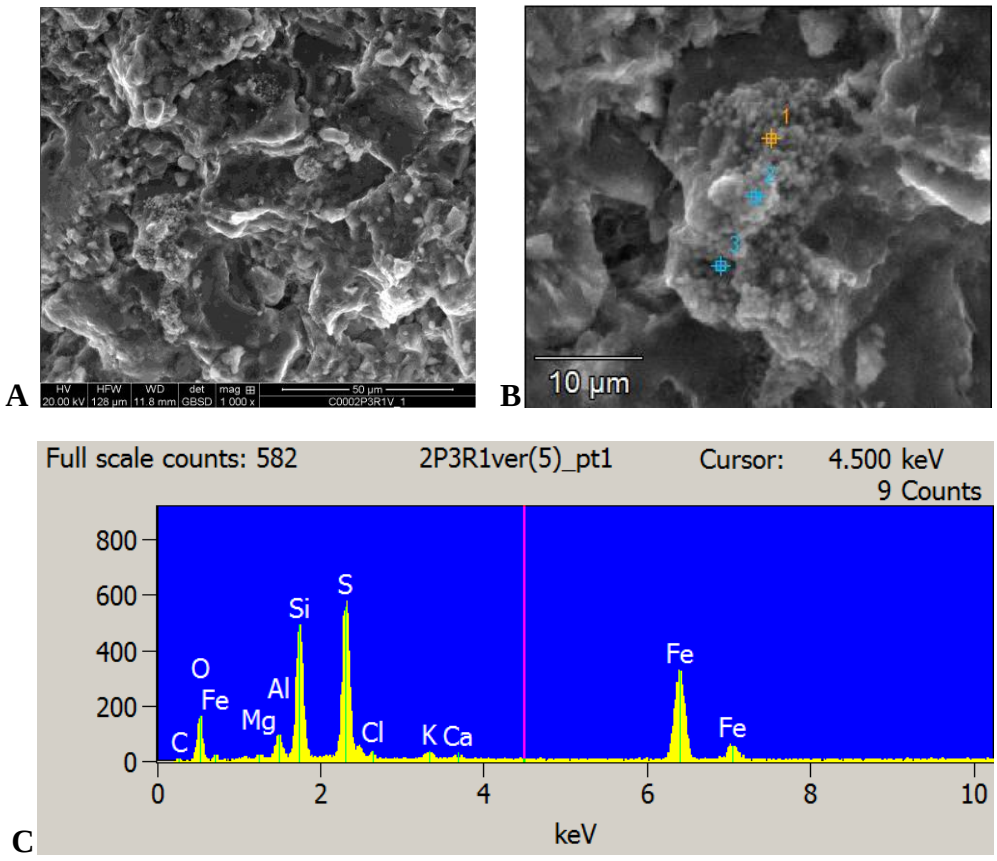

Figure 24. Possible pyrite framboid inside the specimen cut from 348-C0002P-3R-1, 51 cm. A: SEM image of the possible pyrite framboid. B: Image used for EDS analysis on pyrite framboid. C: EDS spectrum results on point 1 from image B. Points 2 and 3 show the similar results as point 1 so their EDS spectrum results are not shown here.

Figure 25 shows SEM images from 348-C0002P-4R-2, 98 cm. There is an oblique thin silty turbidite layer in the trimmed sample (shown in Figure 11), and that is where the image of coarse grains (Figure 30B) is from. The size of the fine grain is ~12 µm, which is dominant in the trimmed sample, and the size of the coarse grain is ~25 µm. Figure 26 shows SEM images from 348-C0002P-6R-1, 64 cm. There is no obvious difference with grain size in this specimen. The average size is ~12-15 µm. In general, these two specimens could also be characterized as clayey siltstone, and specimen 348-

C0002P-4R-2, 98 cm contains relatively more fine grains compared with the other two specimens.

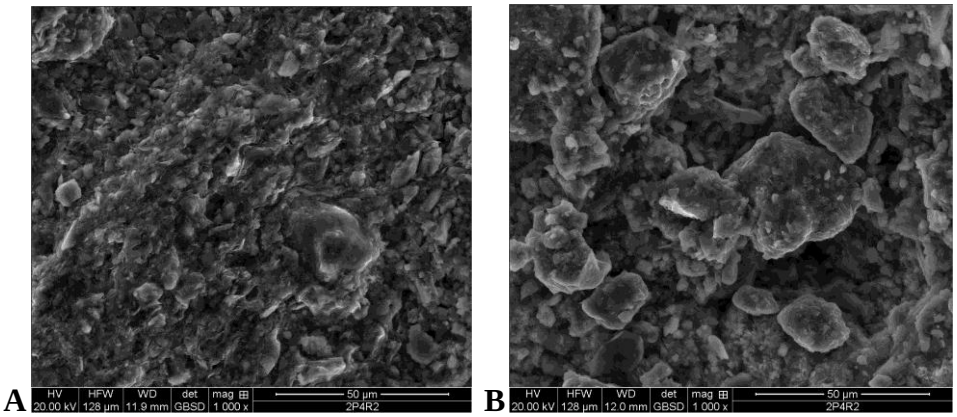

Figure 25. SEM images of different grain sizes in specimen cut from 348-C0002P-4R-2, 98 cm. A: image of fine grains. B: image of coarse grains.

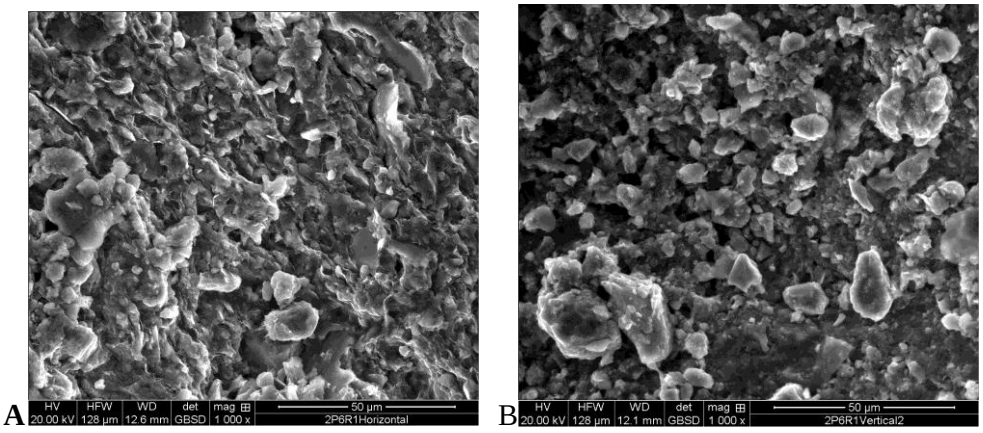

Figure 26. A and B: SEM images of grain sizes in specimen cut from 348-C0002P-6R-1, 64 cm.

4.1.2 Results

Table 5 summarizes lithologic units, values of depth, shipboard grain density and porosity, water content and porosity for trimmings measured before and after each flow–through test.

Table 5. Summary of specimen properties.

Core-section, interval (cm)	Litho - strat. Unit	Depth of top (mbsf)	Cylinder orientation	Shipboard data		Before test		After test	
				Grain density (g/cc)	Porosity (%)	Water content (%)	Porosity (%)	Water content (%)	Porosity (%)
348-C0002P-									
2R-02, 107-114	V	2174.985	Trim failed	2.745	18.88	-	-	-	-
3R-01, 51-72	V	2182.510	Vertical	2.743	19.56	11.5	24	9.1	20
4R-02, 98-103	V	2193.585	Vertical	2.715	20.79	5.1	12	8.8	19
6R-01, 64-76.5	V	2209.640	Vertical	2.741	27.66	10.5	22	9.7	21

For two specimens (348-C0002P-4R-02 and 348-C0002P-6R-01), pre-test water content decreases relative to shipboard values. That was probably caused by the moisture lost during the shipment and storage of the WR specimens. Another reason was that trimmings dried out quickly during the sample preparation. For specimen 348-C0002P-3R-01, 57 cm, the shipboard porosity is lower than either pre-test or post-test porosity. This could result from moisture gained during the trimming procedure in the lab. The spray bottle was used to keep sample saturated during trimming, so this could cause the trimmings content more water than its original water content. For specimen 348-C0002P-4R-02, there is a difference between pre-test porosity and the shipboard porosity, and pre-test porosity is also lower than post-test porosity. That specimen was hard to cut, so there might be moisture lost during the cutting prior the test. The higher post-test porosity could be caused by expansion of water-filled microcracks after the test. Moreover, the

trimmings were not representative of the entire cylinder especially when there are other textures (e.g., black bands) and coarser silty turbidite layer in the whole cylinder.

Each individual test result is illustrated in the Appendix (Figures A7 to A11). Most of the test results are reliable because the coefficients of determination (R^2) are greater than 0.9835. One (348-C0002P-6R-1, 64 cm 0.28 MPa) is less reliable, for which R^2 = 0.9791. This is probably caused by the microcracks inside of the specimen because cracks appeared during trimming for the first stage test (0.28 MPa), and the test kept acting erratically under the higher effective stress (0.55 MPa). While trying to re-trim the specimen for the second stage test, it fell into pieces along those crack lines, so the test result should be interpreted with caution. The goal was to test specimens with different layers and textures; however, because of the limited material extracted from the core liner, the results here may not represent the entire WR samples because the WR samples are not homogeneous. Table 6 lists effective stress level, bedding dips, average height and diameter, Skempton's *B*-value, average values of hydraulic conductivity, and intrinsic permeability for each specimen.

Table 6. Sample properties and average test results.

Core, section, interval (cm)	Depth of top (mbsf)	Effective stress (Mpa)	Beds dip (°)	Ave. height (cm)	Ave. diameter (cm)	Skempton's *B*-value	Vertical hydraulic conductivity (cm/s)	Vertical intrinsic permeability (m^2)
348-C0002P-								
3R-01, 51	2182.51	0.28	88	7.80	3.80	0.82	2.13E-08	2.12E-17
		0.55					1.28E-08	1.27E-17
4R-02, 98	2193.585	0.28	89	3.65	4.15	0.84	4.33E-09	4.30E-18
		0.55					3.83E-09	3.80E-18
6R-01, 64	2209.64	0.28	84	4.40	4.50	0.77	2.68E-08	2.66E-17

At Hole C0002P, the highest value of vertical hydraulic conductivity (K) is 2.68 × 10^{-8} cm/s, with intrinsic permeability (k) of 2.66 × 10^{-17} m^2 (348-C0002P-6R-01, 64 cm 0.28 MPa). The lowest value of K is 3.83 × 10^{-09} cm/s, with k = 3.80 × 10^{-18} m^2 (348-C0002P-4R-02, 98 cm 0.55MPa). Table A1 lists values of volumetric flow rate, discharge velocity, steady-state head loss, steady-state hydraulic gradient, hydraulic conductivity, and intrinsic permeability for each test. Figure 27 shows intrinsic permeability values changing with depth. The permeability values are slightly higher at a confining stress of 0.55 MPa than at 0.28 MPa.

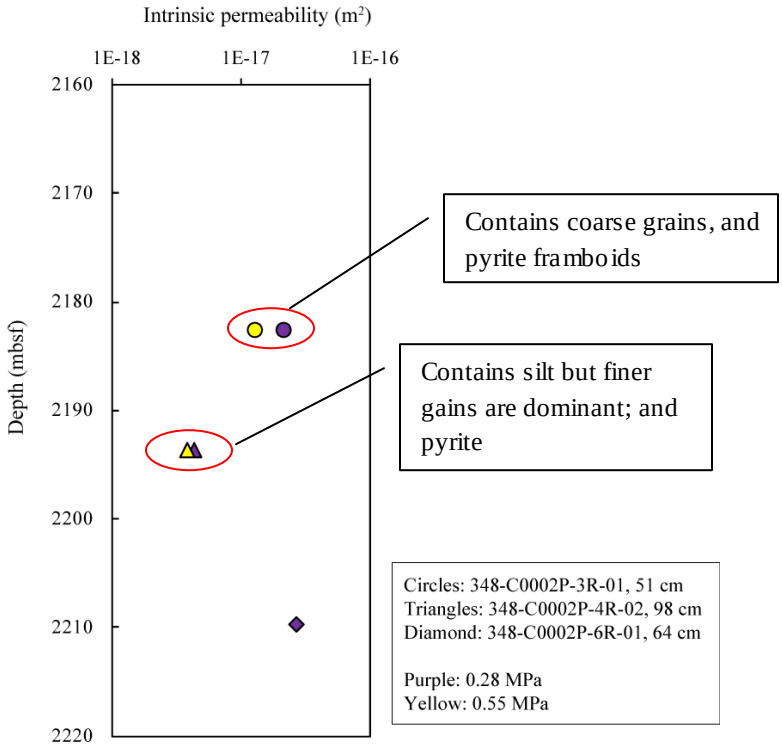

Figure 27. Plot of intrinsic permeability at different effective stress level changing with depth for each specimen from Hole C0002P.

4.2 Results of XRD analysis for cuttings and cores

4.2.1 Shipboard bulk powder

Shipboard bulk powder XRD results show the relative abundance of total clay minerals, quartz, feldspar, and calcite. Only results for cuttings from the 1-4 mm size fraction are reported here. Figure 28 includes data from cuttings from Hole C0002F (Expedition 338 Scientists, 2014b) and Holes C0002N and C0002P (Expedition 348 Scientists, 2015b).

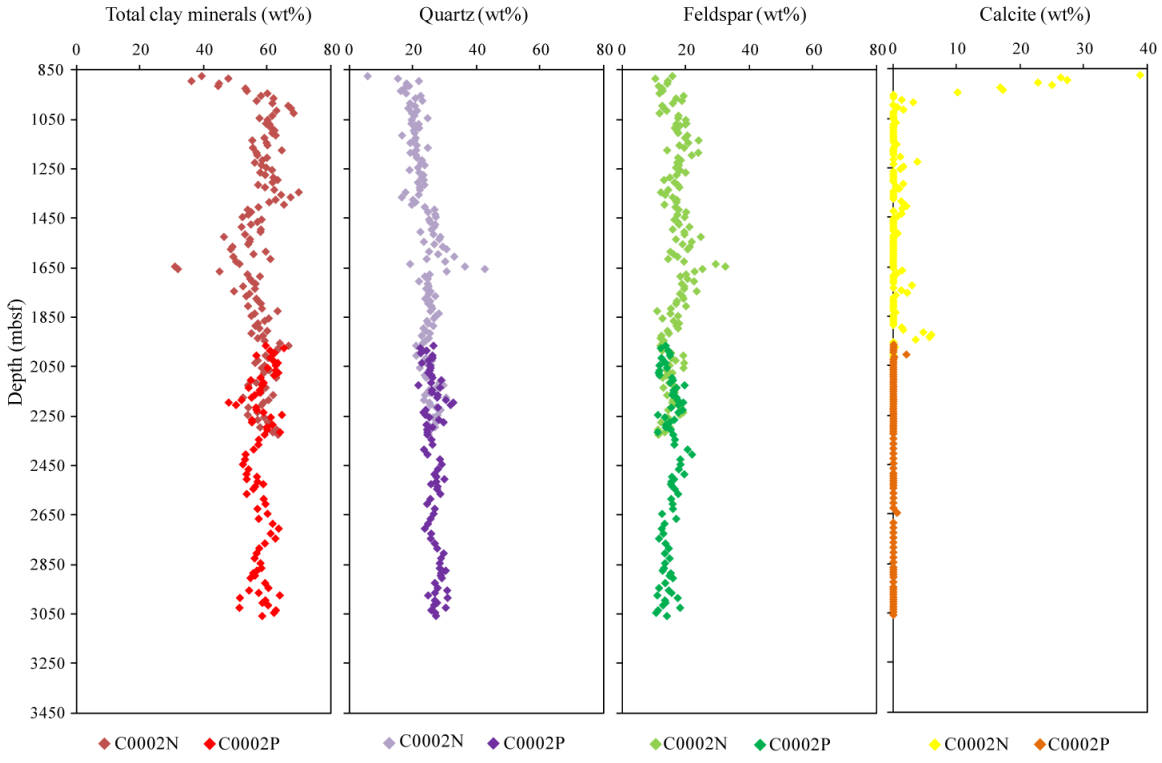

Figure 28. Relative abundances of total clay, quartz, feldspar, and calcite for shipboard bulk powder samples from Holes C0002F, C0002N and C0002P.

In Hole C0002F, cuttings analysis were measured from 920.5 mbsf to 2000.5 mbsf. There are a few cycles of increasing then decreasing in total clay content while

quartz and feldspar remain relatively constant with slight changing through this interval. Calcite, however, shows a large decrease from ~28 to 5 wt% from 920 to 1025.5 mbsf, then remains relatively constant and low values after that. This abrupt change is probably because of cement contamination, which is mining of chips of cement pumped to secure casing, then drilled out.

In Hole C0002N, cuttings were measured between 875.5 and 2325.5 mbsf. Judging from the relative weight percentage of calcite, the uppermost few measurements still show contamination with cement. A cyclic pattern of increasing and decreasing values for total clay, quartz and feldspar repeatedly occur in this interval, but for calcite, after a large decrease from ~39 to 0.1 wt% between 875.5 and 1025.5 mbsf, it basically remains at 0.1 wt% (Expedition 348 Scientists, 2015b). The data from Hole C0002N correlates well with those from Hole C0002F.

In Hole C0002P, the interval for sampling cuttings overlapped with Hole C0002N from 1965.5 mbsf to the depth of 2325.5 mbsf, and contents of total clay minerals, quartz, feldspar and calcite correlate well between C0002P and C0002N in overlap interval. From 2315.5 mbsf to 2435.5 mbsf, total clay minerals decreases from 64% to 51%, whereas quartz and feldspar both increase from 24.7% to 32% and 11.3% to 16.9%. From 2445.5 mbsf to 2705.5 mbsf, total clay mineral content increases from 52.4% to 63.6%, and quartz and feldspar remain approximately the same. From 2705.5 mbsf and 2945.5 mbsf, total clay decreases first from 63.6% to 56% then starts to increase from 56% to 60.4%, while an opposite trend for quartz and feldspar occurs in this interval but without significant variations. Quartz increases from 23.8% to 29.7% then decreases to 27%.

Feldspar increases from 12.5% to 15% then decreases to 11.7%. Calcite remains low as ~0.1 wt% over the whole depth range.

4.2.2 Shipboard core samples

The main lithologies in the cored interval of Hole C0002P are greenish gray silty claystone and fine-grained sandstone (Expedition 348, 2015b). Core samples show trends similar to the cuttings from Holes C0002N and C0002P (Figure 29). Total clay minerals shows the greatest amount of variation through the core, ranging from ~58 wt% to 62 wt%, while there are no significant variations for quartz, feldspar and calcite. Interestingly, the total clay mineral content in the cuttings from Hole C0002P is slightly lower by ~4% than that in core samples from Hole C0002P and cuttings from Hole C0002N, while quartz is slightly higher by ~2-3% in the cuttings from Hole C0002P. One possible reason could be the change in the drill mud composition (Expedition 348 Scientists, 2015b).

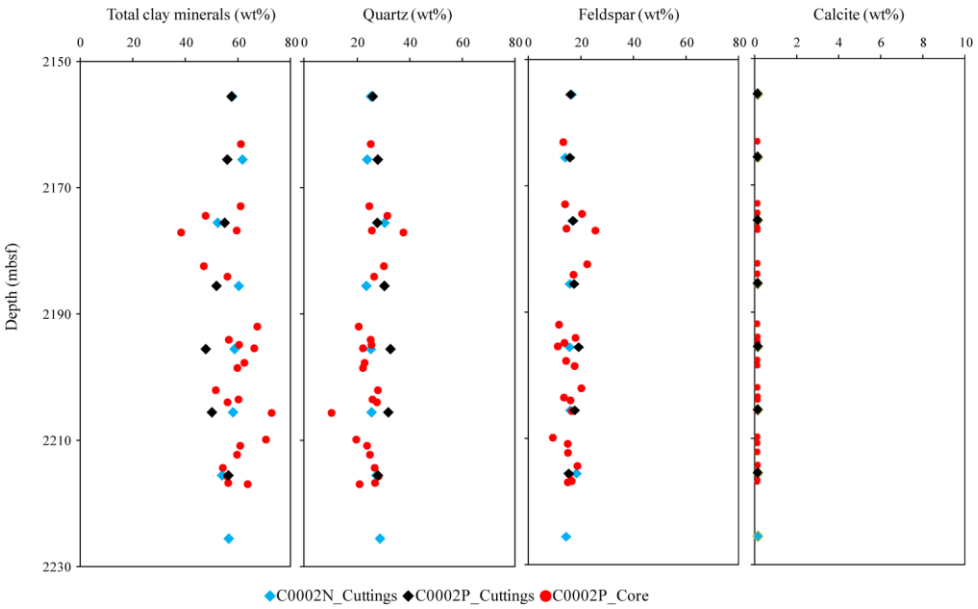

Figure 29. Relative abundance of total clay minerals, quartz, feldspar, and calcite for shipboard core and cuttings from Holes C0002N and C0002P.

4.2.3 Cuttings samples from Hole C0002F

Cutting samples were collected from Hole C0002F within the depth interval of 1190.5 to 1990.5 mbsf in lithologic units IV and V, which consist of greenish gray silty claystone and fine-grained sandstone. The age of these strata is < 5.59 Ma (Expedition 338 Scientists, 2014b). The XRD results for the clay-size fraction show the relative abundance of smectite, illite, kaolinite/chlorite, and quartz (Figure 30 and Table 7). Smectite is the most abundant clay-size mineral with 39.2 wt% average, followed by illite (37.4 wt% average), chlorite (19.9 wt% average), kaolinite (3.0 wt% average), and quartz (0.6 wt% average).

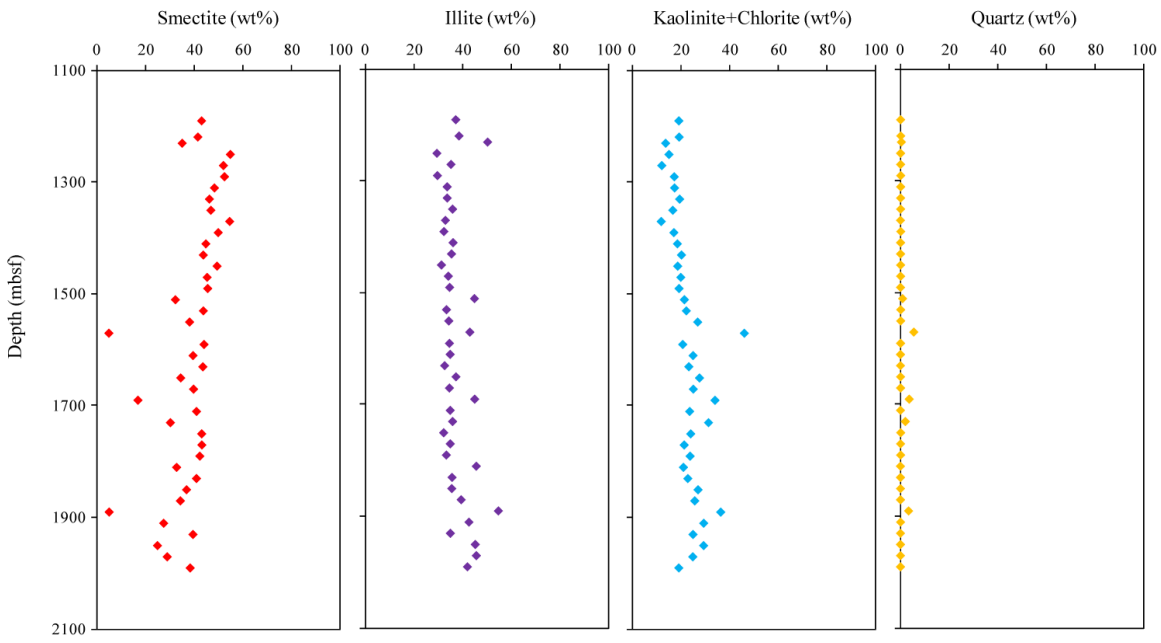

Figure 30. Relative abundances of smectite, illite, kaolinite/chlorite, and quartz in clay-size fraction of cutting samples from Hole C0002F.

The abundance of smectite in the bulk sediment (Figure 31 and Table 7) was calculated by multiplying the percentage of smectite within each clay mineral assemblage (where smectite + illite + chlorite + kaolinite = 100%) by the percentage of total clay

minerals in the same shipboard bulk sediment (where total clay minerals + quartz + feldspar + calcite = 100%) (Underwood and Guo, 2013; Expedition 338 Scientists, 2014b). Placing the clay mineral data in the context of bulk mineralogy is beneficial if the goal is to evaluate whether smectite affects the mechanical and hydrologic properties of the Nankai accretionary prism.

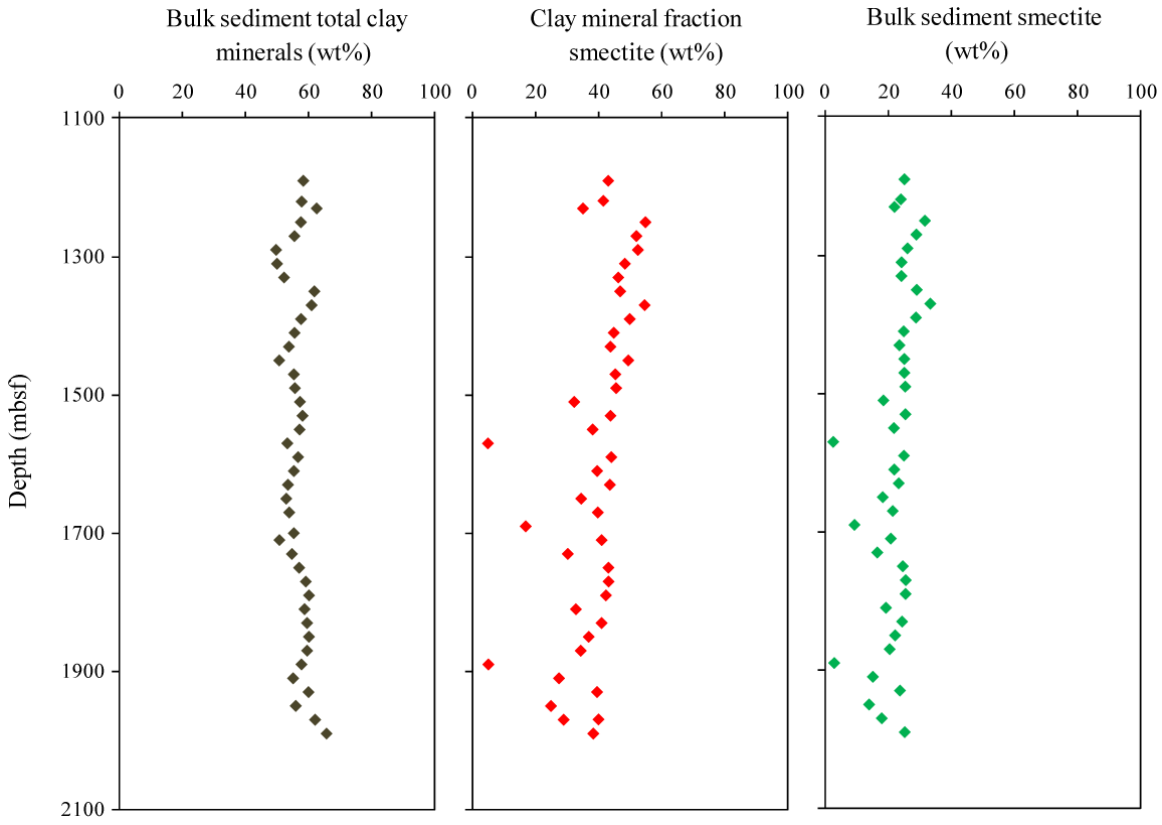

Figure 31. Relative abundances of total clay minerals in bulk sediment relative to quartz + feldspar + calcite (Expedition 338 Scientists, 2014b), smectite in the clay mineral fraction (relative to illite + chlorite + kaolinite), and smectite in bulk sediment. Samples are all from Hole C0002F.

Table 7. Results of XRD analysis with values of integrated peak area and calculated relative clay mineral abundance for cuttings from Hole C0002F.

Core, section, interval (cm)	Depth (mbsf)	Integrated peak area (total counts)						Relative mineral abundance within clay-size fraction SVD normalization factors (wt%)						Relative abundance within bulk sediment (wt%)		
		Smectite (001)	Illite (001)	Kaolinite (001) + Chlorite (002)	Quartz (100)	Kaolinite (002) + Chlorite (004)	Half peak chlorite (004)	Smectite	Illite	Kaolinite + Chlorite	Quartz	Kaolinite	Chlorite	Total clay minerals	Smectite	Illite
348-C0002F-																
82	1190.5	26424	4669	3978	126	2778	1328	43.2	37.3	19.3	0.2	1.2	18.1	58.5	25.3	21.8
86	1219.5	21392	4066	3336	116	2593	1170	41.7	38.6	19.4	0.3	2.7	16.8	58.0	24.2	22.4
92	1230.5	8400	2505	1116	55	1288	881	35.2	50.4	13.8	0.5	0.0	13.8	62.8	22.1	31.6
96	1250.5	32558	3696	3372	167	2588	1292	55.0	29.5	15.2	0.2	0.0	15.2	57.7	31.8	17.0
100	1270.5	32249	4574	2936	126	1895	969	52.2	35.3	12.3	0.2	0.0	12.3	55.7	29.1	19.7
104	1290.5	27847	3325	3306	178	2335	1176	52.6	29.8	17.4	0.2	0.0	17.4	49.9	26.3	14.9
108	1310.5	31030	4522	3948	199	3007	1352	48.5	33.7	17.5	0.2	2.5	15.1	50.2	24.4	16.9
112	1330.5	29404	4388	4236	111	3276	1451	46.4	33.8	19.6	0.2	3.1	16.5	52.4	24.3	17.7
116	1350.5	29158	4662	3662	182	2615	1163	47.0	36.0	16.8	0.2	2.6	14.2	62.0	29.2	22.3
122	1370.5	43842	5547	3830	125	2341	1016	54.8	33.0	12.0	0.2	2.2	9.8	61.1	33.5	20.2
126	1390.5	24769	3354	3035	128	2420	1159	50.0	32.4	17.2	0.3	1.0	16.2	57.8	28.9	18.8
132	1410.5	32564	5447	4640	210	3580	1443	45.0	36.2	18.7	0.2	5.0	13.7	55.7	25.0	20.2
136	1430.5	33448	5642	5242	256	3650	1941	43.9	35.5	20.4	0.2	0.0	20.4	53.9	23.7	19.2
140	1450.5	30385	3987	4027	120	2628	1147	49.6	31.4	18.8	0.2	3.3	15.5	50.9	25.2	16.0
144	1470.5	28486	4489	4287	225	2625	1165	45.5	34.2	20.1	0.2	3.2	16.9	55.5	25.2	19.0
150	1490.5	33565	5283	4854	193	3971	1895	45.7	34.7	19.3	0.2	1.3	18.1	55.9	25.5	19.4
155	1510.5	21361	6122	4548	196	2776	1228	32.4	45.0	21.6	1.0	3.5	18.1	57.4	18.6	25.8
161	1530.5	24835	3923	4212	186	3131	1668	43.9	33.5	22.4	0.2	0.0	22.4	58.3	25.6	19.5
167	1550.5	20722	3741	4596	120	3404	1927	38.3	34.4	27.0	0.3	0.0	27.0	57.3	21.9	19.7
172	1570.5	2980	3337	5206	97	4518	1962	5.1	43.1	46.2	5.6	8.5	37.8	53.5	2.7	23.0
177	1590.5	31102	4989	4917	139	4126	1713	44.2	34.7	20.9	0.2	4.9	16.0	56.8	25.1	19.7
184	1610.5	34264	6039	6879	138	5168	2853	39.7	35.0	25.1	0.2	0.0	25.1	55.5	22.0	19.4
189	1630.5	40236	6066	7011	114	4785	2149	43.7	32.7	23.4	0.2	3.3	20.1	53.6	23.5	17.5
195	1650.5	25257	5316	6153	96	4537	2443	34.6	37.4	27.8	0.2	0.0	27.8	53.1	18.4	19.9
201	1670.5	29727	5171	5965	121	3919	1444	39.9	34.7	25.2	0.2	8.9	16.3	54.0	21.6	18.7
205	1690.5	6327	3193	3577	96	2749	1410	17.0	45.1	34.2	3.7	0.0	34.2	55.5	9.5	25.0
209	1710.5	36947	6335	6865	155	5017	2095	41.1	35.0	23.7	0.2	5.4	18.3	51.0	21.0	17.8
213	1730.5	10640	2532	3371	118	2944	1116	30.4	36.0	31.5	2.1	10.3	21.2	54.9	16.7	19.8
217	1750.5	25195	3829	4586	126	3048	1675	43.3	32.3	24.2	0.2	0.0	24.2	57.2	24.8	18.5
223	1770.5	30331	4954	4963	96	3161	1301	43.3	35.0	21.5	0.2	5.2	16.2	59.3	25.7	20.8
229	1790.5	29102	4615	5295	108	3107	1205	42.5	33.4	23.9	0.2	7.3	16.6	60.3	25.6	20.2
233	1810.5	35576	9648	7113	89	4948	1968	33.0	45.7	21.2	0.1	5.9	15.2	58.9	19.4	26.9
238	1830.5	34256	5943	6164	82	4229	2209	41.1	35.8	23.0	0.2	0.0	23.0	59.7	24.5	21.4
250	1850.5	31783	6159	7322	215	5323	2360	37.0	35.6	27.2	0.2	4.3	22.9	60.3	22.3	21.5
255	1870.5	30565	6861	7022	114	4976	2399	34.5	39.5	25.8	0.2	1.3	24.5	59.7	20.6	23.6
260	1890.5	4403	6264	6037	76	5335	2050	5.2	54.8	36.5	3.5	11.5	25.0	58.0	3.0	31.8
265	1910.5	22623	6675	7039	116	4407	1993	27.6	42.7	29.5	0.2	4.0	25.5	55.3	15.3	23.6
269	1930.5	36045	6383	7246	155	5464	2954	39.7	35.1	25.1	0.2	0.0	25.1	60.2	23.9	21.1
274	1950.5	22607	7738	7643	127	5333	2285	25.1	45.3	29.5	0.2	5.9	23.6	56.1	14.1	25.4
282	1970.5	27965	8532	7220	119	4353	1797	29.1	45.8	25.0	0.1	6.0	19.0	62.3	18.1	28.5
286	1990.5	34013	7448	5572	110	3178	1661	38.5	42.1	19.3	0.2	0.0	19.3	65.9	25.4	27.7

Indicators of clay diagenesis (I/S expandability, illite percentage in I/S mixed layer and illite crystallinity index) are plotted and calculated in Figure 32 and Table 8. The expandability of I/S has an average value of 70%, and the illite percentage in I/S mixed layer is 26%, which indicates smectite illitization has initiated. The range of illite crystallinity index varies from 0.407 to 0.642, which show that detrital source rocks during the late Miocene had been subjected to advanced levels of diagenesis and incipient greenschist-facies metamorphism (Kübler and Jaboyedoff, 2000).

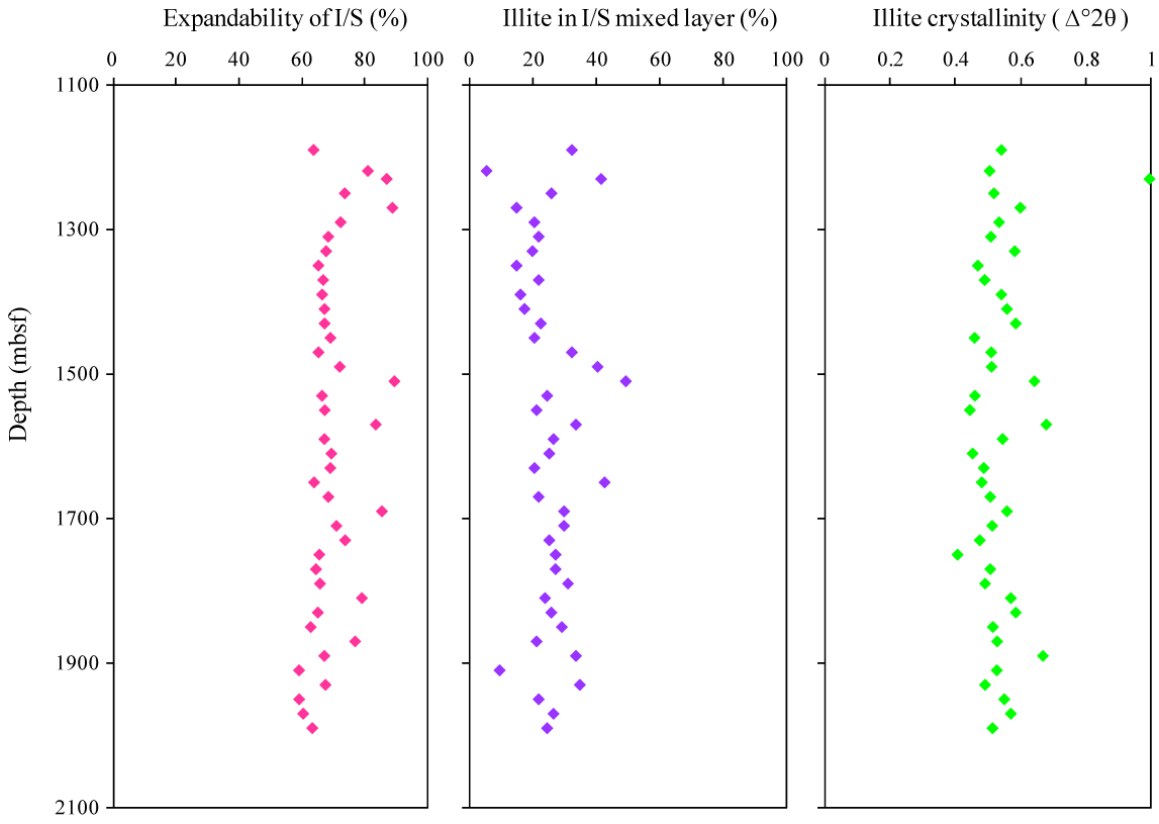

Figure 32. Plots of illite/smectite (I/S) mixed-layer clay expandability, proportion of illite in I/S mixed-layer clay and illite crystalinity index. Samples are collected from Hole C0002F.

Table 8. Results of XRD analysis with values of illite/smectite (I/S) expandability, illite in I/S, and illite crystallinity index, Hole C0002F.

Core, section, interval (cm)	Depth (mbsf)	Intensity saddle (cps)	Intensity peak (cps)	Ratio saddle peak	Expandability (%)	Illite (002) / smectite (003) (°2θ)	Illite in I/S (%)	Illite crystallinity (Δ °2θ)
348-C0002F-								
82	1190.50	213	319	0.668	64	16.05	32	0.541
86	1219.50	56	173	0.324	81	15.67	6	0.505
92	1230.50	14	60	0.233	87	16.14	42	0.994
96	1250.50	132	294	0.449	74	15.97	26	0.518
100	1270.50	50	240	0.208	89	15.84	15	0.599
104	1290.50	125	264	0.473	72	15.89	21	0.534
108	1310.50	190	342	0.556	68	15.91	22	0.509
112	1330.50	212	371	0.571	68	15.88	20	0.582
116	1350.50	235	373	0.630	65	15.84	15	0.469
122	1370.50	303	511	0.593	67	15.91	22	0.490
126	1390.50	182	303	0.601	66	15.85	16	0.541
132	1410.50	232	398	0.583	67	15.86	18	0.558
136	1430.50	243	417	0.583	67	15.92	23	0.585
140	1450.50	200	370	0.541	69	15.89	21	0.459
144	1470.50	221	351	0.630	65	16.05	32	0.510
150	1490.50	159	332	0.479	72	16.12	41	0.511
155	1510.50	32	160	0.200	89	16.28	49	0.642
161	1530.50	189	314	0.602	66	15.95	25	0.460
167	1550.50	160	275	0.582	67	15.90	21	0.445
172	1570.50	12	30	0.400	76	16.06	34	0.678
177	1590.50	208	356	0.584	67	15.98	27	0.545
184	1610.50	188	352	0.534	69	15.96	25	0.453
189	1630.50	252	466	0.541	69	15.89	21	0.487
195	1650.50	215	324	0.664	64	16.16	43	0.481
201	1670.50	200	360	0.556	68	15.91	22	0.507
205	1690.50	13	51	0.255	85	16.03	30	0.558
209	1710.50	180	360	0.500	71	16.03	30	0.513
213	1730.50	50	112	0.446	74	15.96	25	0.475
217	1750.50	197	316	0.623	65	15.99	27	0.407
223	1770.50	237	365	0.649	64	15.99	27	0.507
229	1790.50	220	356	0.618	66	16.04	31	0.491
233	1810.50	90	254	0.354	79	15.94	24	0.570
238	1830.50	252	397	0.635	65	15.97	26	0.585
250	1850.50	285	413	0.690	63	16.02	29	0.515
255	1870.50	16	41	0.390	77	15.90	21	0.528
260	1890.50	269	352	0.764	59	16.06	34	0.668
265	1910.50	272	352	0.773	59	15.79	10	0.527
269	1930.50	247	429	0.576	67	16.07	35	0.491
274	1950.50	281	364	0.772	59	15.91	22	0.550
282	1970.50	295	396	0.745	60	15.98	27	0.570
286	1990.50	280	413	0.678	63	15.95	25	0.514

4.2.4 Cluster samples from Hole C0002P

Cluster samples were collected adjacent to each whole-round sample used for shipboard analyses and shore-based tests by other scientists. The samples used in this study are from 2163 mbsf to 2216.825 mbsf in lithologic unit V, which consists of

greenish gray silty claystone and fine-grained sandstone. These samples are from the same clusters as the shipboard core samples used for XRD test. The age of these strata is younger than ~10.54 Ma (Expedition 348 Scientists, 2015b). The XRD results for the clay-size fraction show the relative abundance of smectite, illite, kaolinite/chlorite, and quartz (Figure 33 and Table 9). The relative abundance of smectite varies the most, from 11.4 wt% to 98.2 wt%, and it is still the most abundant clay-size mineral with 39.5 wt% average, followed by illite (32.5 wt% average), chlorite (22.7 wt% average), quartz (3.0 wt% average) and kaolinite (2.4 wt%).

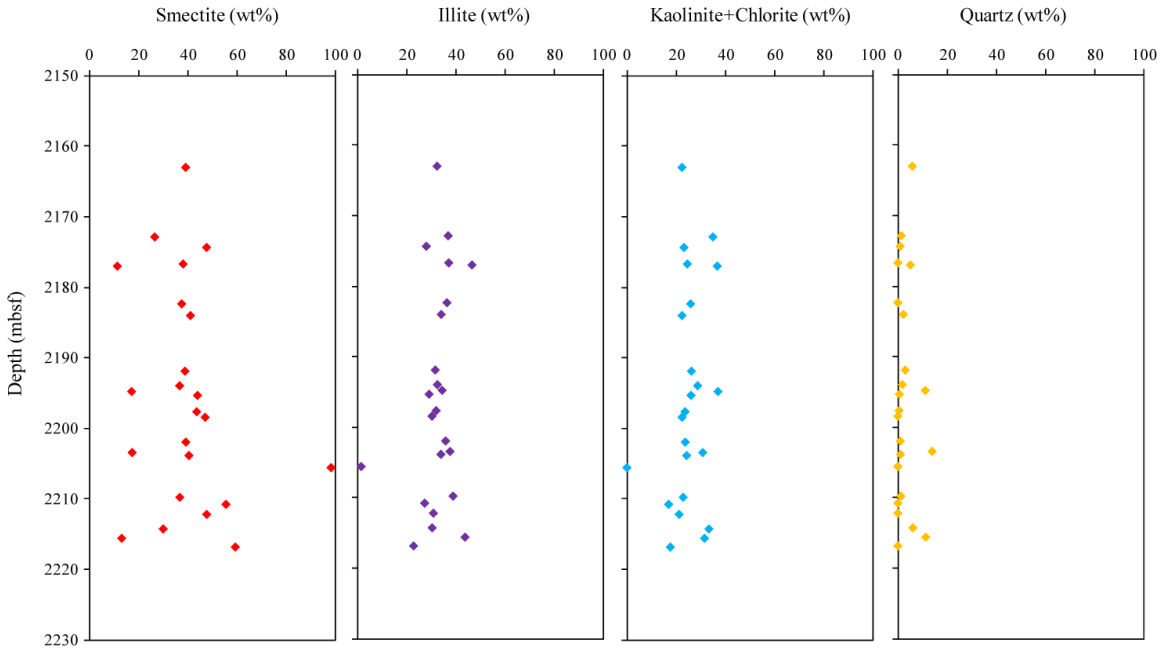

Figure 33. Relative abundances of smectite, illite, kaolinite/chlorite, and quartz in clay-size fraction of cluster samples from Hole C0002P.

For specimen with more than 80% smectite in the clay-size fraction, it is considered to be bentonite (348-C0002P-5R-5, 2 cm). I also calculated the abundance of smectite in the bulk sediment (Figure 34 and Table 9) by multiplying the percentage of smectite within each clay mineral assemblage (where smectite + illite + chlorite +

kaolinite = 100%) by the percentage of total clay minerals in the same shipboard bulk sediment (where total clay minerals + quartz + feldspar + calcite = 100%) (Underwood and Guo, 2013; Expedition 348 Scientists, 2015b).

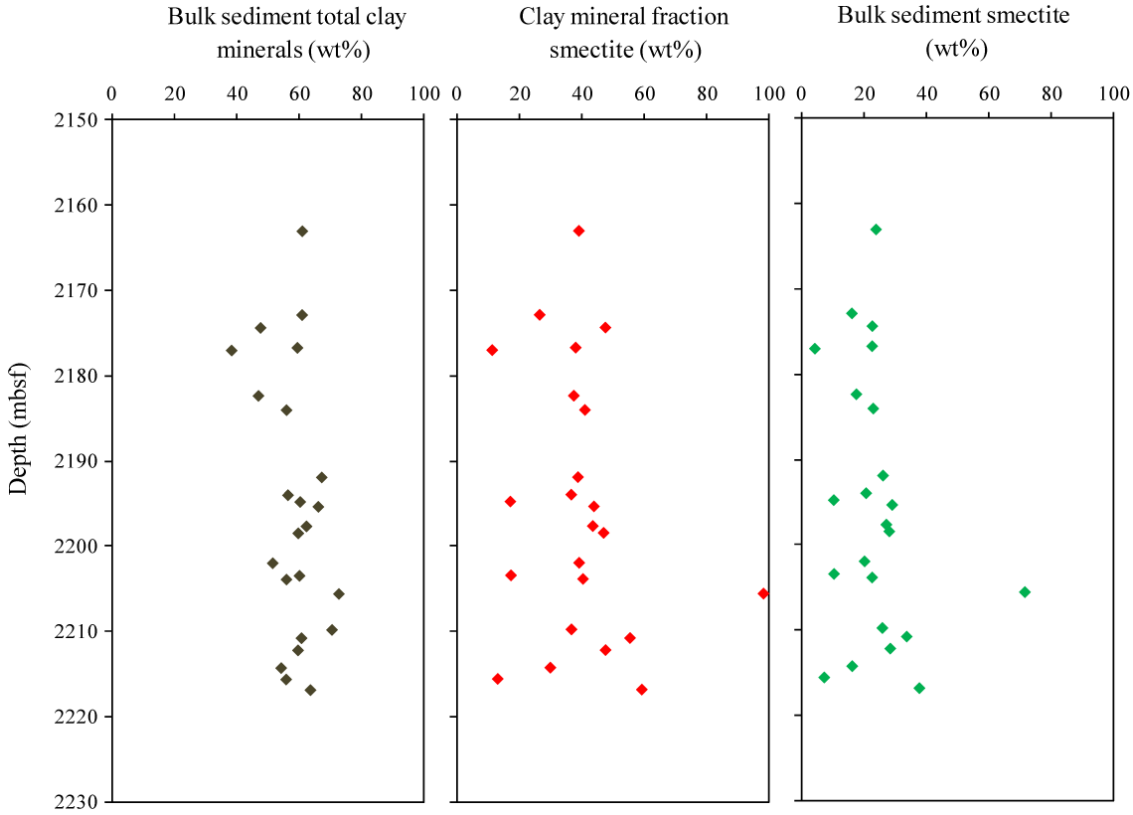

Figure 34. Relative abundances of total clay minerals in bulk sediment relative to quartz + feldspar + calcite (Expedition 348 Scientists, 2015b), smectite in the clay mineral fraction (relative to illite + chlorite + kaolinite), and smectite in bulk sediment. Samples are all from Hole C0002P.

Table 9. Results of XRD analysis with values of integrated peak area and calculated relative clay mineral abundance for clusters from Hole C0002P.

Core, section, interval (cm)	Depth (mbsf)	Integrated peak area (total counts)						Relative mineral abundance within clay-size fraction SVD normalization factors (wt%)						Relative abundance within bulk sediment (wt%)		
		Smectite (001)	Illite (001)	Kaolinite (001) + Chlorite (002)	Quartz (100)	Kaolinite (002) + Chlorite (004)	Half peak chlorite (004)	Smectite	Illite	Kaolinite + Chlorite	Quartz	Kaolinite	Chlorite	Total clay minerals	Smectite	Illite
348-C0002P-																
1R 1 0	2163.00	22516	4061	4370	384	3072	1190	39.2	32.4	22.4	5.9	6.9	15.5	61.2	24.0	19.9
2R 1 35	2172.85	26787	7192	10257	259	7367	3696	26.6	37.0	35.0	1.4	0.0	35.0	61.1	16.3	22.6
2R 2 43	2174.35	33527	4156	5538	337	4235	2601	47.8	28.1	23.2	0.9	0.0	23.2	47.8	22.8	13.4
2R 3 137	2176.70	30294	5928	6196	160	4197	1703	38.1	37.1	24.6	0.2	6.4	18.2	59.6	22.7	22.1
2R 4 27	2177.00	7071	5318	6123	160	3873	2170	11.4	46.7	36.8	5.1	0.0	36.8	38.5	4.4	18.0
3R 1 35	2182.35	31520	6164	6868	200	4746	2054	37.5	36.4	25.9	0.2	4.8	21.0	47.1	17.7	17.2
3R 2 60	2184.01	29477	5168	5367	338	3859	1833	41.2	34.1	22.4	2.2	1.6	20.8	56.1	23.1	19.1
4R 1 39	2191.89	24111	4130	5327	304	3791	1826	39.0	31.7	26.3	3.0	1.4	24.9	67.4	26.3	21.4
4R 2 135	2193.96	24563	4478	6115	267	4432	2080	36.8	32.6	28.8	1.9	2.5	26.3	56.6	20.8	18.4
4R 3 72	2194.77	5913	2768	4418	264	4142	1620	17.3	34.5	37.0	11.2	11.0	26.1	60.5	10.4	20.9
4R 4 32	2195.33	38215	5278	7458	364	5412	2903	44.1	29.2	26.1	0.6	0.0	26.1	66.3	29.2	19.4
4R 5 125	2197.64	38676	5936	6967	362	4983	2892	43.7	32.1	23.7	0.5	0.0	23.7	62.5	27.3	20.1
4R 6 54	2198.43	37668	5081	6068	311	4291	2132	47.1	30.3	22.4	0.2	0.2	22.2	59.9	28.2	18.2
5R 1 95	2201.95	28303	5381	5595	275	3687	1367	39.3	35.9	23.7	1.0	8.3	15.5	51.7	20.3	18.6
5R 2 99	2203.43	3225	1940	2316	206	2417	1066	17.5	37.7	30.9	13.9	5.1	25.8	60.3	10.5	22.7
5R 3 0	2203.85	29114	5091	5735	288	4032	1989	40.5	34.0	24.3	1.1	0.5	23.9	56.1	22.7	19.1
5R 5 2	2205.57	128967	1143	1018	403	560	337	98.2	1.6	0.1	0.1	0.0	0.1	72.9	71.6	1.2
6R 1 77	2209.77	27740	6108	5615	275	3904	2075	36.8	39.0	22.9	1.3	0.0	22.9	70.7	26.1	27.6
6R 2 37	2210.78	48928	5147	5456	411	3778	2090	55.5	27.4	17.0	0.1	0.0	17.0	60.9	33.8	16.7
6R 3 37	2212.19	42322	5749	6426	322	4656	1973	47.7	30.9	21.2	0.1	4.5	16.7	59.8	28.5	18.5
6R 4 103	2214.26	17269	3669	6126	323	4948	2383	30.1	30.4	33.4	6.1	1.7	31.6	54.4	16.4	16.6
6R 5 94	2215.58	4531	4004	4159	277	3698	1897	13.2	43.8	31.6	11.4	0.0	31.6	56	7.4	24.5
6R 6 77	2216.83	52858	4368	5823	311	4273	2018	59.3	22.9	17.7	0.1	1.4	16.3	63.8	37.9	14.6

Indicators of clay diagenesis (I/S expandability, illite percentage in I/S mixed layer and illite crystallinity index) are plotted and calculated in Figure 35 and Table 10. The expandability of I/S does not show significant varibility with coring depth with an average value of 69% (three anomalies were omitted), but there is a slight increase below ~2190 mbsf. The illite percentage in I/S mixed layer varies from 13% to 54% with an average of 41%, which indicates smectite illitization has advanced. The range of illite crystallinity index varies from 0.396 to 0.708, which shows the detrital source rocks also had been subjected to advanced levels of diagenesis and incipient greenschist-facies metamorphism.

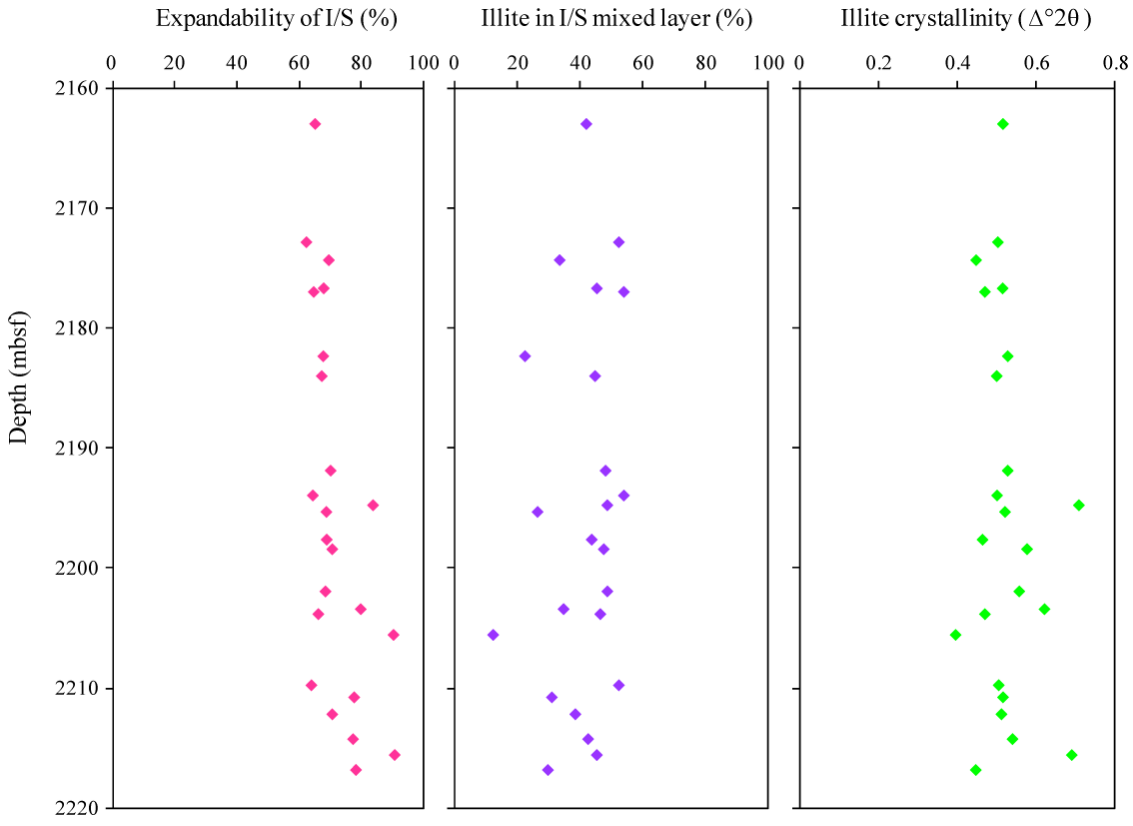

Figure 35. Plots of illite/smectite (I/S) mixed-layer clay expandability, proportion of illite in I/S mixed-layer clay and illite crystalinity index. Samples are all from Hole C0002P.

Table 10. Results of XRD analysis with values of illite/smectite (I/S) expandability, illite in I/S, and illite crystallinity index, Hole C0002P.

Core, section, interval (cm)	Depth (mbsf)	Intensity saddle (cps)	Intensity peak (cps)	Ratio saddle peak	Expandability (%)	Illite (002) / smectite (003) (°2θ)	Illite in I/S (%)	Illite crystallinity (Δ °2θ)
348-C0002P-								
1R-1, 0	2163.00	195	308	0.633	65	16.15	42	0.516
2R-1, 35	2172.85	276	393	0.702	62	16.37	53	0.503
2R-2, 43	2174.35	233	439	0.531	69	16.06	34	0.448
2R-3, 137	2176.70	236	416	0.567	68	16.21	46	0.515
2R-4, 27	2177.00	160	192	0.833	56	16.42	54	0.470
3R-1, 35	2182.35	247	433	0.570	68	15.92	23	0.528
3R-2, 60	2184.01	227	390	0.582	67	16.20	45	0.500
4R-1 39	2191.89	154	297	0.519	70	16.26	48	0.528
4R-2, 135	2193.96	210	322	0.652	64	16.42	54	0.501
4R-3, 72	2194.77	16	57	0.281	84	16.27	49	0.708
4R-4, 32	2195.33	250	456	0.548	69	15.98	27	0.521
4R-5, 125	2197.64	264	484	0.545	69	16.18	44	0.464
4R-6, 54	2198.43	232	457	0.508	71	16.25	48	0.577
5R-1, 95	2201.95	208	375	0.555	68	16.27	49	0.557
5R-2, 99	2203.43	12	35	0.343	80	16.07	35	0.621
5R-3, 0	2203.85	222	365	0.608	66	16.23	47	0.470
5R-5, 2	2205.57	201	1387	0.145	94	15.82	13	0.396
6R-1, 77	2209.77	260	392	0.663	64	16.37	53	0.505
6R-2, 37	2210.78	194	514	0.377	78	16.04	31	0.516
6R-3, 37	2212.19	248	489	0.507	71	16.10	39	0.512
6R-4, 103	2214.26	66	172	0.384	77	16.16	43	0.540
6R-5, 94	2215.58	15	56	0.268	85	16.21	46	0.690
6R-6, 77	2216.83	224	609	0.368	78	16.03	30	0.447

4.3 Results of microfabric analysis

Table 8 summarizes the values of standard deviation and index of orientation for each specimen that was imaged for microfabric using ESEM. Figure 36 shows all the ESEM images for specimens tested for permeability. The grains are mainly angular to sub-angular outlined and less than ~0.03 mm which is consistent with material type, silty claystone. In general, there is no obvious preferred orientation for grains in all specimens. Figure 37 catalogs the rose diagrams of particle orientation and corresponding values of standard deviation and index of orientation (see Table 11 for statistics). The cumulative frequency curves are plotted on Figure 38. The standard deviation for grain orientation ranges from 53.6 ° to 58.7 °, and the index of orientation ranges from 0.19 to 0.26. All such values are consistent with random arrangements of particles. However, the index of orientation appears to increase with depth especially for the microfabric on the vertical cut face (Figure 39).

Table 11. Statistics for microfabric calculated from analyses of environmental SEM images, Hole C0002P.

Core, section, interval (cm)	Depth of top (mbsf)	Horizontal section			Vertical section		
		Grains counted	Stand. Dev. orientation (°)	Index of orientation	Grains counted	Stand. Dev. orientation (°)	Index of orientation
348-C0002P-							
3R-01, 51	2182.51	645	57.5	0.20	531	57.8	0.20
4R-02, 98	2193.585	791	58.7	0.19	841	56.3	0.22
6R-01, 64	2209.64	886	53.6	0.26	687	54.9	0.24

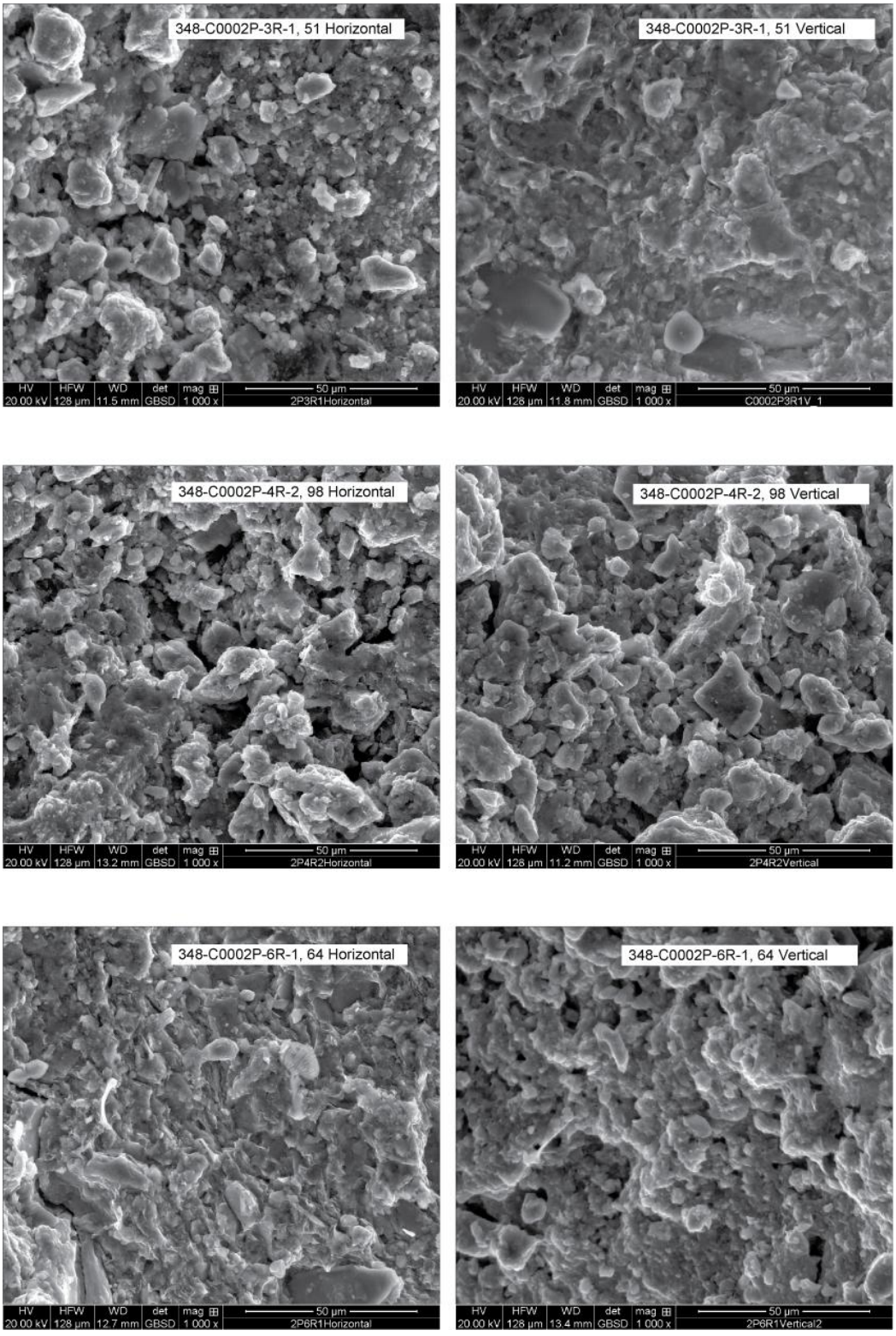

Figure 36. ESEM images for all specimens tested for permeability, Hole C0002P. Relative to the core axis, sections were cut parallel (vertical) and perpendicular (horizontal). See Table 4 for bedding dips.

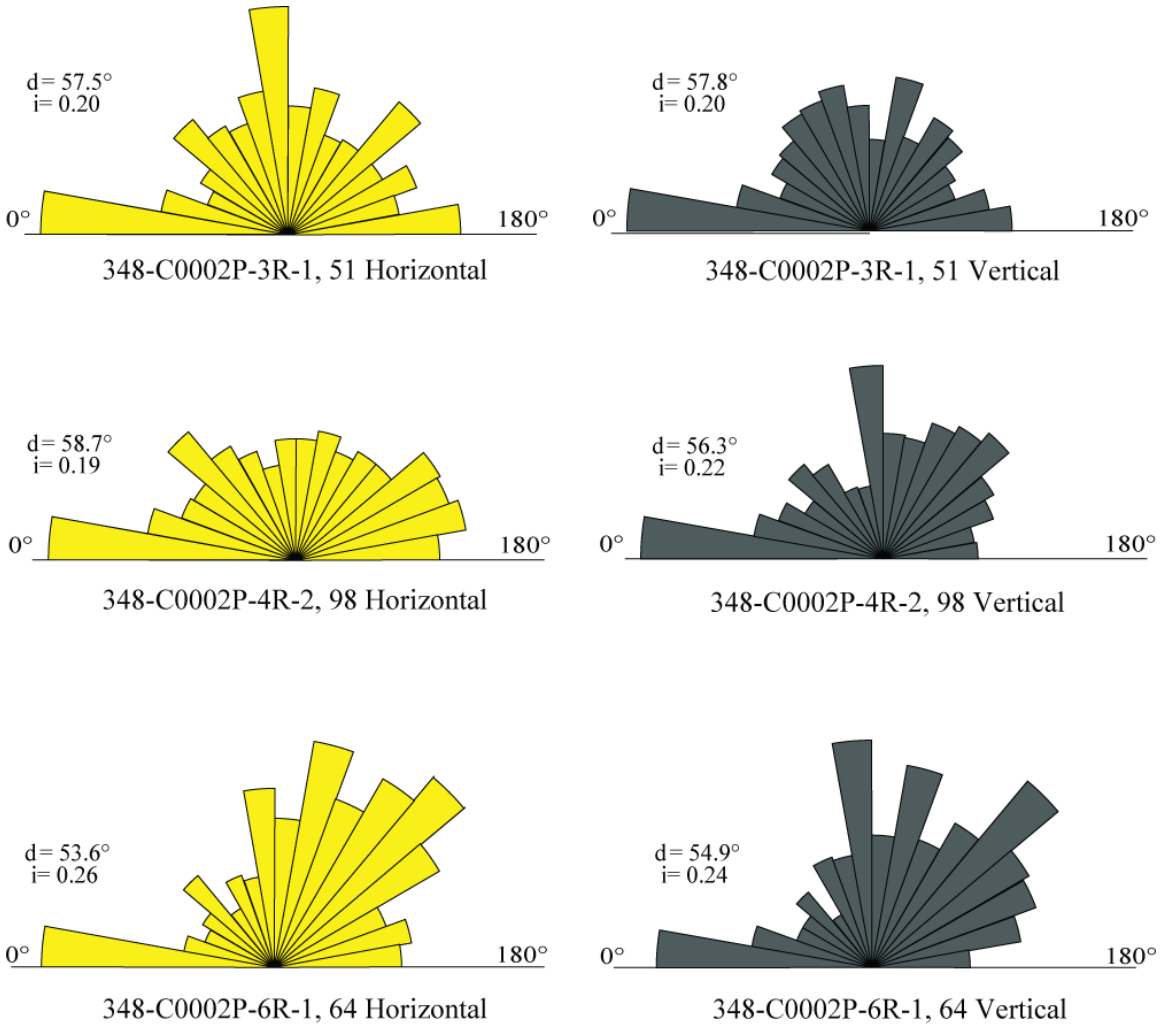

Figure 37. Orientation of grains (apparent long axis) measured on ESEM images. Relative to the core axis, sections were cut parallel (vertical) and perpendicular (horizontal). See Figure 23 for the corresponding ESEM images. Also shown are values of standard deviation (*d*) for grain orientation and values of microfabric orientation index (*i*).

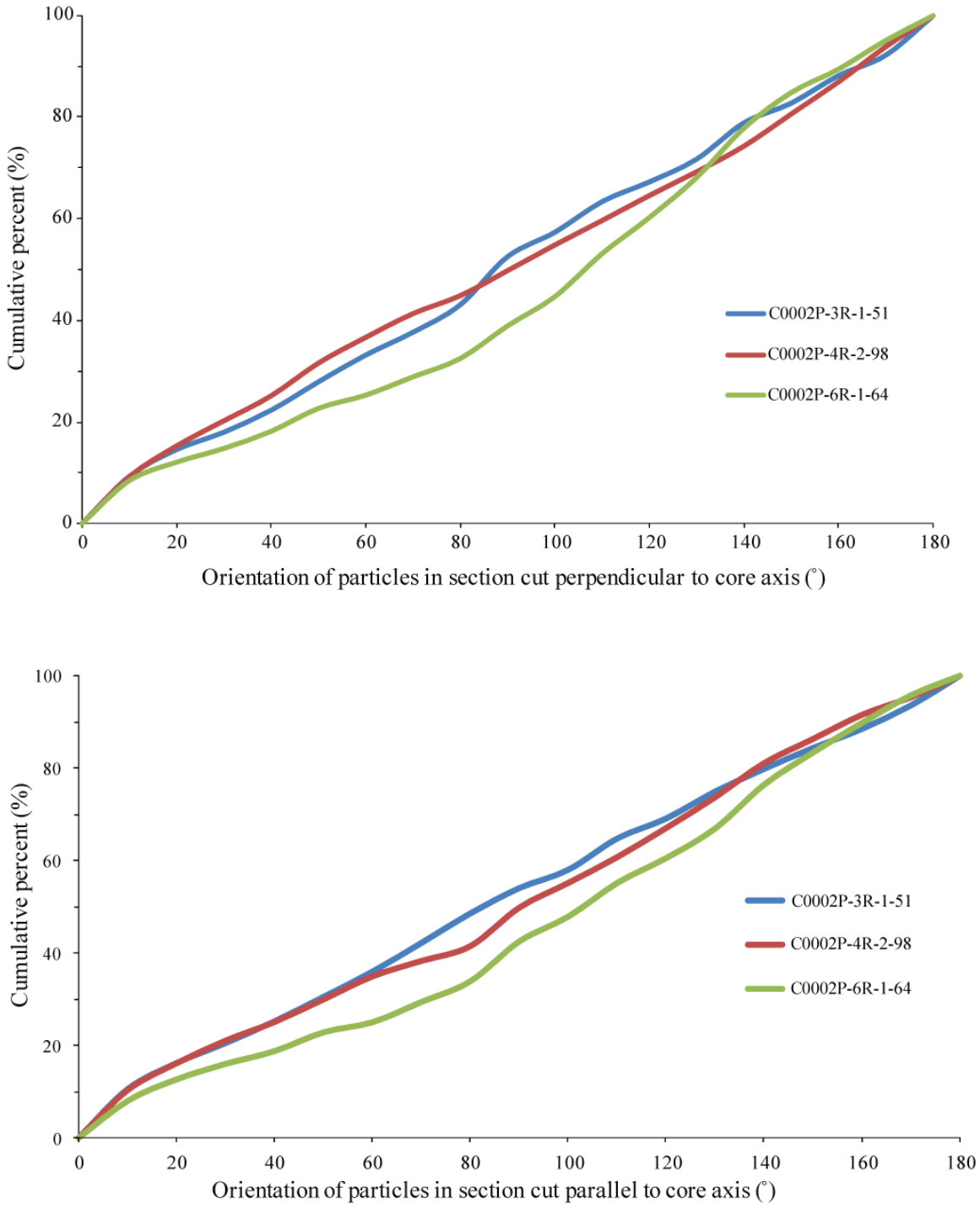

Figure 38. Cumulative frequency curves for grain orientations on horizontal sections (perpendicular to core axis) and vertical sections (parallel to core axis) imaged by ESEM, Hole C0002P.

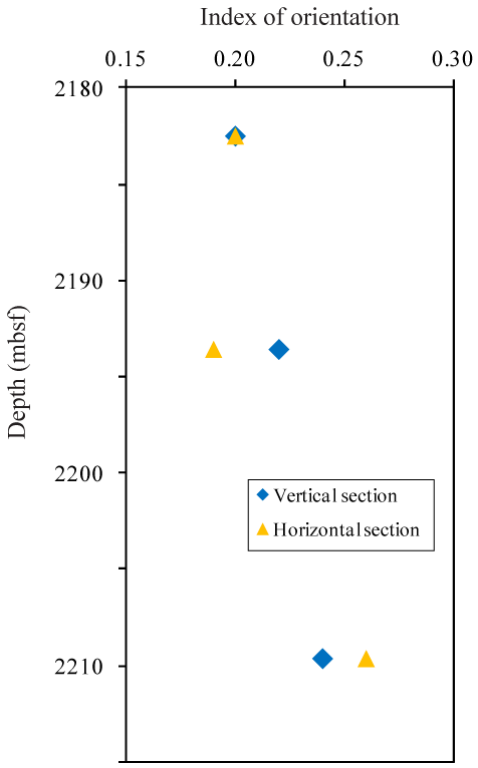

Figure 39. Index of orientation (horizontal and vertical sections) plotted as a function of depth at Hole C0002P.

Chapter 5 Discussion

5.1 Comparison of permeability values from Nankai Trough and other subduction zones

5.1.1 Other sites from Nankai Trough

Permeability tests have been conducted on samples from other ODP and IODP drilling sites in Nankai Trough. Figure 40 summarizes most of the results. The compilation for vertical permeability shows variability extending over six orders of magnitude.

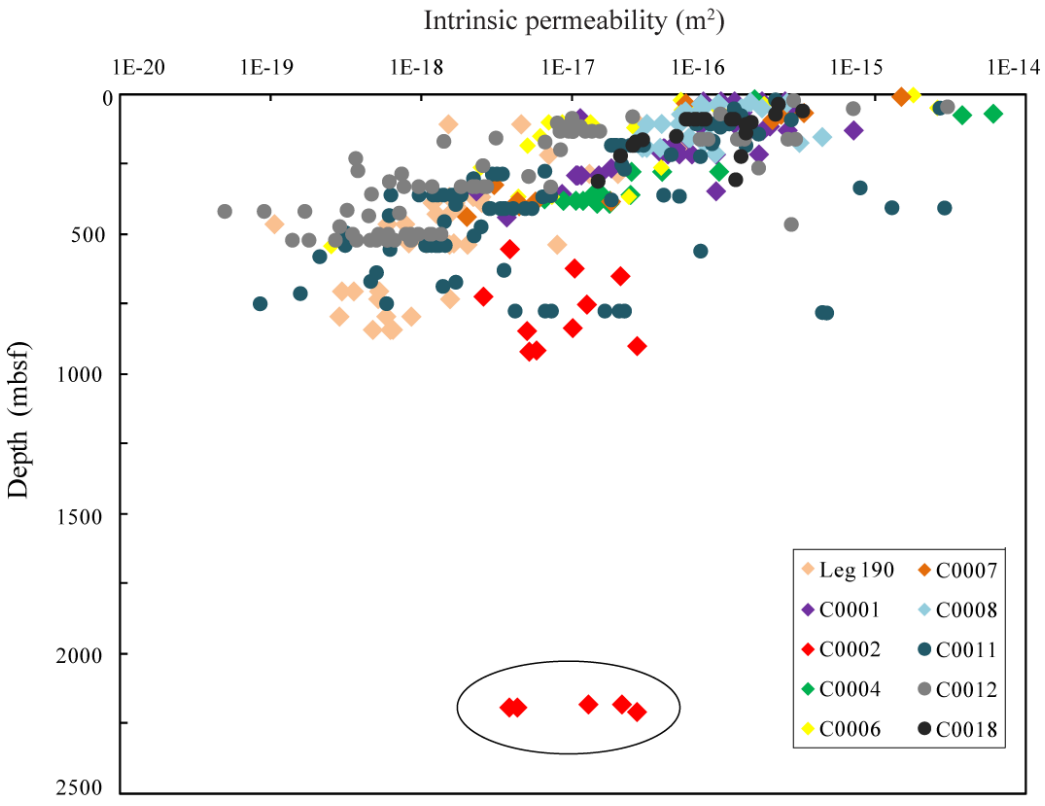

Figure 40. Values of vertical intrinsic permeability versus depth for specimens from Nankai Trough (see text for references). Circled values are from Hole C0002P (this study).

Site C0002:

. Guo *et al.* (2011) reported 11 CRS tests on WR samples from Expedition 315 Hole C0002B with the depth range of 553.80 mbsf to 846.83 mbsf. Samples are from the lower forearc basin facies and the basal starved-basin facies. Homogeneous and intact mud/mudstone was subsampled for the tests. The permeability values range from 2.56×10^{-18} to 2.67×10^{-17} m^2 with the vertical effective stress level from 4.041 MPa to 7.444 MPa. For samples from Hole C0002P (this study), the flow-through technique was used for testing the permeabilities of the silty claystone samples from 2182.51 mbsf to 2209.64 mbsf with two different effective stresses, 0.28 MPa and 0.55 MPa. The highest permeability value is 2.66×10^{-17} m^2 and the lowest is 3.80×10^{-18} m^2.

Sites C0001, C0004, C0008 and C0018:

Coring at IODP Site C0001 recovered the uppermost 1000 mbsf seaward of the Kumano Basin, where the megasplay fault system branches and approaches the surface (Expedition 314/315 Scientists, 2009b). Rowe *et al.* (2011), Saffer *et al.* (2011), and Yue *et al.* (2012) reported a series permeability results on WR samples from Site C0001 by conducting either constant-flow or CRS consolidation tests. Depth is from 25.21 mbsf to 440.34 mbsf, and effective stress varies from 0.03 MPa to 1.003 MPa. The lithology includes silty clay, clayey silt, and mud(stone). The highest value of vertical intrinsic permeability is 7.25×10^{-16} m^2 (129.22 mbsf), and the lowest value is 1.81×10^{-18} m^2 (346.75 mbsf).

Coring at IODP Site C0004 targeted the uppermost 400 mbsf seaward of the Kumano Basin uplift where the megasplay fault system branches and approaches the surface. Drilling penetrated through the fault into the footwall (Expedition 314/316

Scientists, 2009b). Saffer *et al.* (2011), Rowe *et al.* (2011), and Dugan and Daigle (2011) reported three CRS and constant-flow permeability test results for samples from Site C0004 with depth of 17.31 mbsf to 391.36 mbsf. Most of the samples are silty clay. The effective stress varies from 0.105 MPa to 0.55 MPa. The highest permeability value is 6.1 $\times 10^{-15}$ m^2 (69.39 mbsf), and the lowest value is 6.50 $\times 10^{-18}$ m^2 (375.08 mbsf).

IODP Site C0008 is located ~1 km seaward of Site C0004. Rowe *et al.* (2011), Saffer *et al.* (2011), and Dugan and Daigle (2011) reported constant-flow and CRS permeability test results for samples from 30.92 mbsf to 173.96 mbsf. The effective stress varies from 0.14 MPa to 1.569 MPa. The highest permeability value is 4.49 $\times 10^{-16}$ m^2 (173.96 mbsf) and the lowest value is 2.79 $\times 10^{-17}$ m^2 (152.84 mbsf).

IODP Site C0018 is located 5 km south-southwest of IODP Site C0008. It is located within a lower slope basin where mass transport deposits are included (Strasser *et al.*, 2011; Expedition 333 Scientists, 2012b). Guo and Underwood (2014), Daigle and Dugan (2014), and Screaton *et al.* (2013) reported CRS and constant-flow permeability tests on samples with depth range of 35.45 mbsf to 311.12 mbsf. The vertical effective stress changes from 0.14 MPa to 2.27 MPa. The highest permeability value is 3.33 $\times 10^{-16}$ m^2 (59.27 mbsf), and the lowest value is 1.47 $\times 10^{-17}$ m^2 (311.12 mbsf).

Sites C0006 and C0007:

IODP Site C0006 is located at the frontal thrust of the Nankai accretionary prism near the trench axis. Site C0007 is located trenchward of Site C0006 (see the "Expedition 314 Site C0006" [Expedition 314 Scientists, 2009b] and "Expedition 316 Site C0006 and Site C0007" [Expedition 316 Scientists, 2009b] chapters). Rowe *et al.* (2011), Dugan and Daigle (2011), Guo *et al.* (2011), and Ekinci *et al.* (2011) reported constant-flow and

CRS permeability tests on samples from Sites C0006 and C0007. Samples from Site C0006 were recovered from 2.39 mbsf to 542.91 mbsf, and samples from Site C0007 were from 9.02 mbsf to 438.62 mbsf. The effective stress varies from 0.015 MPa to 2.387 MPa. The highest permeability value is 1.5×10^{-15} m^2 (316-C0007B-1H-6 at 9.02 mbsf) and the lowest value is 2.51×10^{-19} m^2 (316-C0006E-17R-1, 65 cm at 542.91 mbsf).

Sites C0011 and C0012:

IODP Sites C0011 and C0012 were first cored during Expedition 322 to document characteristics of incoming sedimentary strata and uppermost igneous basement prior to their arrival at the subduction front (Saito *et al.*, 2009). Site C0011 is on the northwest flank of a prominent bathymetric high, and Site C0012 is near the crest of the knoll. Hüpers and Kopf (2012), Screaton *et al.* (2013), Dugan and Zhao (2013), Guo and Underwood (2014), and Daigle and Dugan (2014) reported constant-flow, incremental loading, and CRS tests on samples from 19.9 mbsf to 782.27 mbsf. Lithologies include silty clay, sandstones and hemipelagic mud(stones). The effective stress varies from 0.14 MPa to 6.06 MPa. The highest permeability is 2.30×10^{-14} m^2 (333-C0011D-49X-4, 100 cm at 363 mbsf) and the lowest value is 4.96×10^{-20} m^2 (322-C0012A-40R-5 at 418.57 mbsf).

Sites 1173, 1174 and 1177:

ODP Sites 1173 and 1174 are located along the Muroto transect, while Site 1177 is along the Ashizuri transect. Gamage *et al.* (2010) summarized the permeability values of samples from these sites with depth range from 199.9 mbsf to 842.75 mbsf. The effective stress used during the tests varies from 0.19 MPa to 12.386 MPa. The highest

permeability value is 5.18 $\times 10^{-17}$ m^2 (190-1173A-22H-2 at 199.9 mbsf) and the lowest value is 1.06 $\times 10^{-19}$ m^2 (190-1173A-49X at 464.71 mbsf).

5.1.2 Global data set

Gamage *et al.* (2011) also documented permeability results of mudstone from different subduction zones. Barbados (20.95 mbsf to 530.4 mbsf): samples are dominated by clay and claystone and tested under effective stress of 0.02 MPa to 1.215 MPa. The permeability values vary from 4.90 $\times 10^{-19}$ m^2 to 8.06 $\times 10^{-16}$ m^2. Costa Rica (80.85 mbsf to 598 mbsf): samples include silty clay, diatom ooze, nannofossil chalk and nannofossil ooze. The effective stress changes from 0.14 MPa to 0.62 MPa. The permeability values are 7.66 $\times 10^{-20}$ m^2 to 6.31 $\times 10^{-15}$ m^2. Peru (17.1 mbsf to 409.4 mbsf): samples vary from nannofossil ooze and chalk to diatom ooze. The effective stress is set from 0.14 MPa to 0.55 MPa for each sample. The permeability changes from 1.25 $\times 10^{-18}$ m^2 to 7.75 $\times 10^{-16}$ m^2. Figure 41 is plotted to show the relation between porosity and permeability at different sites.

Dewhurst and Aplin (1999) reported results of a series of hydraulic conductivity tests on seven natural, well-characterized specimens of London Clay mudstone at effective stresses between 1.5 and 33 MPa. Hydraulic conductivities of clay-rich samples (49-66% clay fraction) decreased from ~10^{-11} m/s to ~10^{-14} m/s (~10^{-19} m^2 to ~10^{-22} m^2 for permeability) over a porosity range of 0.48 to 0.25. At a given porosity, the hydraulic conductivities of two silt-rich samples (27 and 33% clay fraction) were 40-250 times greater than those of the five clay-rich samples. These variations are directly related to pore size distributions. Yang and Aplin (2007) also presented permeability data for 30 deeply buried mudstones (North Sea wells, Gulf of Mexico wells and Caspian Sea well)

at different effective consolidation stresses ranging from 2.5 to 60 MPa. Clay size particle varies from 13 to 66% and porosities range from 0.06 to 0.27. Vertical permeabilities range from 2.4×10^{-22} m^2 to 1.6×10^{-19} m^2. At higher porosities, clay content strongly influences the relation between permeability and porosity. These permeability values are all lower than those from either Nankai Trough or Gamage *et al.* (2011). This difference should mainly result from higher content of clay size particles and the higher effective stress applied on the specimens.

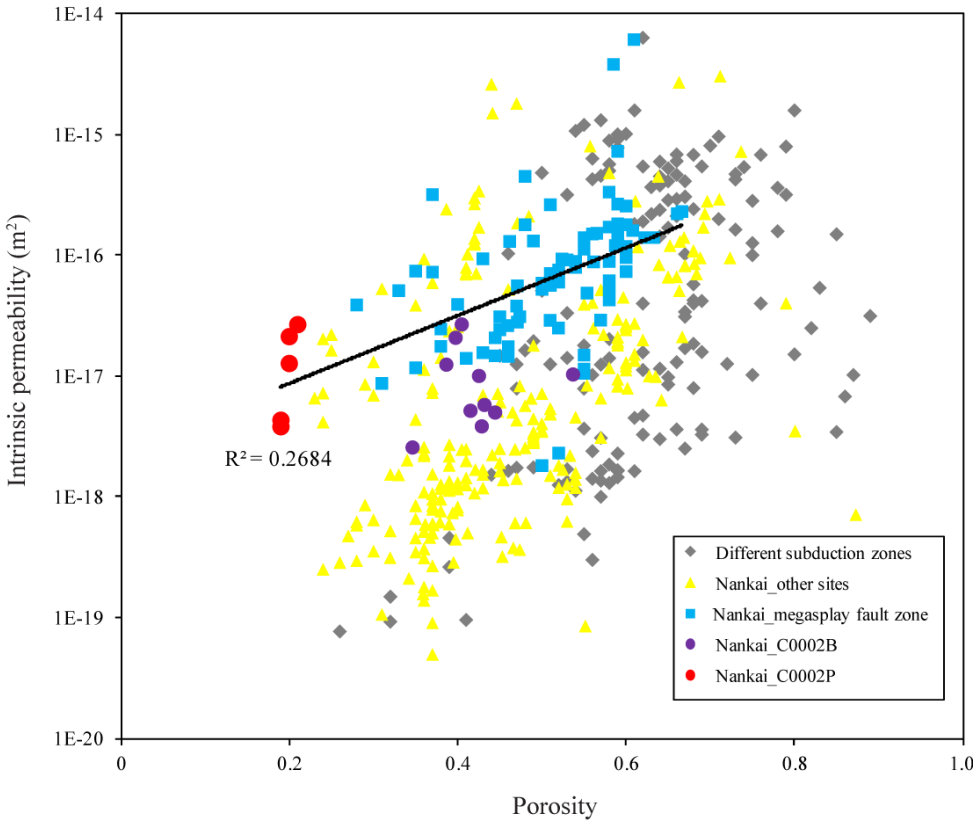

Figure 41. Relation between intrinsic permeability and post-test porosity for specimens from different subduction zones (see text for references).

5.1.3 Discussion

As mentioned above, many factors can affect the permeability for a certain sample, such as effective stress, lithology, pososity, and fracture density inside the

sample. Higher effective stress can result in lower permeability values for the same specimen, and in this study, the difference is not significant because change in effective stress is not great. However, by comparing data from other sources mentioned above, it shows that the difference can be 1-2 orders of magnitude. The main lithology for specimens in this study is characterized as clayey siltstone, while most of the specimens from other sites are mainly mud(stones). With coarser grains inside of clayey siltstone, their permeability values could be higher than mud(stones). In this study, SEM shows there are more fine grains inside the specimen 348-C0002P-4R-02, which could be part of the reasons that its permeability values are lower than the rest of the two specimens. During the trimming, specimens dried out very quickly so there was moisture loss while measuring the porosities (lower than shipboard data), and this could also slightly affect the interpretations here.

Figure 40 shows that intrinsic permeability generally decreases with increasing depth, and at the same depth range, the differences of permeability results are over five to six orders of magnitude. This could result from the differences in lithology and effective stress applied during the tests. The permeability values for samples from Hole C0002P are similar to the results from the shallow parts of the accretionary prism (Hole C0002B). Figure 41 shows permeability increases with the increasing porosity in general, and most data from Nankai Trough fall within the range of the global data set. Results from Hole C0002P seem to correlate better with shallow megasplay fault zone data and exhibit relatively higher permeability values compared with data from other sites. However, the linear regression analysis shows that R^2 is only 0.2684 for the correlation in this study, so more data from Hole C0002P is needed for further study.

One of the possible reasons for the relatively higher permeability in the cored interval of Hole C0002P is the microfractures and steep bedding. According to the shipboard structural and logging results (Expedition 348 Scientists, 2015b), there are 27 minor faults observed in the cored interval. In the interval where the specimens of this study cored from, there are 14 minor faults (both normal and reverse faults). In most of the cored interval, bedding dips are greater than 75°. Sand layer grading was used as one of the indicators to determine the facing direction of the bedding; most layers are upright. This can result in higher permeability especially when the trimming direction is parallel with the bedding planes because fluids can easily flow along the bedding planes. The resistivity images for the cored interval also show steep bedding angles and high density of fractures and faults, which indicate this interval is strongly deformed.

Boutt *et al.* (2012) discussed the role of fractures on overall prism permeability structure at a megascopic *in-situ* scale. They concluded that natural fractures could be responsible for permeability higher than matrix permeability in lab-scaled core samples, which has implications for the permeability structure of deformed accretionary prisms. Bourlange *et al.* (2004) also conducted a series tests on samples from ODP Leg 190 to partially document the effect of fracture on permeability. They showed that permeability increases as a result of the formation of a fault-like slip plane in the sample when confining stress is low (~0.2 MPa). The higher permeability document in my study could be caused by the high densities of fracture because they were observed during the trimming and the specimens tended to break easily (see Figure 14 for examples).

5.2 Comparison of clay mineralogy at different Nankai drilling sites

Many studies pointed out that clay minerals can provide important information for determining the detrital origin of sediment and dispersal patterns (e.g., Moros *et al*., 2004; Underwood and Pickering, 1996), and the mineral assemblages are closely related to the geology and weathering regime of the adjacent hinterland (Gingele *et al*., 2001b) . For example, detrital illite resists chemical weathering and is common in most continental soils (Biscaye, 1965). Illite and chlorite are also formed via mechanical weathering of plutonic, metamorphic, and sedimentary rocks in continental areas (Chamley, 1989). Minerals of the smectite group form from different sources and processes, and they are widely regarded as chemical weathering products or submarine alteration of volcanic rocks and pedogenesis in arid-to-semiarid climates (e.g., Biscaye, 1965; Chamley, 1989). Smectite group minerals can also be detrital or authigenic in origin (Phillips *et al*, 2014). For example, Petschick et al. (1996) pointed out that clay minerals are main constituents of most modern abyssal sediments and can be indicators for paleoclimatic and paleoceanographic conditions. They studied 850 surface samples of the South Atlantic and the Antarctic Ocean for clay content and composition (smectite, illite, chlorite, and kaolinite). Specifically, they found that clay fractions with more than 50% smectite are found in some spots in the Antarctic Ocean connected to volcanic environments, and it is a local non-continental origin of smectite resulting from the erosion of alterated basaltic rocks and detrital volcanic glass, which undergo submarine weathering or early diagenetic transformation (Hodder *et al*., 1993). Phillips *et al*. (2014) documented clay mineral composition of Indian continental margin sediments in the Bay of Bengal, Arabian Sea, and Andaman Sea, and they found smectite is the most abundant clay

mineral in the Andaman Sea sediments likely due to weathering of volcanic sources along the Sunda Arc.

Cutting samples from Hole C0002F is within lithologic units IV (upper accretionary prism) and V (accreted trench or Shikoku Basin hemipelagic deposits) with the age of <5.59 Ma, and the main lithology is greenish gray silty claystone. Smectite is the most abundant clay-size mineral with 39.2 wt% average, followed by illite (37.4 wt%), chlorite (19.9 wt%), kaolinite (3.0 wt%), and quartz (0.6 wt%). The core samples from Hole C0002P are from lithologic Unit V. The primary lithology is greenish gray silty claystone and fine silty claystone with minor siltstone and fine sandstone. The dominant clay-size mineral is still smectite (average 39.5%), followed by illite (32.4%), chlorite/kaolinite (25.1%), and quartz (3.0%). Calcareous nannofossils indicate the age of this interval is ~9.56 – 10.54 Ma (late Miocene). One sample (348-C0002P-5R-5, 2 cm) contains 98% smectite and can be defined as bentonite.

To compare the clay mineralogy in the units with results from coeval Miocene strata, along Muroto transect area, strata from Site 1178 consist of late Miocene trench wedge facies with smectite as the dominant clay (~45%), followed by illite (~30%), and chlorite/kaolinite (~20%) (Underwood and Steurer, 2003). At Site 1173 (Miocene Shikoku Basin facies), the average abundance of smectite is ~40%, followed by illite (~30%) and chlorite/kaolinite (~20%). At Site 1174 (Miocene Shikoku Basin facies), the average of smectite decreases to ~20% (lower because of I/S diagenesis), and illite is ~35%, followed by chlorite/kaolinite ~30%. Along Ashizuri transect, Site 1177 mainly consists of Shikoku Basin facies from Pliocene to early Miocene. Smectite slightly

increases with an average of ~50% for Miocene age. Illite is ~30% followed by chlorite/kaolinite ~15% (Steurer and Underwood, 2003).

Underwood and Guo (2013) reported on the clay-size fraction at Sites C0011 and C0012, which are located in the Shikoku Basin. The age varies from ~7.6 to ~18.9 Ma (early to middle Miocene), and smectite is the dominant mineral. Smectite varies significantly from 35% to 100% with a substantial number of bentonites. The total abundance of smectite on average is ~60%, followed by illite ~30% and chlorite/kaolinite ~15%. Through the comparisons, the abundance of detrital smectite from Holes C0002F and C0002P may be reduced by the effects of diagenesis.

In Kumano transect, I compare the clay mineralogy from deep interior of accretionary prism with those from different structural zones. Illite is the dominant clay mineral in all the units with younger age:

Forearc basin (shallow part of C0002): Guo and Underwood (2012) summarized the clay mineralogy through four lithologic units at Site C0002. Through lithologic Unit I to Unit IV (Quaternary to late Miocene), the average abundance of illite decreases from ~38% to ~31%, smectite increases from ~22% to ~41%, chlorite decreases from ~22% to ~15%, quartz decreases from ~13% to 6%. The shift toward higher contents of smectite is consistent with the late Miocene age of the shallow accretionary prism (Underwood and Steurer, 2003).

Shallow megasplay fault zone (Sites C0001, C0004 and C0008): The ages of all units are all younger (Pliocene to Quaternary) than the cored interval at Hole C0002P, and the dominant clay mineral is illite (~33 to 38%), followed by smectite (~26 to 36%),

chlorite (~15 to 23%), quartz (~4 to 10%) and kaolinite (~4 to 8%) (Guo and Underwood, 2012).

Frontal thrust zone (Sites C0006 and C0007): Units in C0006 and C0007 are latest Miocene (5.32 Ma) to Pleistocene. Illite is still the dominant clay mineral in the younger units (~35 to 39%), followed by smectite (~23 to 27%), chlorite (~24 to 26%), quartz (~8 to 10%) and kaolinite (~2 to 4%). In the older units (latest Miocene), smectite becomes the most abundant mineral (~37 to 39%), and followed by illite (36%), chlorite (17%), quartz (6%) and kaolinite (3 to 6%) (Guo and Underwood, 2012).

5.3 Interpretation of sediment dispersal system

The present-day Nankai Trough is characterized by a thick terrigenous trench-sediment section entering the subduction zone (Ike *et al.*, 2008). The frontal accretionary prism consists of offscraped and underplated materials from the trench and the upper Shikoku Basin (Taira and Ashi, 1993). Sediment in the Shikoku Basin and the trench wedge is currently supplied by rapid uplift and erosion of a collision zone between the Honshu arc and Izu-Bonin arc, and a system of submarine canyons that are located offshore Shikoku Island, Kii Peninsula and Honshu (Figure 42) (Underwood and Pickering, 1996).

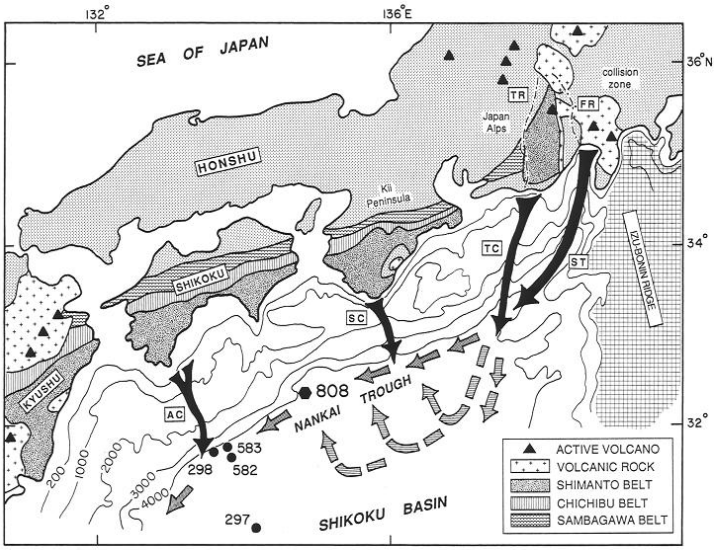

Figure 42. Index map showing the regional geography, geology and bathymetry (in meters) of the Nankai study area of southwest Japan. Numbers refer to DSDP and ODP site localities. Large black arrows symbolize major submarine canyons. Key: ST = Suruga Trough; TC = Tenryu Canyon; SC = Shino-misaki Canyon; AC = Ashizuri Canyon. Smaller arrows represent inferred pathways for turbidity currents within the trench, including flow-reflection trajectories off the seaward slope (Pickering et al., 1992; Underwood et al., 1993a). Major drainage basins in the Izu-Honshu collision zone include the Tenryu River (TR) and the Fuji River (FR) (Underwood and Pickering, 1996).

Underwood and Fergusson (2005) explained the regional sediment dispersal system during different time intervals (Figure 43). First, the late Quaternary dispersal system (less than 0.46 Ma) has been dominated by influx from the collision zone between the Izu-Bonin volcanic arc and the Outer Zone of southwest Japan. The late Pliocene to early Pleistocene dispersal system (2.0-0.46 Ma) shows a compositional shift to funnel most of the sand through canyons and channels along the southern margin of Shikoku. The late Miocene to late Pliocene dispersal system (9.6-2.0 Ma) was dominated by smectite. Similar clay assemblages also entered the Shikoku Basin on the backarc side of the volcanic provenance during the same periods of time (Chamley, 1980). The Kuroshio Current plays an important role by transporting clay in the surface water from Kyushu

and Shikoku toward the northeast, and the strength of that current probably intensified around 3 Ma.

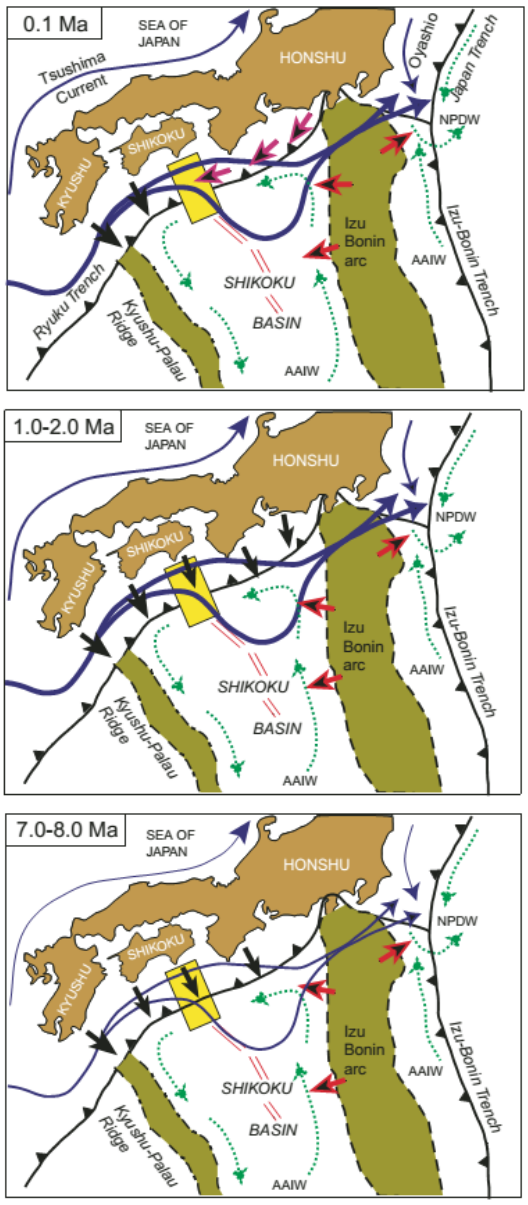

Figure 43. Schematic illustrations of sources and transport routes for sediments entering the Nankai subduction margin during three intervals of time: late Quaternary (0.1 Ma), late Pliocene–early Pleistocene (1.0–2.0 Ma), and late Miocene (7.0–8.0 Ma). Yellow box = location of study area. Surface currents are shown in solid blue; meander in Kuroshio Current is generalized from White and McCreary (1976). Bottom currents are shown in dashed green: AAIW = Antarctic Intermediate Water; NPDW = North Pacific Deep Water. Bold arrows depict transport directions for turbidity currents and other gravity flows: red = IzuBonin arc source; purple = Izu-Honshu collision zone source; black = Outer Zone source (Underwood and Steurer, 2003).

In the Kumano transect, the megasplay fault separates the Kumano forearc basin from the outer wedge, where sandy turbidites and hemipelagic trench deposits are deformed by normal in-sequence imbricate thrusts (Park *et al.*, 2002; Bangs *et al.*, 2004). The frontal accretionary prism is mainly composed with offscraped sand-rich and gravel-rich packets, similar to what has been found along the Muroto and Ashizuri transects. The source of the Quaternary sediments is likely from the Suruga Trough and Tenryu Canyon. However, at the megasplay fault zone, the prism mainly consists of fine-grained sediment (Underwood and Moore, 2012). Kimura *et al.* (2011) discussed the synsedimentary activity of the megasplay fault and showed there is a complex interaction between fault propagation folding, seafloor slumping and sliding, faulting and deformation of shallow strata, and widespread deposition of mass transport deposits and debris slides. Buchs *et al.* (2015) shows that the Kumano Basin initiated as a trench-slope basin in the early Quaternary (~1.93 Ma) and it progressively evolved towards an upper slope environment. Turbidite confinement increased in the basin after a major tilting event in the middle Quaternary with only limited longitudinal transport in the upper forearc. In the late Quaternary, transverse canyons became a major control on the sediment flow routing during maturation of forearc basins. Long-distance longitudinal flows along convergent margins are principally restricted to near-trench environments, even in the presence of large forearc basins.

Fergusson (2003) discussed the provenance of Miocene-Pleistocene turbidite sands and sandstones from ODP Leg 190. He documented that sands from the Pleistocene trench-fill (Sites 1173 and 1174) have a source in the Izu collision zone in central Honshu. Sands from the Pleistocene-Pliocene slope and accreted trench fill (Sites 1175 and 1176)

consist volcanic rock fragments as main silicic composition, and the potential sources are uplifted subduction complexes of southwest Japan. There are more abundant fine-grained sedimentary rock fragments in sands from upper Miocene trench fill (Site 1178), and they were probably derived from the island of Shikoku but the source area may have been Miocene forearc basin successions that were largely removed by erosion. Sand in the upper Miocene turbidites of the lower Shikoku Basin (Site 1177) were similar to Site 1178, and the lower part of the Miocene turbidites are similar to those at Sites 1175 and 1176 and were derived from a continental source with plutonic and volcanic rocks, possibly the Inner Zone of southwest Japan.

Smectite is the dominant clay mineral in this time interval, and smectite group minerals are key tracers for interpretations of clay provenance (Fagel *et al.*, 2001). Considering the age (~9.56 – 10.54 Ma) of the interval in this study, the possible sources could be either central Japan which contains older welded tuffs of middle-late Miocene age (14-4 Ma) (Otofuji *et al.*, 1997; Kitazato, 1997) and associated granodiorite bodies (12-7 Ma) (Saito *et al.*, 1997); or the Izu-Bonin island arc where marine ash layers record four pulses of volcanic activity since the middle Miocene (Cambray *et al.*, 1995). Moreover, values of illite crystallinity show that detrital source rocks during the late Miocene consistent with rock units currently exposed in the Outer Zone of SW Japan.

5.4 Clay diagenesis

At subduction zones, fluid-rich sediments from the subducting plate can either underthrust with the subducting plate or accumulate to form the accretionary wedge. Porosity in those sediments will be reduced because of the lateral tectonic stress and

increasing burial depth. After porosity is reduced, the dehydration of smectite-group clay minerals becomes the largest remaining source of fluid (Moore and Vrolijk, 1992; Saffer *et al.*, 2008). This dehydration process is important in controlling both the hydrologic and mechanical behavior of subduction zones (Vrolijk, 1990; Moore and Vrolijk, 1992; Underwood, 2002). Once dehydration ends, the updip limit of seismogenic zone may be influenced by lower fluid pressure, increasing the effective normal stress (Moore and Saffer, 2001; Spinelli and Saffer, 2004).

In clay-rich sediments, transition of smectite to illite is a common reaction during burial diagenesis, and reaction progress occurs through illite/smectite mixed layers (e.g., Lanson *et al.*, 2009). Hower *et al.* (1976) documented a detailed mineralogical and chemical investigation from a well in Oligocene-Miocene sediment of the Gulf Coast. The results showed that smectite/illite conversion undergoes from less than 20% to about 80% illite layers between ~40°C and ~95°C, after which there are no significant changes detected by XRD. As the smectite-illite transition proceeds, the percentage of illite in the mixed-layer structure increases and the organization of I/S mixed layers changes from random to ordered (Reynolds and Hower, 1970; Altaner and Ylagan, 1997). I/S clays are usually disordered ($R = 0$) with less than 50% illite and $R = 1$ (50:50) ordering usually occurs at 55%-60% illite (Moore and Reynolds, 1997).

Freed and Peacor (1989) pointed out that the temperature windows for diagenesis reaction can deviate significantly, so the S-I transition should not be used as an absolute geothermometer. They examined well-cuttings and core samples from four Gulf Coast areas, and found that the smectite transformation usually begins around 58°C to 92°C and completes the transition with approximately 80% illite within mixed illite/smectite layer

at ~88°C to 142°C. Because factors other than temperature are involved, such as heating time and potassium availability (e.g., Huang *et al.*, 1993), the temperature range illitization varies for different sites.

Underwood *et al.* (1993) documented at ODP Site 808 that illite content of I/S consistently increases with depth. The seafloor temperature at Site 808 is ~2 ℃, and the average geothermal gradient recorded in the upper 350 m of the stratigraphic section is ~110 ℃/km (Shipboard Scientific Party, 1991b). By assuming a linear geothermal gradient, the beginning of illitization is ~65 ℃ (~560 mbsf) and ends at ~135 ℃ (~1220 mbsf) (modified to ~144 ℃ by Shipboard Scientific Party 2001c, 2001d). The illite percentage in I/S mixed-layer is ~20% to ~80% in this interval. Masuda et al. (2001) also provided a detailed observation on the conversion of smectite to illite in mudstones from Site 808. At 512 mbsf (~50 ℃), there are three types of phases presented: detrital minerals, volcanic glass, and smectite. Smectite shows the texture typical of alteration from volcanic glass. At 685 mbsf (~70 ℃), the clays range from smectite to illite. Thin packets of illite layers occur embedded within layers of either I/S or smectite. At 907 mbsf (~90 ℃), it consists smectite and I/S and the I/S is dominantly ($R = 1$) I/S. This depth is shallower compared with depth at the projected completion temperature documented by Underwood et al. (1993). At 1147 and 1176 mbsf (~115 to 120 ℃), the samples closely resemble those from 685 and 907 mbsf, and layer sequences consist either of smectite or ($R = 1$) I/S.

Steurer and Underwood (2003) reported the smectite illitization progress at Sites 1173, 1174 and 1177. At Site 1173, the percent illite in I/S clays increases from ~15% to 50% starting at 350 mbsf with no ordering, while at Site 1174, the illitic component of

I/S mixed-layer clay increases consistently below 590 mbsf, reaching a maximum of 89%, but $R = 1$ ordering does not occur. At Site 1177, the I/S mixed layer clays show no pattern of systematic change with depth, and the percent illite in I/S clays reaches a maximum of 42%, but most values are <25% with random ordering. Heat flow value is much lower at Site 1177 (~63 mW/ m^2) compared with Sites 1173 and 1174 (~130 mW/m^2 to 180 mW/m^2), and this could be the reason that retards the illite-smectite reaction.

Increased sediment thickness, steeper taper angle, higher heat flow, and slower convergence rate can all lead to more advanced reaction progress, and heat flow has the largest effect among all the factors (Saffer *et al.*, 2008). It can be seen from the discussion above that the smectite-illite reaction progress advances further landward (from ~20% to ~85%), from Site 1173 to 1174 and 808. Saffer *et al.* (2008) explained that the higher heat flow along the Muroto transect (range from ~150 to 230 mW/m^2) drives this reaction outboard of the trench in the deeper stratigraphic intervals. They also compared changing of the heat flow and smectite illitization progress along the strike of the Nankai Trough by discussing the results from both Muroto transect (Sites 808, 1173 and 1174) and Ashizuri transect (Site 1177). Along the Ashizuri transect, heat flow values range from ~75 to 130 mW/m^2, and they are consistent with crustal ages of 19-25 Ma. The low heat flow is the main reason that there is no smectite illitization progress initiated at Site 1177, and partly attributed to rapid sedimentation and burial in the trench axis and to tectonic thickening (e.g., Kinoshita and Yamano, 1995; Yamano *et al.*, 2003). Along the Muroto transect, the heat flow is considerably higher than expected for ~15 Ma crust, and the discrepancy has been attributed to volcanic activity and possible

hydrothermal activity along the Kinan Seamount Chain as recently as 6-7 Ma that reheated the crust (Wang *et al.*, 1995; Moore *et al.*, 2001a; Sato *et al.*, 2002; Yamano *et al.*, 2003; Spinelli and Underwood 2005).

Harris *et al.* (2011) documented the heat flow along the Kumano transect from the results of IODP Expeditions 315 and 316. The study region includes the frontal thrust zone (Sites C0007 and C0006), the megasplay fault zone (Sites C0008, C0004, and C0001) and in the Kumano forearc basin (Site C0002). Heat flow values of the Nankai accretionary prism are lower than expected and range from 60 to 36 mW/m^2. With bathymetric or sedimentation corrections, the heat flow values are increased by about 12% and vary from 70 mW/m^2 near the toe of the deformation front to 57 mW/m^2 at the Kumano Basin (Site C0002). In general, heat flow values decrease with distance landward of the deformation front, consistent with subduction.

Sugihara *et al.* (2014) reconstructed the temperature profile at Site C0002 using observatory results (Figure 44). The grain thermal conductivity (k_g) at Hole C0002P ranges from 2.1 to 3.4 W/(m•K) with average of 2.6 W/(m•K), so only the curves with k_g = 2.5 W/(m•K) are considered here. The temperature at 900 mbsf is estimated to be 37.9 ℃ with the heat flow of 56 ± 1 mW/m^2. This heat flow is used to extrapolate the temperature below 900 mbsf. As a result, the temperature is ~80 ℃ to 100 ℃ between 2,000 and 3,000 mbsf (drilling interval for Hole C0002P). From 3,000 to 5,200 mbsf, where the megasplay fault is, the temperature range is ~100 ℃ to 150 ℃. A plate boundary fault is approximately at 7,000 mbsf, and from 5200 to 7000 mbsf, the projected temperature is ~150 ℃-175 ℃. IODP Expedition 348 shipboard measurements show the temperature for Hole C0002P is approximately between 85 ℃ to 110 ℃ from

1981 to 2441 mbsf (Expedition 348, 2015b) which agrees well with the temperature profile reconstructed by Sugihara *et al.* (2014).

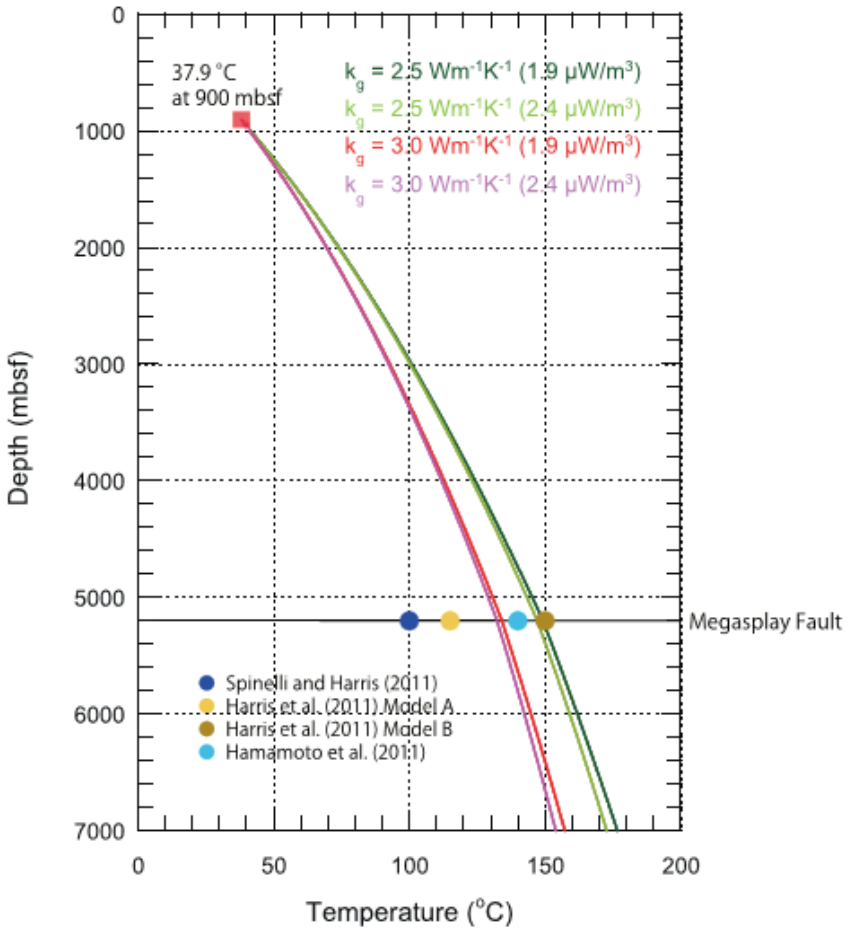

Figure 44. Estimated temperature profiles from 900 to 7,000 mbsf. Temperature-depth profile is based on newly derived in-situ temperature from the long-term borehole monitoring system and basal heat flow at 900 mbsf. The temperature data are compared with estimated reported in previous studies (Harris *et al.*, 2011; Spinelli and Harris 2011; Hamamoto *et al.*, 2011). k_g = grain thermal conductivities(Sugihara *et al.*, 2014).

From Figure 41, the depth interval for ~40 ℃ to 95 ℃ (general documented temperature window for smectite illitization progress) is between ~1100 and 2800 mbsf. The depth interval of Holes C0002F and C0002P should be a good range for the reaction progress to be initiated but may not be the range for the reaction to be completed. In this study, the average illite percentage in I/S mixed layer from the XRD results of Hole

C0002F is 26%, and 41% within Hole C0002P (maximum value of 53%), so by considering the temperature range together, it is reasonable to say the smectite illitization process has been initiated and advanced, which agrees well with what is expected. This transition is also expected to be completed near the megasplay fault.

5.5 Implications for deeper drilling research

The transition from aseismic to seismic slip is affected by such variables as fault zone composition, consolidation state, and pore fluid pressure (Saffer and Marone, 2003). The ultimate goals for NanTroSEIZE project are to sample the megasplay fault at seismogenic depths and monitor in situ conditions over the earthquake cycle. Expedition 348 reached a depth of 3058.5 mbsf, which is the world record for scientific ocean drilling. A suite of samples was successfully collected and used to characterize the deep interior of an active accretionary prism.

If the sediments are with low permeability, the higher pore pressure could be built up under rapid loading, and this can decrease the effective stress then further decrease the shear strengh. However, the very steep bedding dips, which probably are one of the reasons that cause the higher permeability within the cored interval of Hole C0002P, would help the drainage of pore fluids, and retention of near-hydrostatic pore pressures through the accretionary prism. If similar conditions and rock properties extend all the way down to the megasplay fault, it could further increase the effective normal stress and shear strength.

Clay diagenesis results from Hole C0002P indicates that temperature for the updip limit of the seismogenic zone in Nankai accretionary prism supports the hypothesis

of Hyndman *et al.* (1997), which documented the temperature limit is 100 to 150 ℃ for the onset and completion of smectite-illite transition. The temperature range in Nankai accretionary prism is relatively higher than the hypothesis of Hyndman *et al.* (1997) though. Smectite illitization is expected to be completed near the megasplay fault (~5200 mbsf).

As for future drilling, more core samples will be invaluable to describe the hydrological properties in order to evaluate the pore pressure and shear stress in deeper part of the accretionary prism. Also, adding results from deeper intervals can extend the document I/S reaction progress to higher in situ temperatures in order to fully test hypotheses regarding mechanisms and processes that control the aseismic-seismic transition. Scientists need to generate empirical ground truth in order to calibrate the current numerical models, as well as to project the experimental results to the region with higher pressure and temperature.

Chapter 6 Conclusions

6.1 Permeability and microfabric analysis

Samples were collected from the deep interior of the Nankai Trough accretionary prism during the IODP Expedition 348 in Hole C0002P. Samples were cored from 2174.985 to 2209.640 mbsf and from lithologic unit V (trench or Shikoku Basin hemipelagic deposits). Constant-flow permeability tests were completed to calculate intrinsic permeability for three silty claystone specimens on vertical flow direction at two values of effective isotropic confining stress, 0.28 and 0.55 MPa. Due to small sample size, no specimen was tested for the horizontal flow direction to document the anisotropy of permeability. The highest permeability value among all the results is 2.66×10^{-17} m^2 (348-C0002P-6R-01, 64 cm 0.28 MPa) while the lowest value is 3.80×10^{-18} m^2 (348-C0002P-4R-02, 98 cm 0.55 MPa).

By merging the results from other NanTroSEIZE drilling sites, most of the permeability values decrease with the increasing depth, but the permeability results vary up to 6 orders of magnitude at the same depth range. Permeability values for samples from deeper parts of Site C0002 (Hole C0002P), however, are similar to values from the shallow part of Site C0002 (Hole C0002B). Permeability also increases with increasing porosity in general, and results from C0002P seem to correlate better with data from the shallow megasplay fault zone with relatively higher values than the data from other sites. The possible reasons for these variations could be different lithology, different effective stress used during the tests, and more importantly, the steep beddings (close to 90°) and high density of microfractures inside the specimens.

SEM images show the variability of grain size and compositional layering inside of the specimens. The standard deviation and index of microfabric orientation are consistent with random arrangements of particle. The index of orientation increases slightly with depth especially for the microfabric on the vertical cut face.

6.2 Clay mineralogy and diagenesis

XRD analysis on clay-size fraction for cuttings and cluster samples from Holes C0002F and C0002P demonstrates that smectite is the dominant mineral, which agrees well with what has been concluded that the smectite-rich clay mineral is typical of middle to late Miocene deposits. The results are consistent with the accretion of either Miocene trench-wedge or Miocene Shikoku Basin sediments. On average, the expandability of illite/smectite mixed-layer clay is equal to 70% from Hole C0002F, and 69% from Hole C0002P, which is similar to values from other drilling sites of Nankai showing the expandable clay is probably detrital in origin. The average proportion of illite in the I/S mixed-layer is 26% from Hole C0002F, which indicates that smectite-illite transition has initiated. Illite abundance in I/S is 41% from Hole C0002P, which indicates that smectite illitization has advanced in this cored interval. Completion of this reaction is expected to see near the megasplay fault. Values of illite crystallinity show that detrital source rocks during the late Miocene had been subjected to advanced levels of diagenesis and incipient greenschist-facies metamorphism, consistent with rock units currently exposed in the Outer Zone of SW Japan.

6.3 Future work

The ultimate scientific goal of NanTroSEIZE is to utilize ultra-deep riser drilling to penetrate the seismogenic plate interface at a depth of 6000-7000 mbsf and install long-term borehole observatories within the fault zone (Tobin and Kinoshita, 2006; Underwood and Moore, 2012). One of the project's main objectives is to understand the mechanisms and processes controlling the updip aseismic-seismic transition of the megathrust fault system. My study contributes to evaluate one of the related hypotheses, which is that systematic, progressive material and state changes (e.g., pore pressure, smectite-to-illite) control the onset of seismogenic behavior on subduction thrust faults (Hirose *et al.*, 2013).

Future work on permeability for deeper samples from Hole C0002P should be conducted by other scientists. The complete clay-size fraction XRD analysis through the entire drilling interval will also contribute more to constrain clay digenesis and clay provenance. Moreover, the next IODP NanTroSEIZE expedition will drill deeper into the interior of Nankai accretionary prism. Sampling across the megasplay at seismogenic depths will improve the understanding of processes that govern the strength, nature and distribution of slip along the plate boundary fault system, in order to evaluate earthquake and tsunami hazards.

References cited

Anandarajah, A., and Kuganenthira, N., 1995. Some aspects of fabric anisotropy of soil. *Geotechnique*, 45: 69-81.

Ando, M., 1975. Source mechanisms and tectonic significance of historical earthquakes along the Nankai Trough, Japan. *Tectonophysics,* 27(2):119–140.

Aplin, A.C., Matenaar, I.F., McCarty, D.K., and van der Pluijm, B.A., 2006. Influence of mechanical compaction and clay mineral diagenesis on the microfabric and pore-scale properties of deep-water Gulf of Mexico mudstones. *Clays Clay Miner.*, 54(4):500–514.

Altaner, S.P., and Ylagan, R.F., 1997. Comparison of structural models of mixed-layer illite/smectite and reaction mechanisms of smectite illitization. *Clays Clay Miner., 45*(4): 517-533.

Anma, R., Ogawa, Y., Moore, G.F., Kawamura, K., Sasaki, T., Kawakami, S., Dilek, Y., Michiguchi, Y., Endo, R., Akaiwa, S., and Hirano, S., 2011. Structural profile and development of the accretionary complex in the Nankai Trough, Southwest Japan: results of submersible studies. *In* Ogawa, Y., Anma, R., and Dilek, Y. (Eds.), *Accretionary Prisms and Convergent Margin Tectonics in the Northwest Pacific Basin*, 8: Springer Netherlands, 169-196.

Ashi, J., Lallemant, S., Masago, H., and the Expedition 315 Scientists, 2009. Expedition 315 summary. *In* Kinoshita, M., Tobin, H., Ashi, J., Kimura, G., Lallemant, S., Screaton, E.J., Curewitz, D., Masago, H., Moe, K.T., and the Expedition 314/315/316 Scientists, *Proc. IODP*, 314/315/316: Washington, DC (Integrated Ocean Drilling Program Management International, Inc.).

Baba, T., and Cummins, P.R., 2005. Contiguous rupture areas of two Nankai Trough earthquakes revealed by high-resolution tsunami waveform inversion. *Geophys. Res. Lett.*, 32(8): L08305.

Bangs, N., Shipley, T.H., Gulick, S.P.S., Moore, G.F., Kuramoto, S., and Nakamura, Y., 2004. Evolution of the Nankai Trough décollement zone from the trench into the seismogenic zone: Inferences from 3-D seismic reflection imaging. *Geology*, 32: 273-276.

Beall, A.O., and Fischer, A.G., 1969. Sedimentology. *In* Ewing, M., Worzel, J.L., *et al.*, Sedimentology. *Init. Repts. DSDP*, 1: Washington (U.S. Govt. Printing Office), 521-593.

Bennett, R.H., O'Brien, N.R., and Hulbert, M.H., 1991. Determinants of clay and shale microfabric signatures: Processes and mechanisms. *In* Bennett, R.H., Bryant, W.R., and Hulbert, M.H. (Eds.), *Microstructure of Fine-Grained Sediments: From Mud to Shale*: New York, Springer-Verlag, 5-32.

Bilek, S.L., and Lay, T., 2002. Tsunami earthquakes possibly widespread manifestations of frictional conditional stability. *Geophys. Res. Lett.*, 29(14): 18-1-18-4.

Biscaye, P.E., 1965. Mineralogy and sedimentation of recent deep-sea clay in the Atlantic Ocean and adjacent seas and oceans. *Geol. Soc. Am. Bull.*, 76(7): 803-831.

Bloomer, S.H., Taylor, B., MacLeod, C.J., Stern, R.J., Fryer, P., Hawkins, J.W., and Johnson, L., 1995. Early arc volcanism and the ophiolite problem: a perspective from drilling in the western Pacific. In Taylor, B., and Natland, J. (Eds.), *Active margins and marginal basins of the western Pacific*: American Geophysical Union, Washington, D.C., 1-30.

Bolton, A.J., Maltman, A. J., and Fisher, Q.,2000. Anisotropic permeability and bimodal pore-size distributions of fine-grained marine sediments. *Mar. Petrol. Geol.*, 17(6): 657-672.

Bourlange, S., Jouniaux, L., and Henry, P., 2004. Data report: Permeability, compressibility, and friction coefficient measurements under confining pressure and strain, Leg 190, Nankai Trough. *In* Mikada, H., Moore, G.F., Taira, A., Becker, K., Moore, J.C., and Klaus, A. (Eds.), *Proc. ODP, Sci. Results*,190/196: College Station, TX (Ocean Drilling Program), 1–16.

Boutt, D.F., Saffer, D., Doan, M., Lin, W., Ito, T., Kano, Y., Flemings, P., McNeill, L.C., Byme, T., Hayman, N.W., and Moe, K.T., 2012. Scale dependence of in-situ permeability measurements in the Nankai accretionary prism: The role of fractures. *Geophys. Res. Lett.*, 39: L07302.

Buchs, D.M., Cukur, D., Masago, H., and Garbe-Schönberg, D., 2015. Sediment flow routing during formation of forearc basins: constraints from integrated analysis of detrital pyroxenes and stratigraphy in the Kumano Basin, Japan. *Earth Planet. Sci. Lett.*, 414: 164-175.

Burst, J.F., 1957. Postdiagenetic clay mineral environmental relationships in the Gulf Coast Eocene1. *Clays Clay Miner.*, 6: 327-341.

Burst, J.F., 1969. Diagenesis of Gulf Coast clayey sediments and its possible relation to petroleum migration. *AAPG Bull.*, 53(1): 73-93.

Brown, K.M., and Ransom, B., 1996. Porosity correction for smectite-rich sediments: impact on studies of compaction, fluid generation, and tectonic history. *Geology*, 24: 843-846.

Bryant, W.R., Bennett, R., and Katherman, C., 1981. Shear strength, consolidation, porosity, and permeability of oceanic sediments. *In* Emiliani, C. (Ed.), *The Sea*, 7: New York (Wiley), 1555-1616.

Cambray, H., Pubellier, M., Jolivet, L., and Pouclet, A., 1995. Volcanic activity recorded in deep-sea sediments and the geodynamic evolution of western Pacific island arcs. *In* Taylor, B., and Natland, J. (Eds), *Active Margins and Marginal Basins of the Western Pacific*: American Geophysical Union, Washington, D.C., 97-124.

Chamley, H., 1980. Clay sedimentation and paleoenvironment in the Shikoku Basin since the middle Miocene (Deep Sea Drilling Project Leg 58, North Philippine Sea). *In* Klein, G.D., Kobayashi, K., *et al.*, *Init. Repts. DSDP*, 58: Washington, D.C. (U.S. Government Printing Office), 669-678.

Chamley, H., 1989. *Clay sedimentology*: Springer-Verlag, Berlin, 549.

Chamot-Rooke, N., Renard, V., and Le Pichon, X., 1987. Magnetic anomalies in the Shikoku basin: A new interpretation. *Earth Planet. Sci. Lett.*, 3: 214-228.

Clennel, M.B., Dewhurst, D.N., Brown, K.M., and Westbrool, G.K., 1999. Permeability anisotropy of consolidated clays. *In* Aplin, A.C., Fleet, A.J., and Macquaker, J.H.S. (Eds.), *Muds and Mudstone:Physical and Fluid Flow Properties*, 158: Geological Society, London, Special Publication, 79-96.

Clift, P.D., Carter, A., Nicholson, U., and Masago, H., 2013. Zircon and apatite thermochronology of the Nankai Trough accretionary prism and trench, Japan: Sediment transport in an active and collisional margin setting. *Tectonics*, 32: 377-395.

Colten-Bradley, V.A., 1987. Role of pressure in smectite dehydration--effects on geopressure and smectite-to-illite transformation. *AAPG Bull.*, 71(11): 1414-1427.

Coulbourn, W.T., 1986. Introduction and summary of active-margin drilling in the Nankai Trough and Japan trench, deep sea drilling project Leg 87. *In* Kagami, H., Karig, D.E., Coulbourn, W.T., *et al., Init. Repts. DSDP*, 87: Wahsington D.C. (U.S. Goverrntment Printing Office), 5-18.

Cummins, P.R., Hori, T., and Kaneda, Y., 2001. Splay fault and megathrust earthquake slip in the Nankai Trough. *Earth, Planets Space*, (53): 243-248.

Daigle, H., and Dugan, B., 2014. Data report: permeability, consolidation, stress state, and pore system characteristics of sediments from Sites C0011, C0012, and C0018 of the Nankai Trough. *In* Henry, P., Kanamatsu, T., Moe, K., and the Expedition 333 Scientists, *Proc. IODP*, 333: Tokyo (Integrated Ocean Drilling Program Management International, Inc.).

deVries Klein,G., Kobayashi, K., *et al.*, 1980. *Init. Repts. DSDP*, 58: Washington D.C. (U.S. Government Printing Office).

Dewhurst, D.N., Aplin, A.C., and Sarda, J., 1999. Influence of clay fraction on pore-scale properties and hydraulic conductivity of experimentally compacted mudstones. *J. Geophys. Res.*, 104(B12): 29,261-229,274.

Dugan, B., and Daigle, H., 2011. Data report: permeability, compressibility, stress state, and grain size of shallow sediments from Sites C0004, C0006, C0007, and C0008 of the Nankai accretionary complex. *In* Kinoshita, M., Tobin, H., Ashi, J., Kimura, G., Lallemant, S., Screaton, E.J., Curewitz, D., Masago, H., Moe, K.T., and the Expedition 314/315/316 Scientists, *Proc. IODP*, 314/315/316: Tokyo (Integrated Ocean Drilling Program Management International, Inc.).

Dugan, B., and Zhao, X., 2013. Data report: permeability of sediments from Sites C0011 and C0012, NanTroSEIZE Stage 2: subduction inputs. *In* Saito, S., Underwood, M.B., Kubo, Y., and the Expedition 322 Scientists, *Proc. IODP*, 322: Tokyo (Integrated Ocean Drilling Program Management International, Inc.).

Ekinci, M.K., Likos, W.J., Underwood, M.B., and Guo, J., 2011. Data report: permeability of mud(stone) samples from IODP Sites C0006 and C0007, Nankai Trough Seismogenic Zone Experiment. *In* Kinoshita, M., Tobin, H., Ashi, J., Kimura, G., Lallemant, S., Screaton, E.J.,

Curewitz, D., Masago, H., Moe, K.T., and the Expedition 314/ 315/316 Scientists, *Proc. IODP*, 314/315/316: Washington, D.C. (Integrated Ocean Drilling Program Management International, Inc.).

Expedition 315 Scientists, 2009. Expedition 315 Site C0002. *In* Kinoshita, M., Tobin, H., Ashi, J., Kimura, G., Lallemant, S., Screaton, E.J., Curewitz, D., Masago, H., Moe, K.T., and the Expedition 314/315/316 Scientists, *Proc. IODP,* 314/315/316: Washington, D.C. (Integrated Ocean Drilling Program Management International, Inc.).

Expedition 319 Scientists, 2010. Expedition 319 summary. *In* Saffer, D., McNeill, L., Byrne, T., Araki, E., Toczko, S., Eguchi, N., Takahashi, K., and the Expedition 319 Scientists, *Proc. IODP,* 319: Tokyo (Integrated Ocean Drilling Program Management International, Inc.).

Expedition 319 Scientists, 2010b. Site C0009. *In* Saffer, D., McNeill, L., Byrne, T., Araki, E., Toczko, S., Eguchi, N., Takahashi, K., and the Expedition 319 Scientists, *Proc. IODP*, 319: Tokyo (Integrated Ocean Drilling Program Management International, Inc.).

Expedition 326 Scientists, 2011. NanTroSEIZE Stage 3: plate boundary deep riser: top hole engineering. *IODP Prel. Rept.,* 326.

Expedition 332 Scientists, 2011. Expedition 332 summary. *In* Kopf, A., Araki, E., Toczko, S., and the Expedition 332 Scientists, *Proc. IODP,* 332: Tokyo (Integrated Ocean Drilling Program Management International, Inc.).

Expedition 333 Scientists, 2012. Expedition 333 summary. *In* Henry, P., Kanamatsu, T., Moe, K., and the Expedition 333 Scientists, *Proc. IODP,* 333: Tokyo (Integrated Ocean Drilling Program Management International, Inc.).

Expedition 333 Scientists, 2012b. Site C0018. *In* Henry, P., Kanamatsu, T., Moe, K., and the Expedition 333 Scientists, *Proc. IODP,* 333: Tokyo (Integrated Ocean Drilling Program Management International, Inc.).

Expedition 338 Scientists, 2014. Expedition 338 summary. *In* Strasser, M., Dugan, B., Kanagawa, K., Moore, G.F., Toczko, S., Maeda, L., and the Expedition 338 Scientists, *Proc. IODP,* 338: Yokohama (Integrated Ocean Drilling Program).

Expedition 338 Scientists, 2014b. Site C0002. *In* Strasser, M., Dugan, B., Kanagawa, K., Moore, G.F., Toczko, S., Maeda, L., and the Expedition 338 Scientists, *Proc. IODP,* 338: Yokohama (Integrated Ocean Drilling Program).

Expedition 348 Scientists and Scientific Participants, 2014. NanTroSEIZE Stage 3: NanTroSEIZE plate boundary deep riser 3. *IODP Prel. Rept.*, 348.

Expedition 348 Scientists, 2015. Expedition 348 summary. *In* Tobin, H., Hirose, T., Saffer, D., Toczko, S., Maeda, L., Kubo, Y., and the Expedition 348 Scientists, *Proc. IODP,* 348: College Station, TX (Integrated Ocean Drilling Program).

Expedition 348 Scientists, 2015a. Methods. *In* Tobin, H., Hirose, T., Saffer, D., Toczko, S., Maeda, L., Kubo, Y., and the Expedition 348 Scientists, 2015. *Proc. IODP,* 348: College Station, TX (Integrated Ocean Drilling Program).

Expedition 348 Scientists, 2015b. Site C0002. *In* Tobin, H., Hirose, T., Saffer, D., Toczko, S., Maeda, L., Kubo, Y., and the Expedition 348 Scientists, *Proc. IODP,* 348: College Station, TX (Integrated Ocean Drilling Program).

Fagel, N., Robert, C., Preda, M., and Thorez, J., 2001. Smectite composition as a tracer of deep circulation: the case of the Northern North Atlantic. *Mar. Geol.,* (172): 309-330.

Fergusson, C.L., 2003. Provenance of Miocene-Pleistocene turbidite sands and sandstones, Nankai Trough, Ocean Drilling Program Leg 190. *In* Mikada, H., Moore, G.F., Taira, A., Becker, K., Moore, J.C., and Klaus, A. (Eds.), *Proc. ODP, Sci. Results,* 190/196: College Station, TX (Ocean Drilling Program), 1-28.

Fisher, A.T. and Underwood, M.B., 1995. Calibration of an x-ray diffraction method to determine relative mineral abundances in bulk powders using matrix singular value decomposition A test from the Barbados accretionary complex. *In* Shipley, T.H., Ogawa, Y., Blum, P., *et al., Proc. ODP, Init Repts.*, 156: College Station, TX (Ocean Drilling Program), 29-37.

Folk, R.L., and Ward, W.C., 1957, Brazos River Bar: A study in the significance of grain size parameters. *J. Sed. Petrol.,* 27 (1): 3-26.

Freed, R.L., and Peacor, D.R., 1989. Variability in temperature of the smectite/illite reaction in Gulf Coast sediments. *Clay Miner.,* (24): 171-180.

Futagami, T., Morono, Y., Terada, T., Kaksonen, A. H., and Inagaki, F., 2013. Distribution of dehalogenation activity in subseafloor sediments of the Nankai Trough subduction zone. *Phil. Trans. R. Soc. B.*, 368(1616): 1-15.

Gamage, K., Screaton, E., Bekins, B., and Aiello, I., 2011. Permeability–porosity relationships of subduction zone sediments. *Mar. Geol.*, 279(1–4):19–36.

Gingele, F.X., Deckker, P.D., and Hillenbrand, C., 2001b. Clay mineral distribution in surface sediments between Indonesia and NW Australia - source and transport by ocean currents. *Mar. Geol.*, (179): 135-146.

Goldstein, J., Newbury, D.E., Joy, D.C., Lyman, C.E., Echlin, P., LIfshin, E., Sawyer, L., and Michael, J.R., 2003. *Scanning Electron Microscopy and X-ray Microanalysis* (3 ed): Springer.

Gulick, S. P. S., Bangs, N. L.B., Moore, G.F., Ashi, J., Martin, K.M., Sawyer, D.S., Tobin, H.J., Kuramoto, S., and Taira, A., 2010. Rapid forearc basin uplift and megasplay fault development from 3D seismic images of Nankai Margin off Kii Peninsula, *Jpn. Earth Planet. Sci. Lett.*, 300(1-2): 55-62.

Guo, J. and Underwood, M.B., 2011b. Data report: refined method for calculating percentages of kaolinite and chlorite from X-ray diffraction data, with application to the Nankai margin of

southwest Japan. *In* Kinoshita, M., Tobin, H., Ashi, J., Kimura, G., Lallemant, S., Screaton, E.J., Curewitz, D., Masago, H., Moe, K.T., and the Expedition 314/315/316 Scientists, *Proc. IODP*, 314/315/316: Washington, D.C. (Integrated Ocean Drilling Program Management International, Inc.).

Guo, J., Likos, W.J., Underwood, M.B., Skarbek, R.M., Adamson, N., and Saffer, D., 2011. Data report: consolidation characteristics of sediments from Sites C0002, C0006, and C0007, IODP Expeditions 315 and 316, NanTroSEIZE Stage 1. *In* Kinoshita, M., Tobin, H., Ashi, J., Kimura, G., Lallemant, S., Screaton, E.J., Curewitz, D., Masago, H., Moe, K.T., and the Expedition 314/315/316 Scientists, *Proc. IODP*, 314/315/316: Washington, D.C. (Integrated Ocean Drilling Program Management International, Inc.).

Guo, J., and Underwood, M.B., 2012. Data report: clay mineral assemblages from the Nankai Trough accretionary prism and the Kumano Basin, IODP Expeditions 315 and 316, NanTroSEIZE Stage 1. *In* Kinoshita, M., Tobin, H., Ashi, J., Kimura, G., Lallemant, S., Screaton, E.J., Curewitz, D., Masago, H., Moe, K.T., and the Expedition 314/315/316 Scientists, *Proc. IODP*, 314/315/316: Washington, D.C. (Integrated Ocean Drilling Program Management International, Inc.).

Guo, J., and Underwood, M.B., 2014. Data report: consolidation and permeability of sediments from Sites C0011, C0012, and C0018, IODP Expeditions 322 and 333, NanTroSEIZE Stage 2. *In* Saito, S., Underwood, M.B., Kubo, Y., and the Expedition 322 Scientists, *Proc. IODP*, 322: Tokyo (Integrated Ocean Drilling Program Management International, Inc.).

Hamamoto, H., Yamano, M., Goto, S., Kinoshita, M., Fujino, K., and Wang, K., 2011. Heat flow distribution and thermal structure of the Nankai Subduction zone off the Kii Peninsula. *Geochem., Geophys., Geosyst.*, 12(10): 1-22.

Harris, R. N., Schmidt-Schierhorn, F., and Spinelli, G., 2011. Heat flow along the NanTroSEIZE transect: Results from IODP Expeditions 315 and 316 offshore the Kii Peninsula, Japan. *Geochem., Geophys., Geosyst.*, 12(8): 1-18.

Hirose, T., Saffer, D.M., Tobin, H.J., Toczko, S., Maeda, L., Kubo, Y., Kimura, G., Moore, G.F., Underwood, M.B., and Kanagawa, K., 2013. NanTroSEIZE Stage 3: NanTroSEIZE plate boundary deep riser 3. *IODP Sci. Prosp.*, 348.

Hodder, A.P.W., Naish, T.R., and Nelson, C.S., 1993. A two-stage model for the formation of smectite from detrital volcanic glass under shallow-marine conditions. *Mar. Geol.*, 109: 279-285.

Hower, J., Eslinger, E.V., Hower, M.E., and Perry, E.A., 1976. Mechanism of burial metamorphism of argillaceous sediment: 1. Mineralogical and chemical evidence. *Geol. Soc. Am. Bull.*, 87: 725-737.

Hüpers, A., and Kopf, A.J., 2012. Data report: consolidation properties of silty claystones and sandstones sampled seaward of the Nankai Trough subduction zone, IODP Sites C0011 and C0012. *In* Saito, S., Underwood, M.B., Kubo, Y., and the Expedition 322 Scientists, *Proc. IODP*, 322: Tokyo (Integrated Ocean Drilling Program Management International, Inc.).

Huang, W.-L., Longo, J.M., and Pevear, D.R., 1993. An experimentally derived kinetic model for smectite-to-illite conversion and its use as a geothermometer. *Clays Clay Miner.*, 41: 162-177.

Hubbert, M.K., and Rubey, W.W., 1959. Role of fluid pressure in mechanics of overthrust faulting I. Mechanics of fluid-filled porous solids and its application to overthrust faulting. *Geol. Soc. Am. Bull.*, 70(2): 115-166.

Hyndman, R.D., Yamano, M., and Oleskevich, D.A., 1997. The seismogenic zone of subduction thrust faults. *Isl. Arc*, (6): 244-260.

Ichinose, G.A., Thio, H.K., Somerville, P.G., Sato, T. and Ishii, T., 2003. Rupture process of the 1944 Tonankai earthquake (M_s 8.1) from the inversion of teleseismic and regional seismograms. *J. Geophys. Res., [Solid Earth]*, 108(B10): 13-1-13-21.

Ike, T., Moore, G.F., Kuramoto, S., Park, J., Kaneda, Y., and Taira, A., 2008. Variations in sediment thickness and type along the northern Philippine Sea Plate at the Nankai Trough. *Isl. Arc*, 17(3): 342-357.

Ingle, J. C., Karig, D.E., and White, S.M., 1975. Introduction and explanatory notes. *In* Karig, D.E., Ingle, J.C., Jr., *et al.*, *Init. Repts. DSDP*, 31: Washington D.C. (U.S. Government Printing Office), 31: 5-21.

Ishii, T., Sato, H., and Machida, S., *et al.*, 2000. Geological and petrological studies of the Kinan and Izu-Ogasawara-backarc-echelon seamount Chains. *Bull. Geol. Surv. Jpn.*, 51: 615-630.

Ito, Y., and Obara, K., 2006. Very low frequency earthquakes within accretionary prisms are very low stress-drop earthquakes. *Geophys. Res. Lett.*, 33(9): L09302.

Kagami, H., *et al.*, 1986. *Init. Repts. DSDP*, 87: Washington, D.C. (U.S. Government Printing Office).

Karig, D.E., 1971. Origin and development of marginal basins in the western Pacific. *J. Geophys. Res.*, 76(11): 2542-2561.

Karig, D.E., *et al*, 1975. *Init. Repts. DSDP*, 31: Washington, D.C. (U.S. Government Printing Office).

Karig, D.E., and Angevine, C.L., 1985. Geologic constraints on subduction rates in the Nankai Trough. *In* Kagami H., Karig, D.E., and Coulbourn, W.T., (Eds.). *Proc. DSDP, Init. Repts*, 87: Washington, D.C. (U.S. Government Printing Office), 789-796.

Kim, J.-W., Bryant, W.R., Watkins, J.S., and Tieh, T.T., 1999. Electron microscopic observations of shale diagenesis, offshore Louisiana, USA, Gulf of Mexico. *Geo-Mar. Lett.*, 18(3): 234–240.

Kimura, G., Kitamura, Y., Hashimoto, Y., Yamaguchi, A., Shibata, T., Ujiie, K., and Okamoto, S., 2007. Transition of accretionary wedge structures around the up-dip limit of the seismogenic subduction zone. *Earth Planet. Sci. Lett.*, 255(3-4): 471-484.

Kimura, G., Moore, G.F., Strasser, M., Screaton, E., Curewitz, D., Streiff, C., and Tobin, H., 2011. Spatial and temporal evolution of the megasplay fault in the Nankai Trough. *Geochem., Geophys., Geosyst.*, 12(3): 1-23.

Kimura, G., Hashimoto, Y., Kitamura, Y., Yamaguchi, A., and Koge, H., 2014. Middle Miocene swift migration of the TTT triple junction and rapid crustal growth in southwest Japan: A review. *Tectonics,* 33(7): 1219-1238.

Kimura, J.-I., Stern, R.J., Yoshida, T., 2005. Reinitiation of subduction and magmatic responses in SW Japan during Neogene time. *Geol. Soc. Am. Bull.*, 117(7): 969-986.

Kimura, J.-I., Gill, J.B., Kunikiyo, T., Osaka, I., Shimoshioiri, Y., Katakuse, M., Kakubuchi, S., Nagao, T., Furuyama, K., Kamei, A., Kawabata, H., Nakajima, J., Keken, P E., and Stern, R.J., 2014. Diverse magmatic effects of subducting a hot slab in SW Japan: Results from forward modeling. *Geochem., Geophys., Geosyst.,* (15): 691-739.

Kinoshita, M., Tobin, H., Eguchi, N., and Nielsen, S., 2010. NanTroSEIZE Stage 3: plate Boundary deep riser: top hole engineering. *IODP Sci. Prosp.*, 326.

Kinoshita, M., and Yamano, M., 1995. Heat flow distribution in the Nankai Trough region. *In* Tokuyama H. *et al.*, (Eds.). *Geology and Geophysics of the Philippine Sea*: Terra Scientific Publishing, Company (TERRAPUB), Tokyo: 77-86.

Kitazato, H., 1997. Paleogeographic changes in central Honshu, Japan, during the late Cenozoic in relation to the collision of the Izu-Ogasawara Arc with the Honshu Arc. *Isl. Arc*, *6*(2): 144-157.

Kobayashi, K., Kasuga, K., and Okino, K., 1995. Shikoku basin and its margins. *In* Taylor, B., (ed.). *Backarc Basins: Tectonics and Magmatism*: 381-405. Plenum Press, New York, NY.

Kobayashi, K., and Nakada, M., 1978. Magnetic anomalies and tectonic evolution of the Shikoku inter-arc basin, in Geodynamics of the Western Pacific. *J. Phys. Earth*, 26: 391-402.

Kopf, A., Araki, E., Toczko, S., and the Expedition 332 Scientists, 2011. *Proc. IODP,* 332: Tokyo (Integrated Ocean Drilling Program Management International, Inc.).

Kopf, A., Strasser, M., Monsees, N., Underwood, M.B., and Guo, J., 2011. Data report: particle size analysis of sediments recovered during IODP Expeditions 315 and 316, Sites C0001–C0008, Nankai Trough forearc, off Japan. *In* Kinoshita, M., Tobin, H., Ashi, J., Kimura, G., Lallemant, S., Screaton, E.J., Curewitz, D., Masago, H., Moe, K.T., and the Expedition 314/315/316 Scientists, *Proc. IODP*, 314/315/316: Washington, DC (Integrated Ocean Drilling Program Management International, Inc.).

Kübler, B., and Jaboyedoff, M., 2000. Illite crystallinity. *Earth Planet. Sci. Lett.*, (331): 75-89.

Lanson, B., Sakharov, B.A., Claret, F., and Drits, V.A., 2009. Diagenetic smectite-to-illite transition in clay-rich sediments: A reappraisal of X-ray diffraction results using the multi-specimen method. *Am. J. Sci.*, 309(6): 476-516.

Le Pichon, X., and Henry, P., 1992. Erosion and accretion along subduction zones: a model of evolution. *Proceedings of the Koninklijke Nederlandse Akademie van Wetenschappen*, 95(3): 297-310.

Love, L.G., and Amstutz, G.C., 1966. Review of microscopic pyrite from the Devonian Chattanooga shale and Rammelsberg Banderz. *Fortschr. Miner.*, 43(2): 273-309.

Mahony, S.H., Wallace, L.M., Miyoshi, M., Villamor, P., Sparks, R.S.J., and Hasenaka, T., 2011. Volcano-tectonic interactions during rapid plate-boundary evolution in the Kyushu region, SW Japan. *Geol. Soc. Am. Bull.*, 123(11-12): 2201-2223.

Martin, V., Lallemant, S., Henry, P., Dessa, J., Noble, M. S., Operto, S., Pascal, G., Kuramoto, S., and Tokuyama, H., 2004. Eastern Nankai margin structure and history of accretion. *Geology*: 1-14.

Masuda, H., Peacor, D. R., and Dong, H., 2011. Transmission electron microscopy study of conversion of smectite to illite in mudstones of the Nankai Trough: Contrast with coeval bentonites. *Clays Clay Miner.*, 49(2): 109-118.

McManus, D.A., 1991. Suggestions for authors whose manuscripts include quantitative clay mineral analysis by X-ray diffraction. *Mar. Geol.*, 98(1): 1-5.

Mikada, H., Becker, K., Moore, J.C., Klaus, A., *et al.*, 2002. *Proc. ODP, Init. Repts.*, 196: College Station, TX (Ocean Drilling Program).

Miyazaki, S., and Heki, K., 2001. Crustal velocity field of southwest Japan: Subduction and arc-arc collision. *J. Geophys. Res.*, 106: 4305-4326.

Moon, C.F., and Hurst, C.W., 1984. Fabric of muds and shales: an overview. *In* Stow, D.A.V., and Piper, D.J.W. (Eds.), *Fine-Grained Sediments: Deep-Water Processes and Facies*, 15(1): Geological Society, London, Special Publications, 579-593.

Moore, C.A., 1968. Quantitative analysis of naturally occurring multicomponent mineral systems by X-ray diffraction. *Clays Clay Miner.*, 16: 325-336.

Moore, D.M., and Reynolds, R.C., Jr., 1989. *X-ray diffraction and the identification and analysis of clay minerals*: Oxford (Oxford Univ. Press).

Moore, G.F., Bangs, N.L., Taira, A., Kuramoto, S., Pangborn, E., and Tobin, H.J., 2007. Three-dimensional splay fault geometry and implications for tsunami generation. *Science*, 318(5853):1128–1131.

Moore, G.F., and Moore, J.C., 1998. Final Report. *The seismogenic zone experiment (SEIZE) workshop*: June 3-6, 1997, Waikoloa, Hawaii.

Moore, G.F., Park, J.-O., Bangs, N.L., Gulick, S.P., Tobin, H.J., Nakamura, Y., Saito, S., Tsuji, T., Yoro, T., Tanaka, H., Uraki, S., Kido, Y., Sanada, Y., Kuramoto, S., and Taira, A., 2009. Structural and seismic stratigraphic framework of the NanTroSEIZE Stage 1 transect. *In*

Kinoshita, M., Tobin, H., Ashi, J., Kimura, G., Lallemant, S., Screaton, E.J., Curewitz, D., Masago, H., Moe, K.T., and the Expedition 314/315/316 Scientists, *Proc. IODP*, 314/315/316: Washington, DC (Integrated Ocean Drilling Program Management International, Inc.).

Moore, G.F., Taira, A., Klaus, A., Becker, L., Boeckel, B., Cragg, B.A., Dean, A., Fergusson, C.L., Henry, P., Hirano, S., Hisamitsu, T., Hunze, S., Kastner, M., Maltman, A.J., Morgan, J.K., Murakami, Y., Saffer, D.M., Sanchez-Gomez, M., Screaton, E.J., Smith, D.C., Spivack, A.J., Steurer, J., Tobin, H.J., Ujiie, K., Underwood, M.B., and Wilson, M., 2001c. New insights into deformation and fluid flow processes in the Nankai Trough accretionary prism: Results of Ocean Drilling Program Leg 190. *Geochem., Geophys., Geosyst.*, 2(10): 129-200.

Moore, J.C., 1989. Tectonics and hydrogeology of accretionary prisms: role of the décollement zone. *J. Struct. Geol.*, 11(1): 95-106.

Moore, J.C., Barrett, M., and Thu, M.K., 2012. High fluid pressures and high fluid flow rates in the Megasplay Fault Zone, NanTroSEIZE Kumano Transect, SW Japan. *Geochem., Geophys., Geosyst.*, 13(8).

Moore. J.C., and Saffer, D., 2001. Updip limit of the seismogenic zone beneath the accretionary prism of SW Japan: An effect of diagenetic to low-grade metamorphic processes and increasing effective stress. *Geology*, 29: 183-186.

Moore, J.C., and Vrolijk, P., 1992. Fluids in accretionary prisms. *Rev. Geophys.*, 30: 113-135.

Morita, S., Ashi, J., Aoike, K., and Kuramoto, S.I., 2004. Evolution of Kumano Basin and sources of clastic ejecta and pore fluid in Kumano mud volcanoes, Eastern Nankai Trough. *Proceedings of the International Symposium on Methane Hydrates and Fluid Flow in Upper Accretionary Prisms*: 92-99.

Morley, C.K., 2009. Growth of folds in a deep-water setting. *Geosphere*, 5(2):59–89.

Moros, M., McManus, J.F., Rasmussen, T., Kuijpers, A., Dokken, T., Snowball, I., Nielsen, T., and Jansen, E., 2004. Quartz content and the quartz-to-plagioclase ratio determined by X-ray diffraction: a proxy for ice rafting in the northern North Atlantic?. *Earth Planet. Sci. Lett.*, 218(3): 389-401.

Nakamura, K., Shimazaki, K., and Yonekura, N., 1984. Subduction, bending and education, Present and Quaternary tectonics of the northern border of the Philippine Sea Plate. *Bulletin de la Société Géologique de France*, 26: 221-243.

Nakanishi, A., Takahashi, N., Park, J.-O., Miura, S., Kodaira, S., Kaneda, Y., Hirata, N., Iwasaki, T., and Nakamura, M., 2002. Crustal structure across the coseismic rupture zone of the 1944 Tonankai earthquake, the central Nankai Trough seismogenic zone. *J. Geophys. Res., [Solid Earth]*, 107(B1):2007.

Neuzil, C.E., 1994. How permeable are clays and shales? *Water resources research*, 30(2): 145-150.

Noiriel, C., Gouze, P., and Bernard, D., 2004. Investigation of porosity and permeability effects from microstructure changes during limestone dissolution. *Geophys. Res. Lett.*, 31(24): L24603.

Obana, K., and Kodaira, S., 2009. Low-frequency tremors associated with reverse faults in a shallow accretionary prism. *Earth Planet. Sci. Lett.*, 287(1–2):168–174.

Ogawa, Y., Anma, R., and Dilek, Y. (Eds.), 2011. *Accretionary prisms and convergent margin tectonics in the Northwest Pacific Basin*, 8: Springer Science & Business Media.

Ohmori, K., Taira, A., Tokuyama, H., Sagaguchi, A., Okamura, M., and Aihara, A., 1997. Paleothermal structure of the Shimanto accretionary prism, Shikoku, Japan: Role of an out-of-sequence thrust. *Geology*, 25: 327–330.

Okino, K., Ohara, Y., Kasuga, S., and Kato, Y., 1999. The Philippine Sea: New survey results reveal the structure and the history of the marginal basins. *Geophys. Res. Lett.*, 26: 2287-2290.

Okino, K., Shimakawa, Y., and Nagaoka, S., 1994. Evolution of the Shikoku Basin. *J. Geomag. Geoel.*, 46: 463-479.

Otofuji, Y.I., Nishizawa, Y., Tamai, M., and Matsuda, T., 1997. Palaeomagnetic and chronological study of Miocene welded tuffs in the northern part of Central Japan: tectonic implications for the latest stage of arc formation of Japan. *Tectonophysics*, 283(1): 263-278.

Ottner, F., Gier, S., Kuderna, M., and Schwaighofer, B., 2000. Results of an inter-laboratory comparison of methods for quantitative clay analysis. *Appl. Clay Sci.*, 17(5-6): 223-243.

Park, J.-O., Tsuru, T., Kodaira, S., Cummins, P.R., and Kaneda, Y., 2002. Splay fault branching along the Nankai subduction zone, *Science*, 297: 1157-1160.

Perry, E.A., and Hower, J., 1970. Burial diagenesis in Gulf Coast pelitic sediments *Clays Clay Miner.*, 18: 165-177.

Petschick, R., Kuhn, G., and Gingele, F., 1996. Clay mineral distribution in surface sediments of the South Atlantic: sources, transport, and relation to oceanography. *Mar. Geol.*, 130(3-4): 203-229.

Phillips, S.C., Johnson, J.E., Underwood, M.B., Guo, J., Giosan, L., and Rose, K., 2014. Long-timescale variation in bulk and clay mineral composition of Indian continental margin sediments in the Bay of Bengal, Arabian Sea, and Andaman Sea. *Mar. Petrol. Geol.*, 58: 1-22.

Pickering, K.T., Underwood, M.B., Saito, S., Naruse, H., Kutterolf, S., Scudder, R., Park, J.-O., Moore, G.F., and Slagle, A., 2013. Depositional architecture, provenance, and tectonic/eustatic modulation of Miocene submarine fans in the Shikoku Basin: Results fromNankai Trough Seismogenic Zone Experiment. *Geochem., Geophys., Geosyst.*, 14(6): 1722-1739.

Powers, M.C., 1957. Adjustment of clays to chemical change and the concept of the equivalence level. *Clays Clay Miner.*, 6: 309-326.

Rettke, R.C., 1981. Probable burial diagenetic and provenance effects on Dakota group clay mineralogy, Denver Basin. *J. Sed. Petrol.*, 51(2): 541-551.

Reynolds, R.C., and Hower, J., 1970. The nature of interlayering in mixed-layer illite/montmorillonites. *Clays Clay Miner.*, (18): 25-36.

Rowe, K.T., Screaton, E.J., & Ge, S., 2012. Coupled fluid flow and deformation modeling of the frontal thrust region of the Kumano Basin transect, Japan: Implications for fluid pressures and decollement downstepping. *Geochem., Geophys., Geosyst.*, 13(3): 1-18.

Rowe, K.T., Screaton, E.J., and Underwood, M.B., 2011. Data report: permeabilities of sediments from the Kumano Basin transect off Kii Peninsula, Japan. *In* Kinoshita, M., Tobin, H., Ashi, J., Kimura, G., Lallemant, S., Screaton, E.J., Curewitz, D., Masago, H., Moe, K.T., and the Expedition 314/315/316: Washington, D.C. (Integrated Ocean Drilling Program Management International, Inc.).

Saffer, D.M., 2010. Hydrostratigraphy as a control on subduction zone mechanics through its effects on drainage: an example from the Nankai Margin, SW Japan. *Geofluids*, (10): 114-131.

Saffer, D.M., 2015. The permeability of active subduction plate boundary faults. *Geofluids*, 15: 193-215.

Saffer, D.M., and Bekins, B.A., 1998. Episodic fluid flow in the Nankai accretionary complex: Timescale, geochemistry, flow rates, and fluid budget. *J. Geophys. Res.*, 103(B12): 30,351-330,370.

Saffer, D.M., Lockner, D.A., and McKiernan, A., 2012. Effects of smectite to illite transformation on the frictional strength and sliding stability of intact marine mudstones. *Geophys. Res. Lett.*, 39: 1-6.

Saffer, D.M., and Marone, C., 2003. Comparison of smectite- and illite rich gouge frictional properties: Application to the up-did limit of the seismogenic zone along subduction mega-thrusts. *Earth Planet. Sci. Lett.*, 215: 219–235.

Saffer, D.M., and Tobin, H.J., 2011. Hydrogeology and mechanics of subduction zone forearcs: fluid flow and pore pressure. *Annual Review of Earth and Planetary Sciences*, 39(1): 157-186.

Saffer, D.M., Underwood, M.B., and McKiernan, A.W., 2008. Evaluation of factors controlling smectite transformation and fluid production in subduction zones: Application to the Nankai Trough. *Isl. Arc,*, 17(2): 208-230.

Saffer, D., Guo, J., Underwood, M.B., Likos, W., Skarbek, R.M., Song, I., and Gildow, M., 2011. Data report: consolidation, permeability, and fabric of sediments from the Nankai continental slope, IODP Sites C0001, C0008, and C0004. *In* Kinoshita, M., Tobin, H., Ashi, J., Kimura, G., Lallemant, S., Screaton, E.J., Curewitz, D., Masago, H., Moe, K.T., and the Expedition 314/315/316 Scientists, Proc. IODP, 314/315/316: Washington, D.C. (Integrated Ocean Drilling Program Management International, Inc.).

Saito, K., Kato, K., and Sugi, S., 1997. K-Ar dating studies of Ashigawa and Tokuwa granodiorite bodies and plutonic geochronology in the South Fossa Magna, central Japan. *Isl. Arc*,, 6: 158-167.

Sato, H., Machida, S., Kanamaya, S., Taniguchi, H., and Ishii, T., 2002. Geochemical and isotopic characteristics of the Kinan Seamount Chain in the Shikoku Basin. *Geochem. J.*, 36: 519-526.

Schallreuter, R., 1984. Framboidal pyrite in deep-sea sediment. *In* Hay, W.W., Sibuet, J.-C., *et al., Init. Repts. DSDP*, 75: Wahsington D.C. (U.S. Governtment Printing Office), 875-891.

Schwartz, F.W., and Zhang, H., 2003. *Fundamentals of Ground Water*: New York, John Wiley & Sons.

Screaton, E., Kimura, G., Curewitz, D., Moore, G., Chester, F., Fabbri, O., Fergusson, C., Girault, F., Goldsby, D., Harris, R., Inagaki, F., Jiang, T., Kitamura, Y., Knuth, M., Li, C. F., Claesson Liljedahl, L., Louis, L., Milliken, K., Nicholson, U., Riedinger, N., Sakaguchi, A., Solomon, E., Strasser, M., Su, X., Tsutsumi, A., Yamaguchi, A., Ujiee, K., and Zhao, X., 2009b. Interactions between deformation and fluids in the frontal thrust region of the NanTroSEIZE transect offshore the Kii Peninsula, Japan: Results from IODP Expedition 316 Sites C0006 and C0007. *Geochem., Geophys., Geosyst.*, 10(12): 1-14.

Screaton, E., Rowe, K., Sutton, J., and Atalan, G., 2013. Data report: permeabilities of Expedition 322 and 333 sediments from offshore the Kii Peninsula, Japan. *In* Saito, S., Underwood, M.B., Kubo, Y., and the Expedition 322 Scientists, *Proc. IODP*, 322: Tokyo (Integrated Ocean Drilling Program Management International, Inc.).

Sdrolias, M., Roest, W.R., and Müller, R.D., 2004. An expression of Philippine Sea plate rotation: the Parece Vela and Shikoku basins. *Tectonophysics*, 394(1): 69-86.

Seno, T., 1977. The instantaneous rotation vector of the Philippine Sea Plate relative to the Eurasian Plate. *Tectonophysics*, (42): 209-226.

Seno, T., Stein, S., and Gripp, A.E., 1993. A model for the motion of the Philippine Sea plate consistent with NUVEL-1 and geological data. *J. Geophys. Res., [Solid Earth], (1978–2012)*, 98(B10): 17941-17948.

Simpson, G., 2010. Formation of accretionary prisms influenced by sediment subduction and supplied by sediments from adjacent continents. *Geology*, 38(2): 131-134.

Sintubin, M., 1994. Clay fabrics in relation to the burial history of shales. *Sedimentology*, 41: 1161-1169.

Spinelli, G., and Harris, R.N., 2011. Thermal effects of hydrothermal circulation and seamount subduction: temperature in the Nankai Trough Seismogenic Zone Experiment transect. *Japan Geochem., Geophys., Geosyst.*, 12(12): 1-15.

Spinelli, G.A., and Saffer, D.M., 2004. Along-strike variations in underthrust sediment dewatering on the Nicoya margin, Costa Rica related to the updip limit of seismicity. *Geophys. Res. Lett.*, 31 (L04613).

Spinelli, G.A., and Underwood, M.B., 2004. Character of sediments entering the Costa Rica subduction zone: Implications for partitioning of water along the plate interface. *Isl. Arc*,, 13: 432-451.

Steurer, J.F., and Underwood, M.B., 2003. Clay mineralogy of mudstones from the Nankai Trough reference Sites 1173 and 1177 and frontal accretionary prism Site 1174. *In* Mikada, H., Moore, G.F., Taira, A., Becker, K., Moore, J.C., and Klaus, A. (Eds.), *Proc. ODP, Sci. Results*, 190/196: College Station, TX (Ocean Drilling Program), 1-37.

Strasser, M., Moore, G.F., Kimura, G., Kitamura, Y., Kopf, A.J., Lallemant, S., Park, J.-O., Screaton, E.J., Su, X., Underwood, M.B., and Zhao, X., 2009. Origin and evolution of a splay fault in the Nankai accretionary wedge. *Nat. Geosci.*, 2(9):648–652.

Sugihara, T., Kinoshita, M., Araki, E., Kimura, T., Kyo, M., Namba, Ya. Kido, Y., Sanada, Y., and Thu, M.K., 2014. Re-evaluation of temperature at the updip limit of locked portion of Nankai megasplay inferred from IODP Site C0002 temperature observatory. *Earth, Planets Space*, 66(107): 1-14.

Sugioka, H., Okamoto, T., Nakamura, T., Ishihara, Y., Ito, A., Obana, K., Kinoshita, M., Nakahigashi, K., Shinohara, M., and Fukao, Y., 2012. Tsunamigenic potential of the shallow subduction plate boundary inferred from slow seismic slip. *Nat. Geosci.*, 5(6):414–418.

Taira, A., and Ashi, J., 1993. Sedimentary facies evolution of the Nankai forearc and its implications for the growth of the Shimanto accretionary prism. *In* Hill, I.A., Taira, A., Firth, J.V., *et al., Proc. ODP, Sci. Results*, 131: College Station, TX (Ocean Drilling Program), 331-341.

Taira, A., Katto, J., Tashiro, M., Okamura, M., and Kodama, K., 1988. The Shimanto Belt in Shikoku, Japan: Evolution of Cretaceous to Miocene accretionary prism. *Mod. Geol.*, 12: 5–46.

Taira, A., and Tashihiro, M. (Eds.), 1987. *Late Paleozoic and Mesozoic accretion tectonics of Japan and eastern Asia, in Historical Paleogeography and Plate Tectonic Evolution of Japan and Eastern Asia*: Terra Scientific Publishing Company, Tokyo, 1-47.

Tamaki, K., 1985. Two modes of back-arc spreading. *Geology*, 13(7): 475-478.

Thiry, M., 2000. Palaeoclimatic interpretation of clay minerals in marine deposits: an outlook from the continental origin. *Earth-Science Reviews*, (49): 201-221.

Tobin, H.J., and Kinoshita, M., 2006. NanTroSEIZE: The IODP Nankai Trough Seismogenic Zone Experiment. *Sci. Dril.*, (2): 23-27.

Tobin, H., Kinoshita, M., Ashi, J., Lallemant, S., Kimura, G., Screaton, E.J., Moe, K.T., Masago, H., Curewitz, D., and the Expedition 314/315/316 Scientists, 2009. NanTroSEIZE Stage 1 expeditions: introduction and synthesis of key results. *In* Kinoshita, M., Tobin, H., Ashi, J.,

Kimura, G., Lallemant, S., Screaton, E.J., Curewitz, D., Masago, H., Moe, K.T., and the Expedition 314/315/316 Scientists, *Proc. IODP*, 314/315/316: Washington, D.C. (Integrated Ocean Drilling Program Management International, Inc.).

Underwood, M.B., 2002. Strike-parallel variations in clay minerals and fault vergence in the Cascadia subduction zone. *Geology*, 30 (2): 155–158.

Underwood, M.B., 2007. Clay mineral composition and diagenesis: Effects on the location and behavior of faults in the frontal portions of subduction zones. *Sci. Dril.*, SpecialIssue: 61-63.

Underwood, M.B., Basu, N., Steurer, J., and Udas, S., 2003. Data report: Normalization factors for semiquantitative X-ray diffraction analysis, with application to DSDP Site 297, Shikoku basin. *In* Mikada, H., Moore, G.F., Taira, A., Becker, K., Moore, J.C., and Klaus, A. (Eds.), *Proc. ODP, Sci. Results*, 190/196: College Station, TX (Ocean Drilling Program).

Underwood, M.B., and Fergusson, C.L., 2005. Late Cenozoic evolution of the Nankai trench-slope system: evidence from sand petrography and clay mineralogy. *In* Hodgson, D.M., and Flint, S. S. (Eds), *Submarine Slope Systems: Processes and Products,* 244*:* Geological Society, London, Special Publications, 113–129.

Underwood, M.B., and Guo, J., 2013. Data report: clay mineral assemblages in the Shikoku Basin, NanTroSEIZE subduction inputs, IODP Sites C0011 and C0012. *In* Saito, S., Underwood, M.B., Kubo, Y., and Expedition 322 Scientists, *Proc. IODP,* 322: Tokyo (Integrated Ocean Drilling Program Management International, Inc.).

Underwood, M.B. and Moore., G.F., 2012. Evolution of sedimentary environments in the subduction zone of southwest Japan: recent results from the NanTroSEIZE Kumano transect. *In* Busby, C. and Azor, A. (Eds.), *Tectonics of Sedimentory Aasins: Recent Advances*: John Wiley & Sons, Ltd, Chichester, UK, 310-326.

Underwood, M.B., Pickering, K., Gieskes, J.M., Kastner, M., and Orr, R., 1993. Sediment geochemistry, clay mineralogy, and diagenesis: A synthesis of data from Leg 131, Nankai Trough. *In* Hill, I.A., Taira, A., Firth, J.V., *et al., Proc. ODP, Sci. Results*, 131: College Station, TX (Ocean Drilling Program), 343-363.

Underwood, M.B., and Pickering, K.T., 1996. Clay-mineral provenance, sediment dispersal patterns, and mudrock diagenesis in the Nankai accretionary prism, southwest Japan. *Clays Clay Miner.*, 44(3): 339-356.

Underwood, M.B., Saito, S., Kubo, Y., and the Expedition 322 Scientists, 2010. Expedition 322 summary. *In* Saito, S., Underwood, M.B., Kubo, Y., and the Expedition 322 Scientists, *Proc. IODP*, 322: Tokyo (Integrated Ocean Drilling Program Management International, Inc.).

Underwood, M.B. and Steurer, J.F., 2003. Composition and sources of clay from the trench slope and shallow accretionary prism of Nankai Trough. *In* Mikada, H., Moore, G.F., Taira, A., Becker, K., Moore, J.C., and Klaus, A. (Eds.), *Proc. ODP, Sci. Results*, 190/196: College Station, TX (Ocean Drilling Program), 1-28.

Uyeda, S., and Hascgawa, A., 1995. Dynamics of lithosphere convergence. *International Lithosphere Program Workshop Report*: September 17-20, 1995, Miyagi, Japan.

Verdel, C., Niemi, N., and van der Pluijm, B.A., 2011. Variations in the illite to muscovite transition related to metamorphic conditions and detrital muscovite content: Insight from the Paleozoic passive margin of the southwestern United States. *J. Geol.*, 119(4): 419-437.

Vrolijk, P., 1990. On the mechanical role of smectite in subduction zones. *Geology*, 18: 703-707.

Wang, K., Hyndman, R.D., and Yamano, M., 1995. Thermal regime of the southwest Japan subduction zone: Effects of age history of the subducting plate. *Tectonophysics*, 248: 53-69.

Worden, R.H., and Burley, S.D., 2003. Sandstone diagenesis: the evolution of sand to stone. *In* Burley, S.D., Worden, R.H. (Eds.), *Clastic Diagenesis: Recent and Ancient*, 4: International Association of Sedimentologists, Blackwells, Oxford, 3–44.

Yamano, M., Kinoshita, M., Goto, S., and Matsubayashi, O., 2003. Extremely high heat flow anomaly in the middle part of the Nankai Trough. *Physics and Chemistry of the Earth*, 28: 487-497.

Yang, Y., and Aplin, A.C., 2007. Permeability and petrophysical properties of 30 natural mudstones. *J. Geophys. Res., [Solid Earth],* 112(B03): 1-14.

Yoshioka, S., and Murakami, K., 2007. Temperature distribution of the upper surface of the subducted Philippine Sea Plate along the Nankai Trough, southwest Japan, from a three-dimensional subduction model: relation to large interplate and low-frequency earthquakes. *Geophys. J. Int.*, 171(1): 302-315.

Yue, L., Likos, W.J., Guo, J., and Underwood, M.B., 2012. Data report: permeability of mud(stone) samples from Site C0001, IODP Expedition 315, Nankai Trough: NanTroSEIZE Stage 1. *In* Kinoshita, M., Tobin, H., Ashi, J., Kimura, G., Lallemant, S., Screaton, E.J., Curewitz, D., Masago, H., Moe, K.T., and the Expedition 314/315/316 Scientists, *Proc. IODP*, 314/315/316: Washington, D.C. (Integrated Ocean Drilling Program Management International, Inc.).

APPENDIX

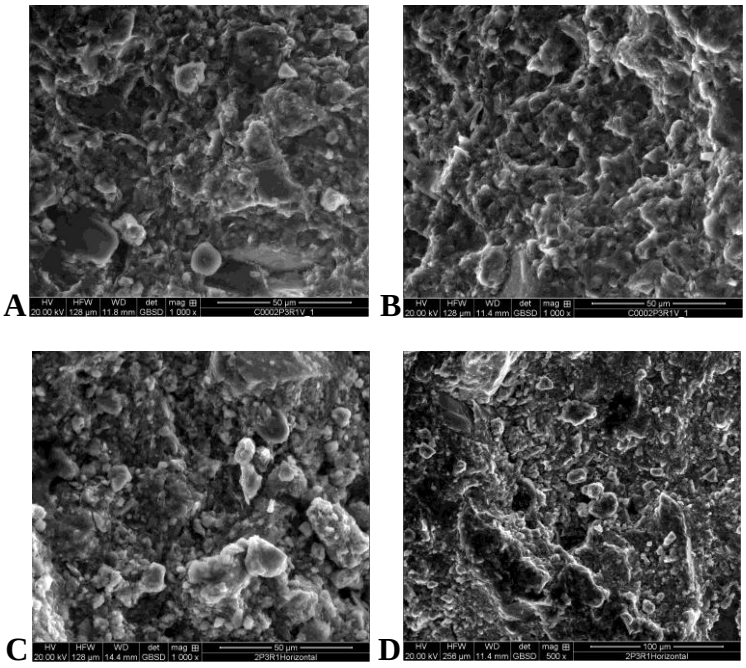

Figure A1. SEM images of grain sizes in specimens cut from 348-C0002P-3R-1, 51 cm. A and B: images of specimen cut parallel to the core axis. C and D: images of specimen cut perpendicular to the core axis.

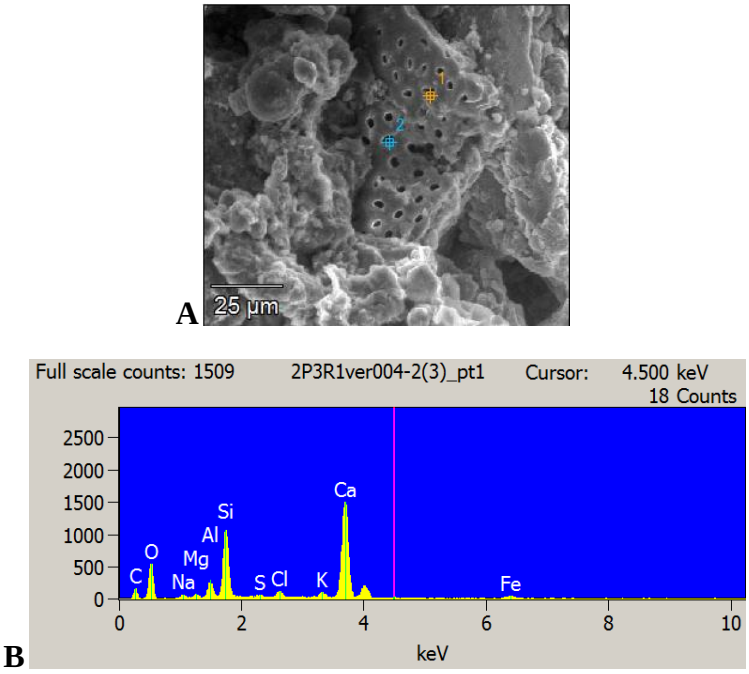

Figure A2. Calcium compound (one type of fossil) in specimen cut from 348-C0002P-3R-1, 51 cm. A: Image used for EDS analysis. C: EDS spectrum results on point 1 from image B. Points 2 shows the similar result as point 1 so its EDS spectrum result is not shown here.

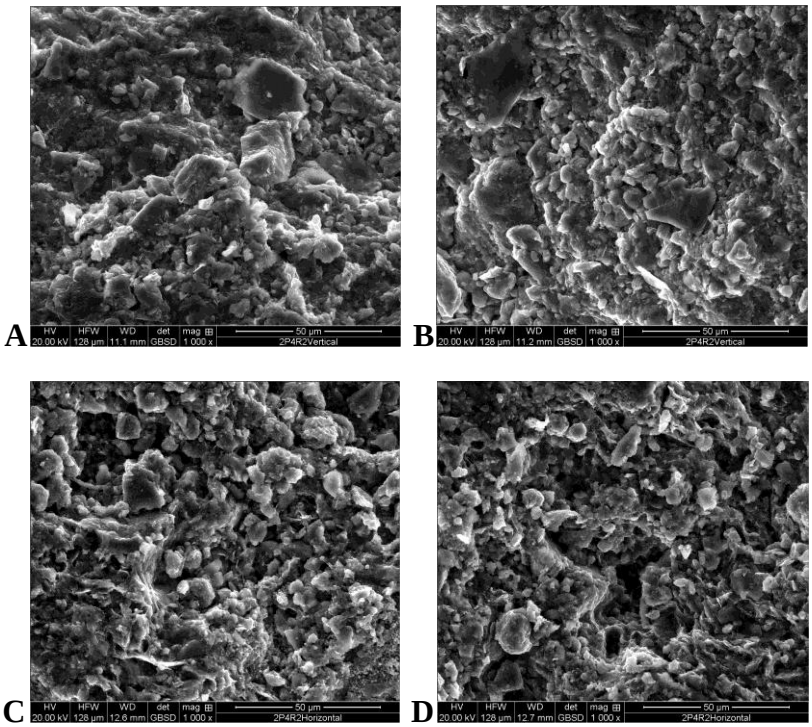

Figure A3. SEM images of grain sizes in specimens cut from 348-C0002P-4R-2, 98 cm. A and B: images of specimen cut parallel to the core axis. C and D: images of specimen cut perpendicular to the core axis.

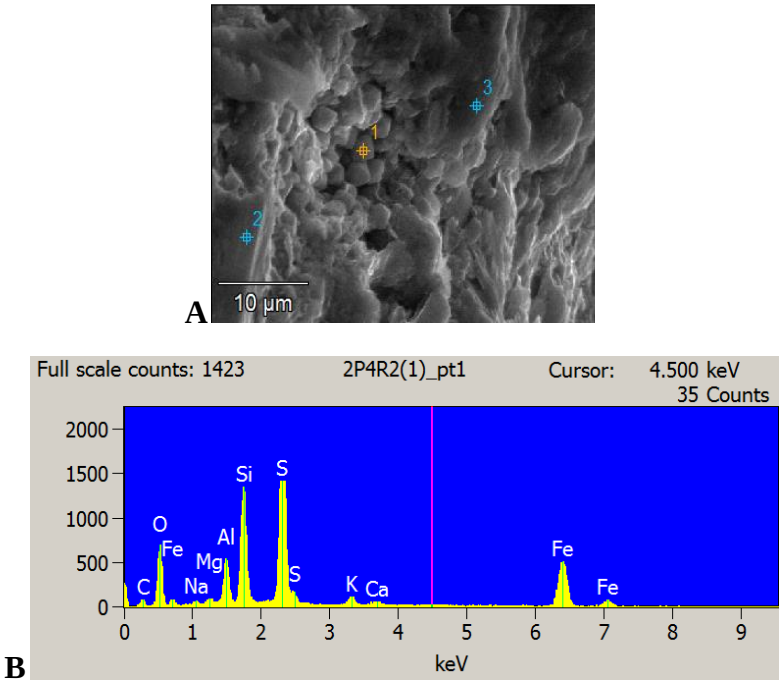

Figure A4. Possible pyrite inside the specimen cut from C0002P-4R-2, 98 cm. A: Image of the possible pyrite used for EDS analysis. B: EDS spectrum results on point 1 from image B. Points 2 and 3 are used for comparison which are typical silicate minerals so no EDS spectrum is shown here.

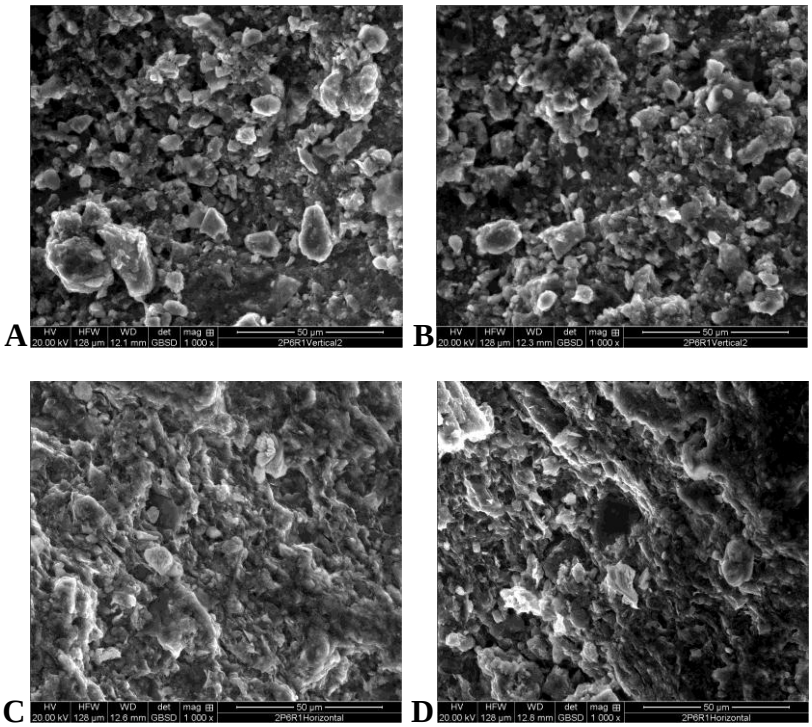

Figure A5. SEM images of grain sizes in specimens cut from 348-C0002P-6R-1, 64 cm. A and B: images of specimen cut parallel to the core axis. C and D: images of specimen cut perpendicular to the core axis.

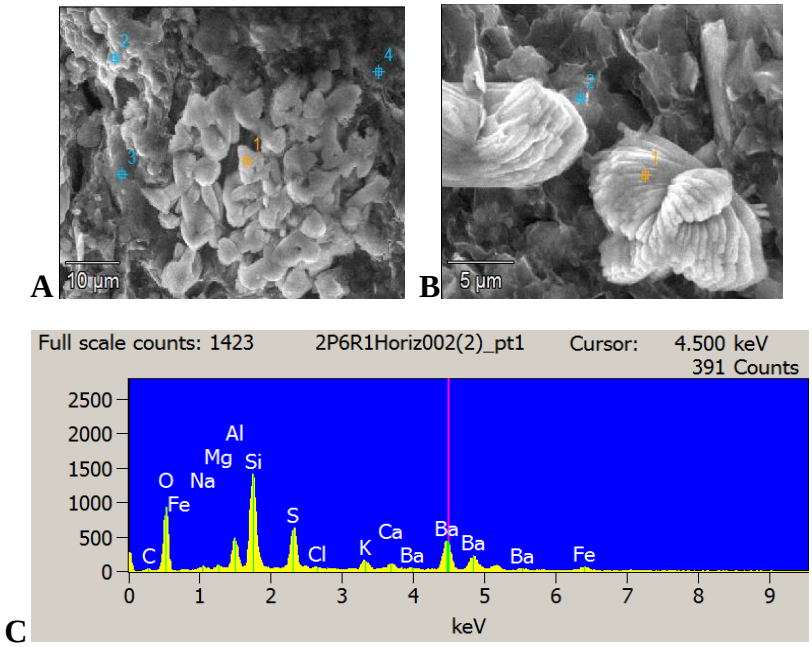

Figure A6. Barite inside the specimen cut from C0002P-6R-1, 64 cm. A and B: Images of barite used for EDS analysis. C: EDS spectrum results on point 1 from image B. Point 1 from image A is similar as point 1 from image B so only one spectrum is shown here. The rest of the points from both images are used for comparison which are typical silicate minerals so no EDS spectrum is shown here.

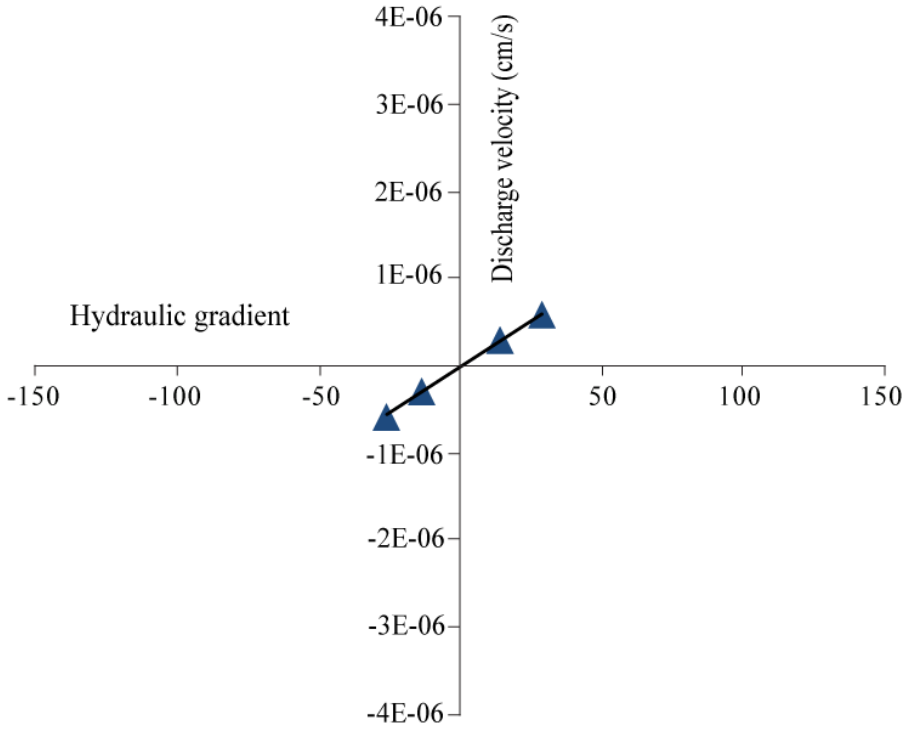

Figure A7. Hydraulic gradient vs. discharge velocity (348-C0002P-3R-1, 51 cm @0.28 MPa).

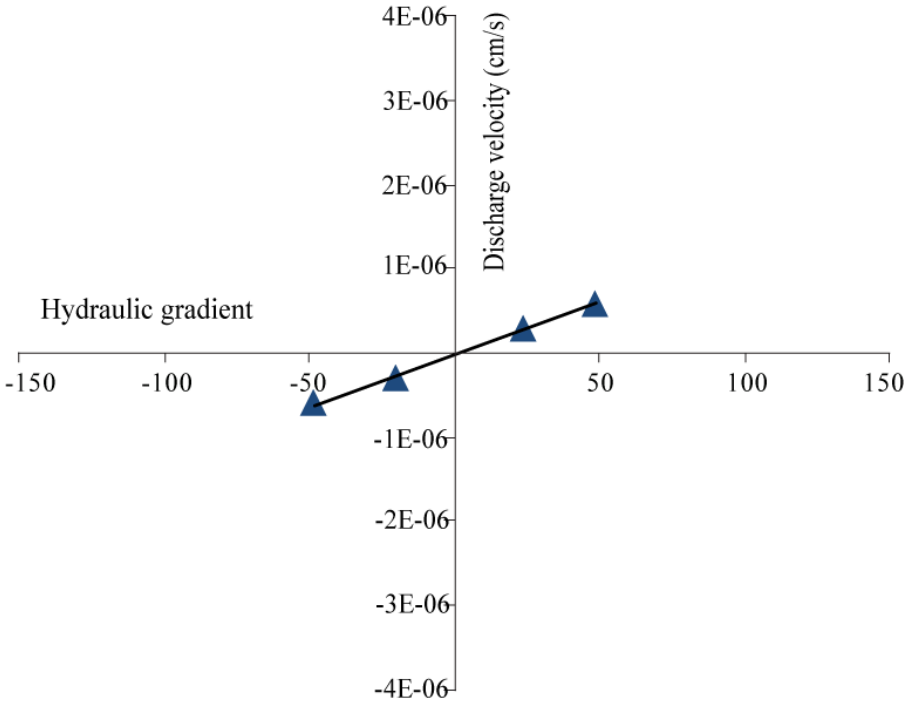

Figure A8. Hydraulic gradient vs. discharge velocity (348-C0002P-3R-1, 51 cm @0.55 MPa).

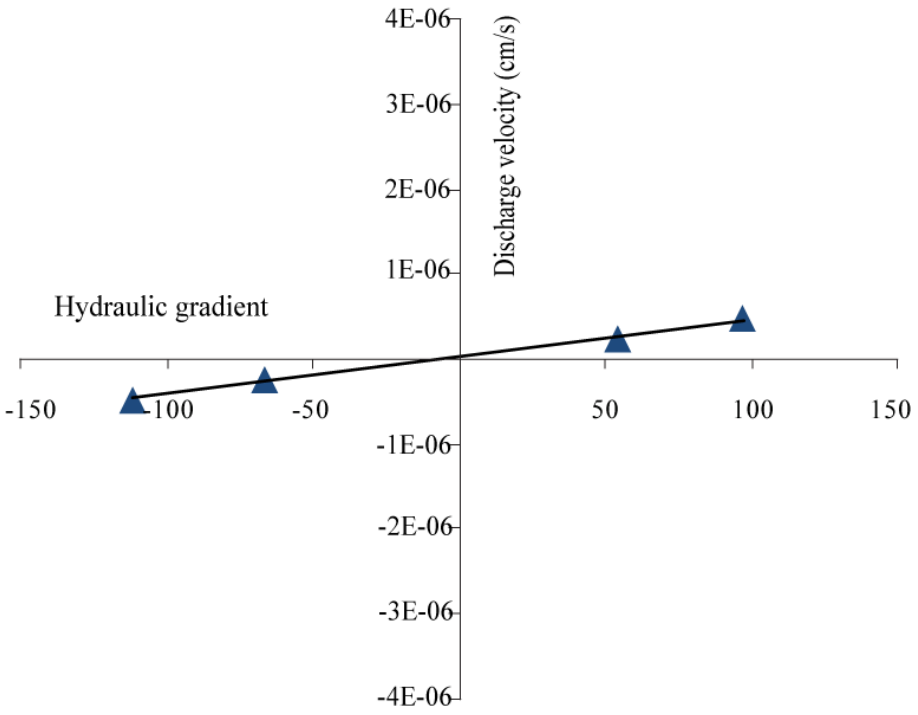

Figure A9. Hydraulic gradient vs. discharge velocity (348-C0002P-4R-2, 98 cm @0.28 MPa).

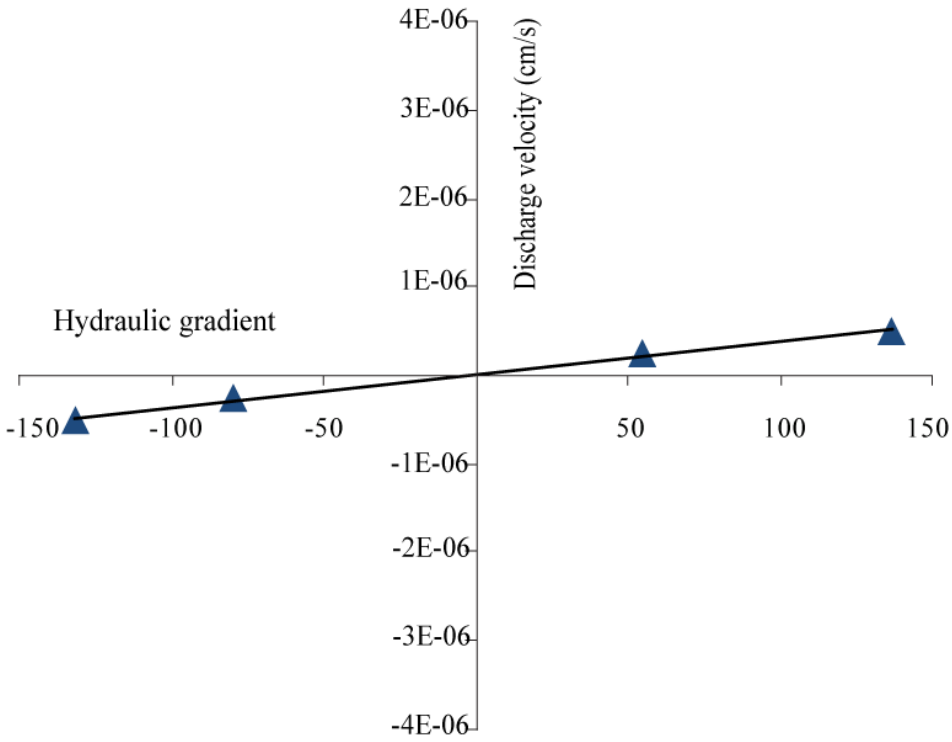

Figure A10. Hydraulic gradient vs. discharge velocity (348-C0002P-4R-2, 98 cm @0.55 MPa).

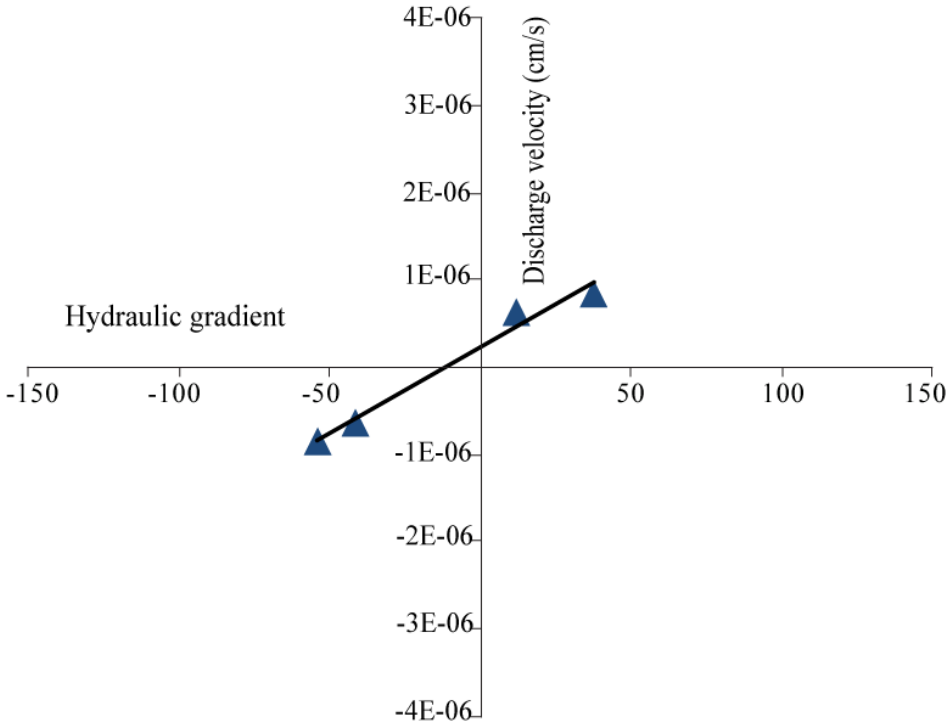

Figure A11. Hydraulic gradient vs. discharge velocity (348-C0002P-6R-1, 64 cm @0.28 MPa).

Table A1. Results of individual constant-flow permeability tests, Hole C0002P. Note that some tests failed because of a faulty pressure transducer.

Hole, core, section, interval (cm)	Effective stress (MPa)	Test run	Volumetric flow rate (cm^3/min)	Discharge velocity (cm/s)	Head difference (cm)	Hydraulic gradient	Hydraulic conductivity (cm/s)	Intrinsic permeability (m^2)
348-C0002P-								
3R-01, 51 vertical	0.28	1	0.0002	2.94E-07	109	13.97	2.10E-08	2.09E-17
		2	-0.0002	-2.94E-07	-107	-13.72	2.14E-08	2.13E-17
		3	0.0004	5.88E-07	225	28.85	2.04E-08	2.02E-17
		4	-0.0004	-5.88E-07	-204	-26.15	2.25E-08	2.23E-17
						Average	2.13E-08	2.12E-17
3R-01, 51 vertical	0.55	1	0.0002	2.94E-07	184	23.59	1.25E-08	1.24E-17
		2	-0.0002	-2.94E-07	-159	-20.38	1.44E-08	1.43E-17
		3	0.0004	5.88E-07	377	48.33	1.22E-08	1.21E-17
		4	-0.0004	-5.88E-07	-380	-48.72	1.21E-08	1.20E-17
						Average	1.28E-08	1.27E-17
4R-02, 98 vertical	0.28	1	0.0002	2.41E-07	200	54.05	4.45E-09	4.42E-18
		2	-0.0002	-2.41E-07	-247	-66.76	3.60E-09	3.58E-18
		3	0.0004	4.81E-07	358	96.76	4.97E-09	4.94E-18
		4	-0.0004	-4.81E-07	-414	-111.89	4.30E-09	4.27E-18
						Average	4.33E-09	4.30E-18
4R-02, 98 vertical	0.55	1	0.0002	2.53E-07	196	54.44	4.64E-09	4.60E-18
		2	-0.0002	-2.53E-07	-288	-80.00	3.16E-09	3.13E-18
		3	0.0004	5.05E-07	491	136.39	3.70E-09	3.67E-18
		4	-0.0004	-5.05E-07	-475	-131.94	3.83E-09	3.80E-18
						Average	3.83E-09	3.80E-18
6R-01, 64 vertical	0.28	1	0.0006	6.34E-07	52	11.82	5.38E-08	5.34E-17
		2	-0.0006	-6.34E-07	-183	-41.59	1.53E-08	1.52E-17
		3	0.0008	8.45E-07	165	37.50	2.26E-08	2.24E-17
		4	-0.0008	-8.45E-07	-238	-54.09	1.57E-08	1.55E-17
						Average	2.68E-08	2.66E-17